Complex optical metasurfaces for multi-functional holography

Dissertation

zur Erlangung des akademischen Titels

doctor rerum naturalium

(Dr. rer. nat.)

vorgelegt der Fakultät für Naturwissenschaften der Universität Paderborn

von M. Sc. Daniel Frese

geboren am 12. September 1991 in Marburg

Gutachter:

Prof. Dr. Thomas Zentgraf

Prof. Dr. Donat As

Eingereicht am: 27.01.2022

Erklärung der Selbstständigkeit

Hiermit versichere ich die vorliegende Arbeit mit dem Titel „Complex optical metasurfaces for multi-functional holography“ selbständig verfasst und keine anderen als die angegebenen Quellen und Hilfsmittel verwendet, sowie Zitate kenntlich gemacht zu haben. Diese Arbeit hat in gleicher oder ähnlicher Form noch keiner Prüfungsbehörde vorgelegen.

Paderborn, den 27.01.2022

Abstract

In the present work, different metasurface holograms are investigated as functional holographic devices. Different geometries, arrangements and materials of nanoantennas, which are the building blocks of metasurfaces, are investigated to encode the holograms.

Using a plasmonic two-layer structure, consisting of one layer of antennas for the phase encoding and one layer of antennas which is utilized as a polarizer, a directional hologram is generated and compared to a direction-independent hologram. It is shown that a potential coupling in the bilayer structure has an impact on the conversion efficiency of the hologram.

Furthermore, it is shown how wavelength and polarization dependent holograms can be fabricated based on the principle of a photon sieve. By using specially designed silicon nanoantennas, which are utilized as spectral filters, two amplitude holograms combined with a phase hologram can be encoded into one metasurface. The different holograms can be reconstructed by changing the polarization and wavelength of the incident light.

Lastly, using rotationally symmetric plasmonic nanoantennas, a nonlinear hologram based on the Pancharatnam-Berry phase is generated. When the metasurface is excited with near-infrared laser light with appropriate power, wavelength, and polarization, a two-color image in the visible spectral range can be generated based on second and third harmonic generation processes.

Kurzfassung

In der vorliegenden Arbeit werden Metaoberflächenhologramme als funktionale holografische Informationsträger untersucht. Dabei werden verschiedene Geometrien, Anordnungen und Materialien für Nanoantennen verwendet, um Hologramme zu kodieren.

Durch die Ausnutzung einer plasmonischen Zweilagenstruktur, wobei eine Lage aus Antennen für eine Phasenkodierung und eine Lage aus Antennen als Polarisator designt wird, wird ein richtungsabhängiges Hologramm erzeugt und mit einem richtungsunabhängigen Hologramm verglichen. Es wird gezeigt, dass eine Kopplung der Zweischichtstruktur Auswirkungen auf die Konversionseffizienz des Hologramms hat.

Des Weiteren wird untersucht, wie wellenlängen- und polarisationsabhängige Hologramme basierend auf dem Prinzip eines Photonensiebs hergestellt werden können. Durch die Verwendung speziell designter Siliziumantennen, welche als spektrale Filter eingesetzt werden, können zwei Amplitudenhologramme mit einem Phasenhologramm in eine Metaoberfläche kodiert werden. Die verschiedenen Hologramme können unter Änderung der Polarisation und Wellenlänge des einfallenden Lichts rekonstruiert werden.

Zuletzt werden rotationssymmetrischen plasmonischen Nanoantennen ausgenutzt um ein nichtlineares Hologramm basierend auf der Pancharatnam-Berry Phase zu generieren. Wenn die Metaoberfläche mit nahinfrarotem Laserlicht mit entsprechender Leistung, Wellenlänge und Polarisation angeregt wird, kann ein zweifarbiges Bild im sichtbaren Spektralbereich erzeugt werden.

Contents

1 Introduction

1.1 From the first hologram to modern holographic applications

The concept of holography was first invented by Dennis Gabor in the year 1948, who got the Nobel prize ‘for the invention and development of the holographic method’[1]. The word hologram comes from the greek words *holos* (whole) and *gramma* (message). In holography – which is different from normal photography which only stores amplitudes (intensities) – the full-wave information scattered by an object is stored. Thus, the reconstructed hologram contains three-dimensional spatial information. The basic principle of holography is related to diffraction effects, which require coherent light waves with constant phase relations. Light, which is capable to interfere is designated as coherent. In 1948, coherent light sources like lasers were not available, so Gabor used a mercury lamp combined with an optical filter and a pin-hole to create a sufficient coherence length for the first experiments [1].

The next milestones in the history of holography were the invention of the first laser by Maiman in 1960 which provided coherence lengths in the meter range and higher light intensities [2], the description of holography by communication theory by Leith and Upatnieks in 1962 [3], and the invention of computer-generated holograms by Brown and Lohmann in 1966 [4]. By using numerical computation to synthesize the diffraction pattern of a hologram for a predefined image, the elaborate recording process of holograms can be avoided.

After the invention of the holographic method, holographic applications spread out in a wide range. Art holography was the most accessible and perceived for the public [5], but useful applications for industrial usage were quite different. For example, holographic metrology became a fast and precise method to measure three-dimensional surfaces within time scales of a few seconds and accuracy in the micrometer range [6, 7]. Holographic gratings, mirrors, and lenses, which belong to the category of holographic optical elements (HOE), are often used to push developments towards holographic display applications [8, 9]. HOEs are fabricated based on the holographic recording process. Photopolymers which form the basis of the HOEs, are exposed

[1] Dennis Gabor – Facts, NobelPrize.org, Nobel Prize Outreach AB 2021, Wed. 10 Nov 2021, <https://www.nobelprize.org/prizes/physics/1971/gabor/facts/>

to light scattered by an object and a reference beam [10]. The occurring standing wave pattern within the photopolymer film creates a refractive index change and enables a very flexible design of refractive and diffractive HOEs. In contrast to bulky lenses and other optical components, HOEs profit from their low thickness of several 100 µm and are generally elastic, so that they can be applied to curved surfaces like windshields. This is an advantage for head-up displays, where HOEs are used to project holograms within the user's field of view without covering the environment [9]. The hologram which is projected onto a user's field of view is generally a phase-only hologram provided by a projector. Holographic projectors are mostly spatial light modulators (SLM) that imprint the phase information on an incident plane wave, based on liquid crystals arranged in pixels, which can be individually polarized by applying an electric field and changing the refractive indices of the pixels [11-13]. Combining SLMs with HOEs, flexible head-up displays can be realized which already find applications in aircrafts and cars[2].

Although the SLMs as phase or amplitude modulators are very advanced in development, they come with limitations. Spatial light modulators, which are the hearth for holographic applications, can only modulate the phase or the amplitude of an incoming wave. In addition, the relatively large pixel size of a few micrometers is accompanied by a relatively small field of view and generates higher-order diffraction, resulting in losses [14].

Besides SLMs, metasurfaces are attractive candidates for holographic applications. Metasurfaces consist of artificially structured nanoantennas that can be designed from different materials with a high degree of freedom to manipulate light in amplitude, phase, and polarization. The high flexibility in light manipulation arises from the individually shaped nanoantennas, which can be designed to accommodate different wavelengths, interact with specific polarization states, etc [15]. The antennas allow spatial control of wavefronts along the surface, which is very useful for a wide range of applications. Metasurfaces can be designed to either mimic the functionalities of bulky optical elements, such as lenses or waveplates[16, 17], or introduce complex phase manipulations for holographic applications [18, 19]. Compared to SLMs, the pixel size of metasurface holograms in the visible regime is in the range of several hundred nanometers instead of micrometers. Thereby, higher-order diffraction can be avoided and the field of view can be enhanced. Furthermore, metasurfaces can be designed to control the phase and amplitude of light simultaneously [20]. However, one disadvantage of metasurfaces is that they

[2] Carl Zeiss AG – Multifunktionales Smartes Glas, Sun. 16 Nov 2022, <https://www.zeiss.de/oem-solutions/produkte-loesungen/multifunktionales-smartes-glas.html>

are generally static devices. Once the antennas are fabricated, the arrangement cannot be changed anymore. To overcome this disadvantage and make these static devices multifunctional, multiplexing techniques can be applied so that metasurfaces become optically switchable [21, 22].

Commonly used multiplexing methods are wavelength and polarization multiplexing. Wavelength multiplexing is attractive for display applications because of the colorful reconstructed images which can be achieved. Therefore, the pixels of a metasurface hologram can consist of multiple antennas, for example, antennas that interact either with red (R), green (G) light, or blue (B) light. Thus, different images can be encoded in the RGB components (so to say RGB antennas) of the metasurface [23, 24]. One disadvantage is the lower space-bandwidth product compared to a metasurface which utilizes a pixel consisting of one antenna for several tasks. This disadvantage can be overcome by polarization multiplexing. It has been shown that e. g. rectangular dielectric antennas can be utilized to encode three different phase-holograms in three different polarization channels. In this way, the images can be reconstructed depending on the chosen input and output polarization states, as well as the wavelength which is used for the reconstruction [25, 26]. There are many other multiplexing methods, for example, based on nonlinear generations [27], utilizing addressable dynamic pixels [28], and others[21]. The goal of many metasurface researchers is to expand the functionality of metasurfaces so that they become attractive for commercial applications. However, the research area still leaves room to generate and combine further functionalities or to use alternative manufacturing processes.

In this thesis, I present three approaches to complex optical metasurfaces to expand the functionalities of metasurface holograms. Therefore, a layered holographic metasurface is designed to modulate both, the amplitude and phase of the transmitted light, by simultaneously introducing asymmetric transmission of the metasurface. The phase profile is calculated using the Gerchberg-Saxton algorithm [29], while the amplitude is modulated by the antenna design which is drafted based on FDTD simulations. The hologram can be reconstructed in a particular propagation direction and polarization state, while it disappears in the reverse propagation direction of the light. Such directionality is generally not achievable in planar metasurfaces which are symmetric perpendicular to the surface. Furthermore, a metasurface color-hologram is realized by using a photon sieve approach combined with spectral filters. The photon sieve consists of a gold film with particularly arranged and designed nanohole patterns filled with spectral filters. The photon sieve stores two amplitude holograms at different wavelengths and additionally stores a phase-only hologram, which is different from the generally broadband operation of photons sieves. The hologram is wavelength- and polarization-multiplexed. In the last project, I introduce a nonlinear bi-colored hologram based on the Pancharatnam-Berry phase approach. When the nonlinear hologram is resonantly excited in the near-infrared, the reconstructed image appears in the visible spectrum of light. The reconstructed holograms are generated based on second and third harmonic generation processes of rotation symmetric plasmonic nanoantennas. This is an example of wavelength multiplexing based on two nonlinear processes.

1.2 Structure of this thesis

This thesis is organized as follows: Before diving directly into the holographic metasurface concepts, an overview of holography and metasurface holography is given in section 2, followed by the description of abrupt phase changes at optical interfaces which can be introduced by metasurfaces. Thereafter the Gerchberg-Saxton algorithm is explained, which is used to calculate desired phase masks for the metasurface holograms which are encoded in plasmonic or dielectric nanoantennas. Lastly, I show the fabrication techniques which are used to fabricate metasurface holograms presented in this thesis and a Fourier imaging setup for the hologram reconstruction.

The first study is presented in section 3. Most of the existing metasurfaces are made of planar, two-dimensional structures, where the thickness of the metasurface is smaller than the wavelength λ of the light. Since the structures are mostly symmetric in the propagation direction of the light, the optical response of the metasurface is the same in the forward and the backward direction. To create a directional holographic scheme, a stacked metasurface concept is fabricated with a thickness of approximately $\frac{3}{25}\lambda$. By breaking the symmetry of the metasurface in the propagation direction of the light by stacking two different layers of nanoantennas, the encoded hologram can only be reconstructed in a particular direction and polarization state. The directionality of the hologram is interesting for anti-counterfeiting allocations and information processing [30].

To expand the functionality of photon sieve holograms which are generally broadband and polarization-independent, a concept to replace the nanoholes with square and rectangular nanoapertures, filled with band-pass filters is shown in section 4. Thus, not only wavelength but also polarization multiplexing is realized. The hologram stores two different amplitude holograms at two different wavelengths and an additional phase-only hologram. Attractive applications are holographic displays, where different holograms can be reconstructed by switching the wavelength or polarization state of the light [31].

In section 5, a concept of a plasmonic bi-colored nonlinear hologram is shown. When the metasurface hologram is illuminated with near-infrared laser light, the transmitted beam does not carry any image information in the linear regime. However, the created second and third-harmonic signals of two different types of nanoantennas form a nonlinear image in the visible regime. It is demonstrated that the intensities of the nonlinear signals can be tuned by the properties of the incident beam [32].

In section 6, the thesis is summarized and a short outlook is given.

2 An introduction to metasurface holography

This chapter builds a roadmap from classical holography towards holographic metasurface applications. Classical holography is also known as optical holography, where the hologram recording is done based on interference in experiments. Metasurface holography is a part of digital holography, where the object or image is computed and coded into a metasurface hologram. First, I briefly revisit the classical recording and reconstruction of holograms. Second, I lead over to metasurface holography and then introduce the generalized Snell's law, the Gerchberg Saxton algorithm, followed by different plasmonic and dielectric nanoantenna types as building blocks for metasurface holograms. The design procedure of nanoantennas is explained by an example of a plasmonic nanoantenna. After that, I show how the plasmonic and dielectric metasurfaces presented in the thesis were fabricated. Lastly, a typically used Fourier plane imaging setup is illustrated, which is used for the image reconstruction of the Fourier holograms.

2.1 Fundamentals of classical holography

A hologram contains three-dimensional information of a light wave scattered by an object. The concept of holography is based on the interference and the diffraction of light. In short: A hologram is the interference pattern of scattered light from an object and a reference beam. The interference pattern can be stored on a light-sensitive film. In order to create a hologram, certain conditions must be fulfilled to enable interference: The light source used for holographic applications must be coherent. An ideally coherent light wave has an exactly defined amplitude and phase. Conventional light sources fulfill this condition only in a limited space-time domain. To classify the coherence of light sources, one can distinguish between temporal and spatial coherence [5].

Temporal coherence describes the correlation between two light signals at a fixed point in space but for different points in time. If the temporal separation of the two light signals exceeds a critical time (the so-called coherence time τ_c), they are not able to interfere, and the phase difference varies statistically. The coherence length $l_c = \tau_c \cdot c$ is the path that the light travels within the coherence time τ_c. Temporal coherence describes how monochromatic a light source is. For light sources with Gaussian emission spectra, the coherence length can be estimated as [33]

$$l_c = \tau_c \cdot c = \sqrt{\frac{2 \cdot \ln(2)}{\pi \cdot n}} \cdot \frac{\lambda^2}{\Delta\lambda} \tag{2.1}$$

where c is the speed of light, n the refractive index of the medium, λ the center wavelength of the Gaussian spectrum, and $\Delta\lambda$ the full width of half maximum of the spectrum. Light sources with small $\Delta\lambda$ such as lasers are temporally coherent, while white light lamps with large $\Delta\lambda$ are generally temporally incoherent. The influence of temporally coherent light on the interference is illustrated in Figure 2.1a using a double-slit experiment. If a point source emits two waves W_1 and W_2 with different wavelengths, both waves create an interference pattern behind the slits on an observation plate. The peak-to-peak distance increases for an increasing wavelength difference. As a consequence, for a nonzero difference between the wavelengths of waves W_1 and W_2, the higher diffraction orders will decrease rapidly. [34]

Spatial coherence describes the correlation between the amplitude of the light at two different positions at a given time. One can also measure the spatial coherence using a double-slit experiment as illustrated in Figure 2.1b. When the light waves of two displaced point-sources S_1 and S_2 with same wavelength (monochromatic light source) passes the double slits, each wave shows a sine-like interference pattern on the observation plate. For perfectly coherent light, which resembles a displacement of S_1 and S_2 equal to zero, the contrast of the interference pattern is maximum and destructive interference reaches zero. In the case of spatial coherence, the interference patterns of S_1 and S_2 are displaced on the observation plate. As a result, the

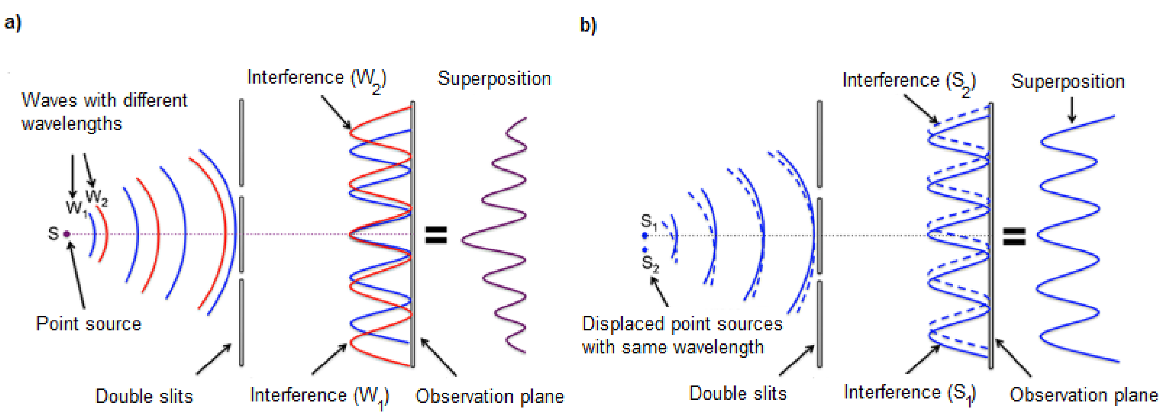

Figure 2.1 Illustration of the interference effect of a) a point source emitting two different wavelength and b) a light source consisting of two displaced point sources both emitting the same wavelength) [34].

contrast of the superposition decreases for monochrome sources which deviate from an ideal point source. For incoherent light, the interference pattern vanishes completely [4, 34].

The image quality of the reconstructed hologram depends on the quality of the hologram itself, as well as the coherence quality of the used laser light for the reconstruction. The image sharpness can be directly linked to spatial coherence. For an increasing spectral width of the source, a reconstructed hologram would be blurred. A certain degree of temporal coherence is needed so that the phase front over the beam cross-section is homogeneous [34].

A classical recording of a hologram is shown in Figure 2.2a. Monochromatic laser light is used to illuminate an object. The light scattered by the object reaches a photosensitive plate. A reference beam of the laser light is superimposed onto the photosensitive plate with the scattered light. The photosensitive plate is exposed according to the interference pattern and is called the hologram. After the development of the plate, the hologram carries the full phase and amplitude information of the scattered light of the object. [5]

The reconstruction of the hologram is illustrated in Figure 2.2b. When laser light with the same wavelength and direction illuminates the hologram, the laser light diffracts when hitting the hologram. For an observer who looks at the hologram in direction of the dashed line, a virtual image of the recorded object appears behind the hologram. [5]

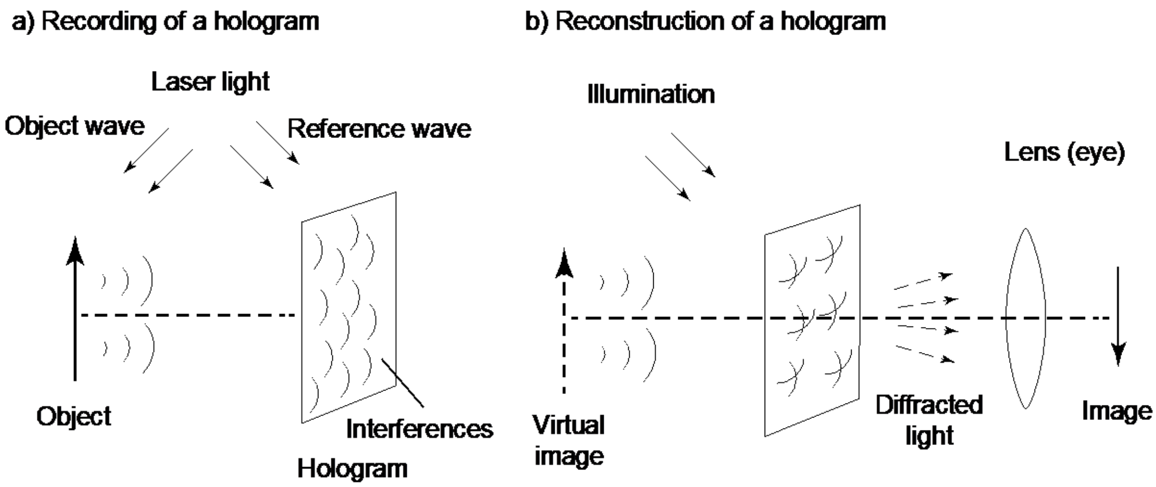

Figure 2.2 Recording and reconstruction of classical holograms. a) General recording of a hologram: Scattered laser light of an object is superimposed with a reference beam on a photosensitive film. b) Reconstruction of the hologram: If the hologram is illuminated with the same light source in the same direction than during the recording, the hologram diffracts the light in a way that an observer can see a virtual image of the recorded object [5].

2.2 Overview of metasurface holograms

Different from classic holograms, in metasurface holography the hologram is not stored in a medium but rather is built of two-dimensional arrangements of artificially structured nanoantennas. Those antennas can capture the light and re-emit it with the desired phase, amplitude, polarization, or even frequency [15, 35-39]. A metasurface hologram is comparable to a hologram generated by an SLM. In both cases, the hologram is computed. The difference is that the pixels size of a metasurface hologram is smaller than the wavelength of light and that the nanoantennas of a metasurface have a higher degree of freedom in light shaping since SLMs generally only modulate the phase of the light. The metasurface antennas can be fabricated of plasmonic or dielectric materials, or a mixture of both. Depending on the size, shape, and material of an antenna, its scattering properties can be tailored, and the calculated hologram can be transferred into a suitable antenna pattern. Based on this, the following classes of holograms have emerged: phase-only holograms, amplitude-only holograms, and complex amplitude holograms [19, 40].

Phase-only holograms are holograms that modulate the spatial phase in the desired way by keeping the amplitude of transmitted or reflected waves constant. Among others, metasurfaces based on the Pancharatnam-Berry (PB) phase are perfect candidates for phase-only holograms. They generally consist of one type of subwavelength-sized resonators which all have the same amplitude response to the incident light. The phase information which is imprinted on the scattered light is stored in the spatial orientation of the resonators when illuminated with circularly polarized light. Plasmonic metasurfaces have been realized in reflection [41] or transmission mode [42] and can e. g. be used for three-dimensional image reconstruction (Figure 2.3a) [43]. Another alternative is the usage of all-dielectric metasurfaces. Dielectric nanostructures support electric and magnetic resonances which have been utilized to create metasurfaces based on silicon nanodiscs with spatially varying radii as the basis of a phase hologram [44].

Amplitude-only holograms are holograms that spatially vary the amplitude of the transmitted or reflected light. In metasurface holography, amplitude-only holograms are generally designed as binary-amplitude holograms, where the transmittance or reflectance can either be one or zero. Butt et al. used multi-walled carbon nanotubes in a two-dimensional arrangement, where they are located to define the transmittance pixelwise as 1 or 0 [45]. Another intuitive way to create a binary amplitude-hologram is presented by Huang et al. based on a photon sieve principle. The sample consists of a 100 nm thick chromium film with spatially distributed nanoholes (Figure 2.3b) [46]. The interference of the transmitted light results in the reconstructed holographic image.

Complex amplitude holograms are holograms that enable both amplitude and phase modulations by complex nanostructure arrangements. For instance, if the photon sieve's nanoholes are replaced by complex V-shaped apertures, both the amplitude and phase of the transmitted light

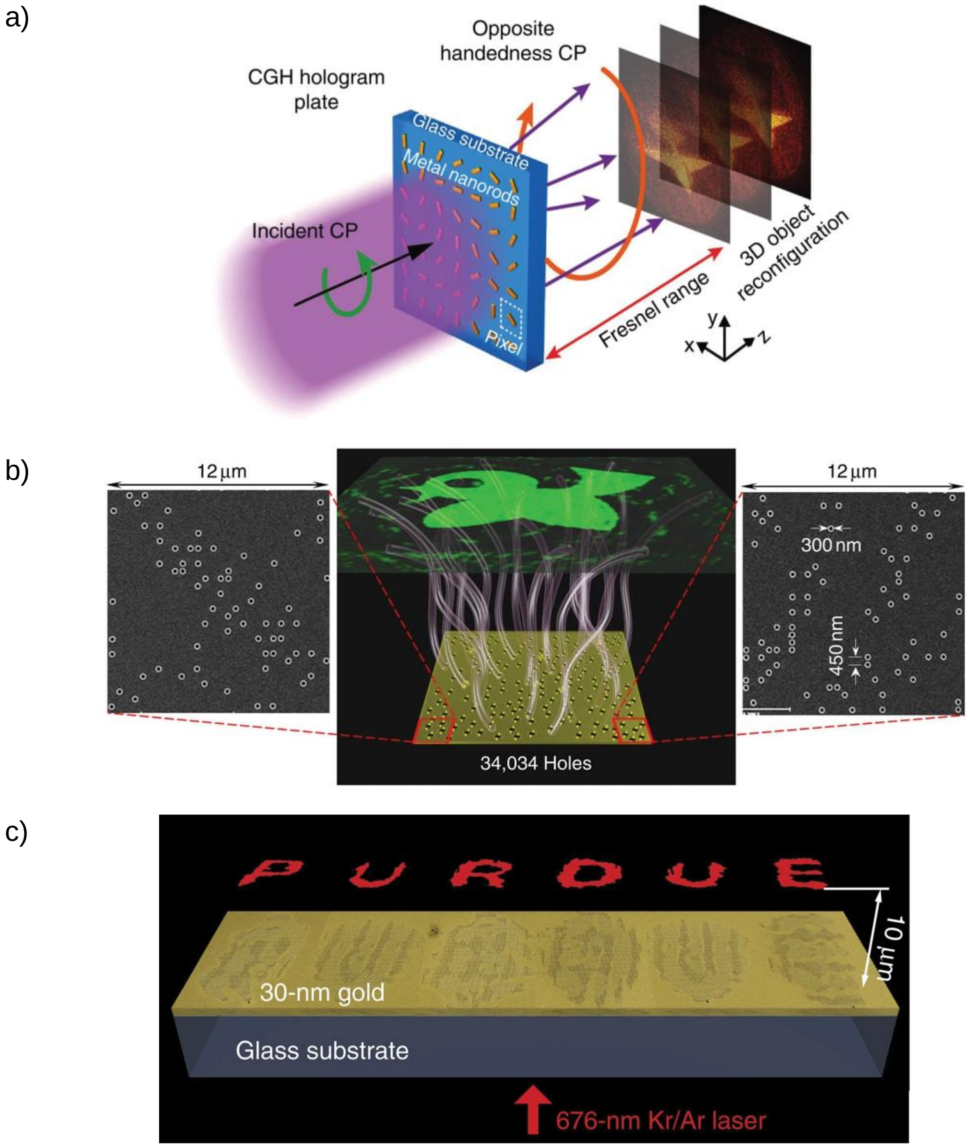

Figure 2.3 Examples of different hologram types. a) A three-dimensional phase-only hologram is realized based on the Pancharatnam-Berry phase. The spatial orientation of the nanorods store the phase-information of the 3D object [43]. b) Example of an amplitude-only hologram realized based on the photon sieve principle [46]. c) A complex amplitude hologram is realized by V-shaped apertures in a gold film [47].

can be modulated (Figure 2.3c) [47]. Moreover, dielectric nanostructures emerged as an attractive candidate to realize Huygens' metasurfaces with high transmittance and phase control [36]. By using silicon in a design of nanodiscs, the electric and magnetic moments within the small resonators can be tuned to obtain high transmittance. The phase modulation is implemented by spatially varying the diameter of the nanostructure along the metasurface [48, 49].

Beyond the three main classes of holograms, the research field has expanded to tailored applications and pushed forward to enlarge the space-bandwidth product of metasurface holograms by multiplexing techniques. Common techniques are color multiplexing and polarization multiplexing [8, 19]. An example for color holography is realized by the subdivision of a metasurface pixel in different subpixels for the primary colors red (R), green(G), and blue (B) (Figure 2.4a) [24]. A disadvantage of this method is the decreasing information density. PB metasurfaces can help to overcome this problem by utilizing one metaatom for more than one wavelength. Ye et al. realized a metasurface hologram based on split rings, which contains an image in the linear regime and two different images at the second harmonic wavelength in two different circularly polarized polarization channels (Figure 2.4b) [27].

a)

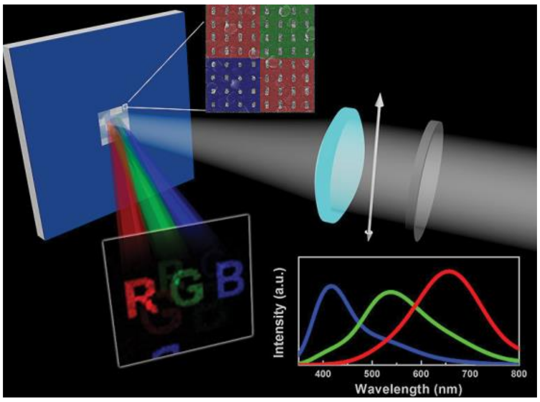

b)

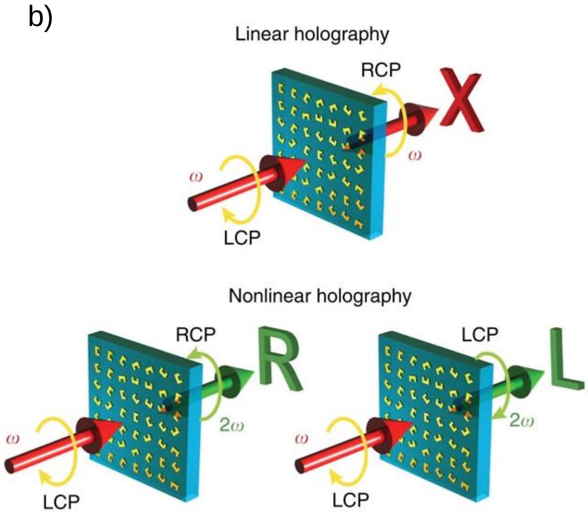

Figure 2.4 a) Example of an RGB metasurface hologram consisting of different aluminum nanoantennas designed for the colors red, green and blue [24]. b) A spin and wavelength multiplexed holographic metasurface. In the linear regime, the 'X' is encoded in the right circularly to lift circularly polarized polarization channel (LCP to RCP). The nonlinear holograms are reconstructed at frequency 2ω in the LCP to RCP ('R') and LCP to LCP ('L') channels [27].

2.3 Abrupt phase changes at optical interfaces – The generalized law of refraction

Metasurfaces are capable to introduce abrupt phase changes at optical interfaces which can be used for unique wavefront shaping. At an optical interface, refraction and reflection between two media follow Fermat's principle, which states that light propagating in a medium with varying refractive index $n(\boldsymbol{r})$ always takes the shortest optical path $\int_A^B n(\boldsymbol{r})\,dr$. In the case of two different optical media with refractive index n_i and n_t for an interface, Snell's law describes the refraction of a light beam when it propagates through the interface. The incident light beam in the medium with refractive index n_i enters the interface with the incident angle θ_i measured to the surface normal in the plane of incidence (Figure 2.5a). The refracted beam in the medium with refractive index n_t propagates in the plane of incidence but under the angel θ_t measured from the surface normal holding:

$$n_t \sin(\theta_t) - n_i \sin(\theta_i) = 0 \qquad (2.2)$$

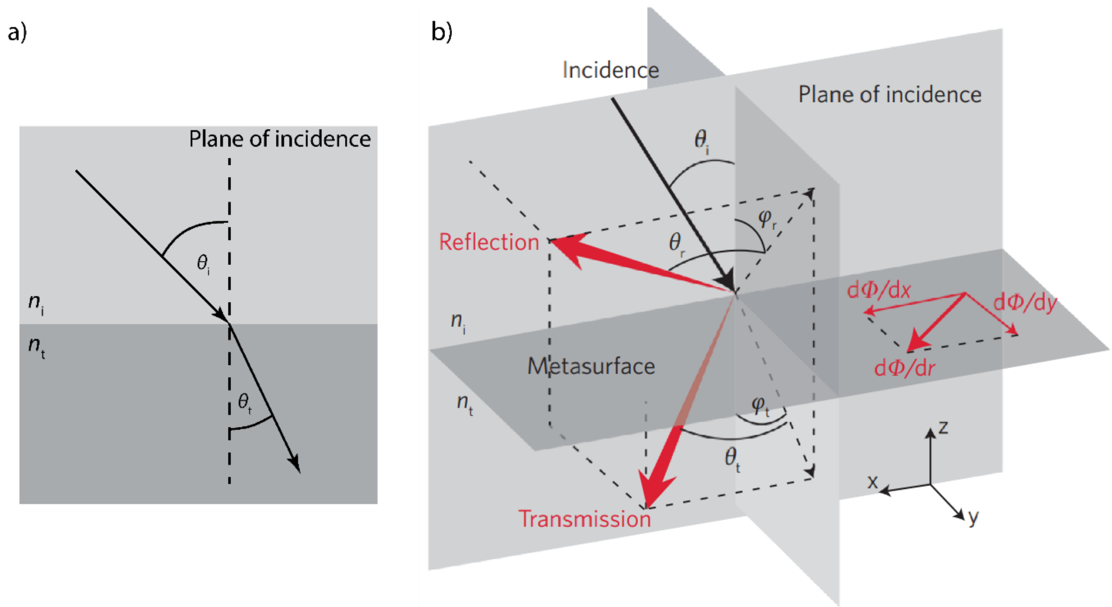

Figure 2.5 a) Depiction of Snell's law in a two-dimensional case. b) Illustration of the generalized Snell's law presented by Yu et al..The abrupt phase change at the optical interface can result in out-of-plane reflection and refraction [50].

In metasurface optics, it is possible to introduce abrupt local phase change $\Phi(r_s)$ depending on the coordinate r_s along the surface by a nanoscatterer. Thus, equation (2.2) would result in:

$$n_t \sin(\theta_t) - n_i \sin(\theta_i) = \frac{1}{k_0} \frac{d\Phi}{d\boldsymbol{r}} \tag{2.3}$$

where k_0 is the absolut wave vector of the incident light. This equation can be decomposed into the x-y direction and one can form the generalized law of refraction:

$$n_t \sin(\theta_t) - n_i \sin(\theta_i) = \frac{1}{k_0} \frac{d\Phi}{dx} \tag{2.4}$$

$$\cos(\theta_t) \sin(\varphi_t) = \frac{1}{n_t\, k_0} \frac{d\Phi}{dy}$$

and the generalized law of reflection:

$$n_i \sin(\theta_r) - n_i \sin(\theta_i) = \frac{1}{k_0} \frac{d\Phi}{dx} \tag{2.5}$$

$$\cos(\theta_t) \sin(\varphi_r) = \frac{1}{n_i\, k_0} \frac{d\Phi}{dx}.$$

with the out-of-plane deflection angles φ_t and φ_r [50]. In this sense, the total phase can be calculated by:

$$\varphi_{total} = \Phi(\boldsymbol{r_s}) + \int_A^B k_0\, n(\boldsymbol{r})\ dr, \tag{2.6}$$

where the total phase change φ_{total} between the two points, A and B, is the sum of the accumulated propagation phase $\int_A^B k_0\, n(\boldsymbol{r})\ dr$ and the abrupt phase change $\Phi(\boldsymbol{r_s})$ along with the interface [51].

In metasurface holography, the phase information which is generally calculated based on phase retrieval algorithms (see section 2.4), is typically the abrupt phase change $\Phi(\boldsymbol{r_s})$. This phase change can be introduced by plasmonic or dielectric nanoantennas in different ways. Principally, the physical properties of the nanoantennas are tuned so that each antenna satisfies the phase (and/or amplitude) change on the interface at the position $\boldsymbol{r_s}$.

2.4 The Gerchberg Saxton algorithm

The Gerchberg-Saxton (GS) algorithm is a widely used phase retrieval algorithm for beam shaping applications and information processing like metasurface holography. In 1972, R. W. Gerchberg and W. O. Saxton presented a rapid algorithm that enables the calculation of the phase distribution in the image and diffraction plane for a predefined amplitude. The method assumes that there is a Fourier transform relation between the light field in the image plane and the diffraction plane. [29]

In this thesis, I concentrate mainly on phase-only holograms in the Fourier space. Therefore, the GS algorithm forms a relatively easy-to-handle basis to calculate the phase distribution of a hologram. Figure 2.6 depicts the functionality of the iterative algorithm which is performed N times in a loop until the algorithm converges. Note, that the diffraction plane describes the near-field of the hologram and the image plane the far-field in which the hologram can be reconstructed.

First, the initialization is performed. The target image is defined as the amplitude of the hologram. In Figure 2.6, I use a dual-amplitude image of a coffee cup as a target image. The image has a resolution of 75 by 75 pixels. Each pixel has either an amplitude of one or zero. As an initial phase, a random phase distribution is recommended, because a constant initial phase mask can cause the algorithm to fail if the intensity pattern in the image and the diffraction plane is centrosymmetric [29].

In step 1, the amplitude and phase of the image plane are inversely Fourier transformed into the diffraction plane using the discrete inverse fast Fourier transform method (iFFT) [52].

In step 2, the amplitude in the diffraction plane will be replaced by an amplitude that corresponds more closely to the experiment. In the example, I use a plane wave. One can also use a Gaussian intensity profile. The calculated phase profile in the diffraction plane is the target phase of the Fourier hologram. This phase is maintained [29].

In step 3, the replaced amplitude and the target phase of the diffraction plane are fast Fourier transformed (FFT) to the image plane. The amplitude in the image plane is the reconstructed image of the Fourier hologram and resembles the predefined target image.

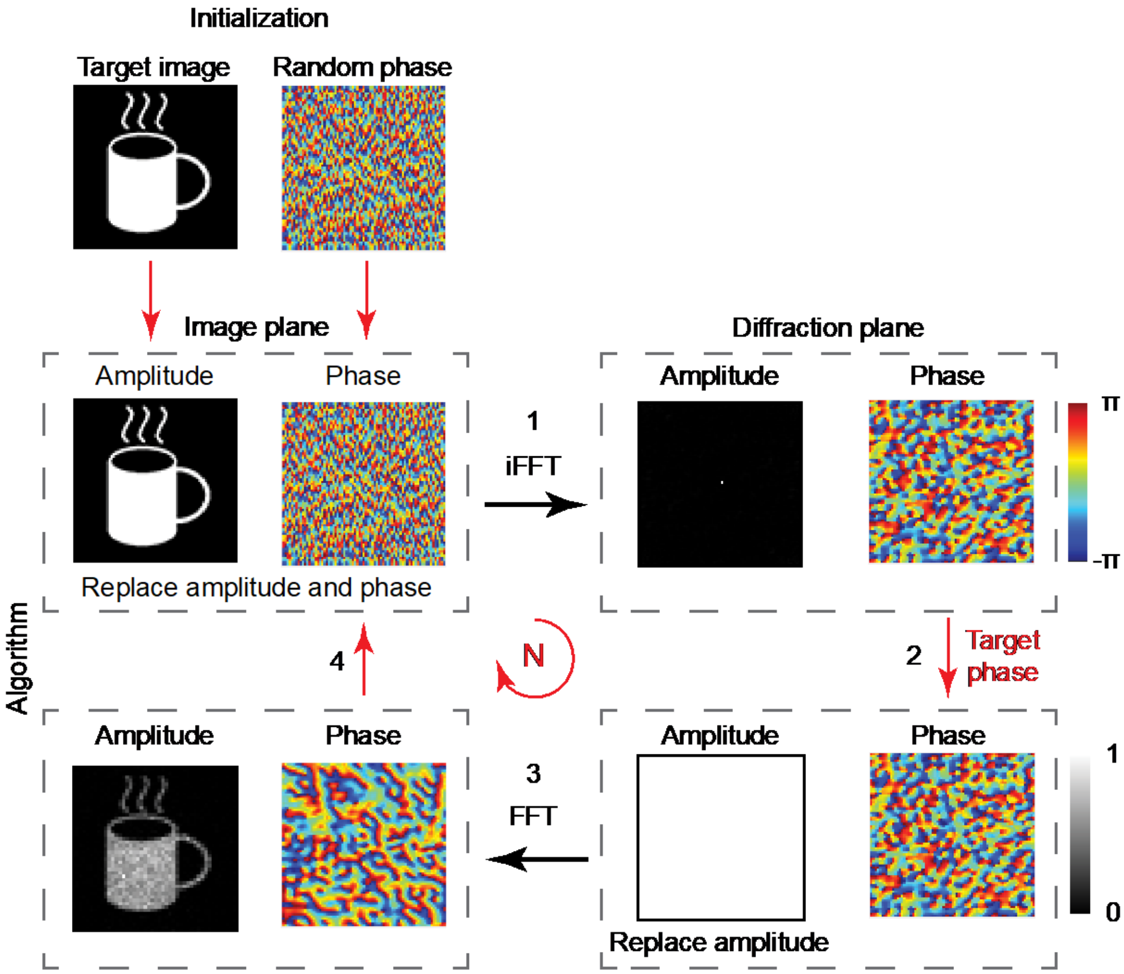

Figure 2.6) Illustration of the Gerchberg-Saxton algorithm. First, a target image and a random phase are used for the initialization in the image plane. The amplitude and phase are inversely Fourier transformed to the diffraction plane. Within the diffraction plane, the amplitude is replaced by a plane wave while the phase is maintained. After the diffraction plane is Fourier transformed to the image plane, the amplitude is replaced by the target image and the phase is maintained for the next iteration.

In step 4, the calculated amplitude in the image plane is replaced by the target image. The calculated phase in the diffraction plane is maintained and used for the next iteration of the algorithm, which is a better approach than the random phase distribution of the first iteration. Until the algorithm converges, the amplitude in the image plane approaches the target image more and more [29].

When the algorithm converges, one can take the calculated phase distribution of the diffraction plane and transfer it to the metasurface design. In this example, the metasurface would contain an array of 75 by 75 light nanoantennas. If the nanoantennas are tailored to imprint the desired phase and ideally transmit the light without any losses, one would expect the hologram image to look like the calculated amplitude in the image plane as illustrated in Figure 2.6 in the lower-left box.

2.5 Plasmonic metaatoms – Charge-on-a-spring model

Plasmonic metasurfaces are made of metallic nanoantennas and are often used as building blocks of metasurfaces. One of the simplest forms of antennas is a metallic bar. When an electromagnetic wave hits the bar with polarization along the long axis of the bar, the metal's free electrons start oscillating back and forth. These electron movements excite localized surface plasmon polaritons. Under certain conditions, the bar supports a dipole moment at its resonance frequency. Two typical features of this kind of optical resonator are that the scattered electric field reaches its maximum at the resonance frequency and that it undergoes a π phase change over the resonator's resonance [53].

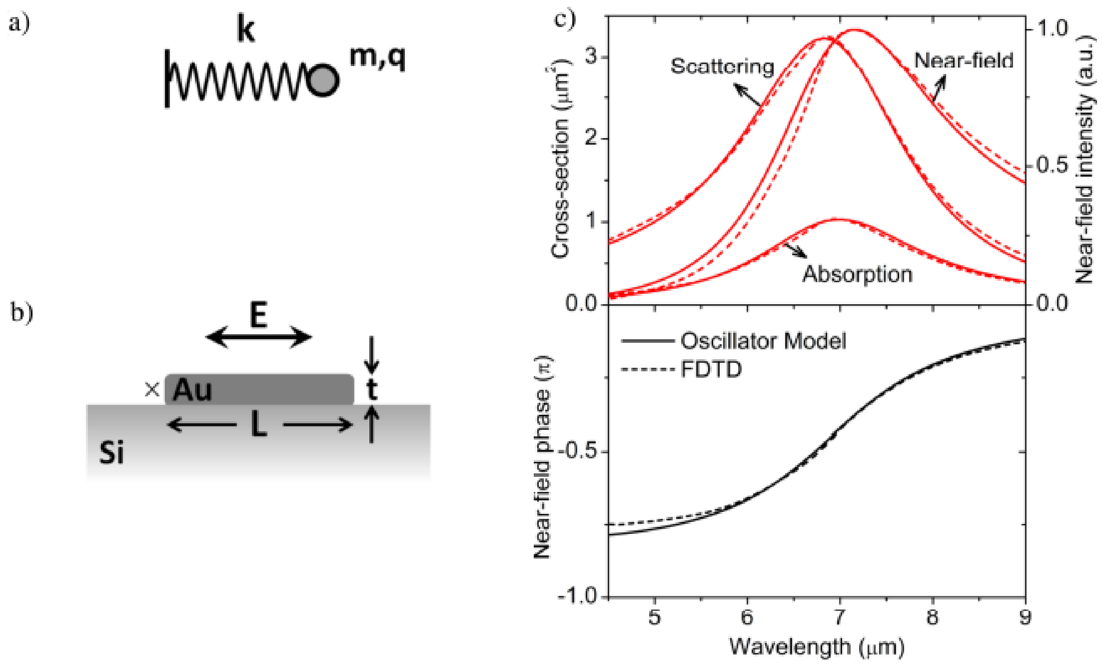

Figure 2.7 a) Simple model of an electron with charge q and mass m on a spring with spring constant k. b) Antenna model for the FDTD simulations with antenna arm length L = 1 µm, antenna thickness t = 50 nm and antenna width of w = 130 nm. c) Upper panel: Calculated scattering cross-section, absorption cross-section, and near-field intensity by the FDTD simulation (dashed line) and oscillator model (solid line). Lower panel: Introduced near-field phase over the exciting wavelength. The calculations are performed by Yu et al [54].

The electron oscillations, the scattering behavior, the near-field behavior, and the phase changes can be described by an oscillator model as presented by Yu et al. [54]. The model treats the light-matter interaction as a charge on a spring as illustrated in Figure 2.7a. When an electric field $\tilde{E} = E_0 e^{i\omega t}$ interacts with the long antenna axis as illustrated in Figure 2.7b, the electrons start oscillating. In the charge-on-the-spring model, the electrons experience a restoring force $F(t) = k \cdot x(t)$ by the spring, a damping force $F_{abs}(\omega, t) = -\Gamma_{abs} dx/dt$, and an additional radiation force $F_{scat}(\omega, t) = -\Gamma_{scat} d^3x/dt^3$, where $\Gamma_{scat} = \frac{q^2}{6\pi\epsilon_0 c^3}$. The radiation force is the force which an accelerated electron feels when it emits radiation that carries away momentum and depends on the change of the acceleration. It is known as the Abraham-Lorentz force [55]. The equation of motion results in

$$m\frac{d^2x}{dt^2} + \Gamma_{abs}\frac{dx}{dt} + kx = qE_0 e^{i\omega t} - \Gamma_{scat}\frac{d^3x}{dt^3}. \tag{2.7}$$

By assuming a harmonic oscillation $x(\omega, t) = x(\omega)e^{i\omega t}$, a solution of equation (2.7) is

$$x(\omega, t) = \frac{(q/m)E_0}{(\omega_0^2 - \omega^2) + i\frac{\omega}{m}(\Gamma_{abs} + \omega^2\Gamma_{scat})}\, e^{i\omega t} = x_0(\omega)e^{i\omega t} \tag{2.8}$$

with $\omega_0 = \sqrt{k/m}$. The time-averaged dissipated power can be written as $P(\omega) = F(\omega)^* \left(i\omega x_0(\omega)\right)$ where $F(\omega)^*$ is the complex conjugate of the applied force. Using the equations (2.7) and (2.8) leads to an expression for the time-averaged absorbed power $P_{abs}(\omega)$ and the time-averaged scattering power $P_{sact}(\omega)$ resulting in

$$P_{abs}(\omega) = F_{abs}(\omega, t)^*(i\omega x(\omega, t)) = \omega^2\Gamma_{abs}|x(\omega)|^2 \tag{2.9}$$

$$P_{scat}(\omega) = F_{scat}(\omega, t)^*\left(i\omega x(\omega, t)\right) = \omega^4\Gamma_{scat}|x(\omega)|^2$$

The absorption power P_{abs} and the scattering power P_{scat} can be associated with the absorption and scattering spectra as illustrated in Figure 2.7c. The charge-on-a-spring model is compared with finite-difference time-domain (FDTD) simulations of a gold nanoantenna placed on a silicon substrate. The near-field enhancement at the end of the antenna arm (marked by the cross in Figure 2.7b) is $|E_{near}(\omega)|^2 \propto |x(\omega)|^2$. By considering $P_{scat}(\omega) \propto \omega^2 P_{abs}(\omega) \propto$

$\omega^4|E_{near}(\omega)|^2$, one finds that P_{scat} is blue-shifted to P_{abs}, which is blue-shifted to the near-field spectrum $|E_{near}(\omega)|^2$. This is in agreement with the experimental observations that the near-field enhancement of the electrical field can be red-shifted compared to the far-field spectra [54]. In linear metasurface holograms, the shift between the near- and far-field spectra is not of high interest. However, in nonlinear plasmonic metasurfaces, the nonlinear processes at the nanoantennas depend on the electric near-field enhancements. Hence, considering this model, one cannot assume that the strongest nonlinear signal appears at the wavelength where the linear nanoantenna absorption is maximum. One would expect that the strongest nonlinear response is red-shifted compared to the absorption maximum.

2.5.1 The resonance phase approach

From the charge-on-a-spring model and the FDTD-simulation, one can find a π phase shift that can be introduced over the antenna's resonance. This phase shift is useful for metasurface applications and is known as the resonance phase approach. To expand the phase range, one can exploit the eigenmodes of anisotropic plasmonic antennas. V-shaped antennas which are characterized by their arm length h and the opening angle Δ as illustrated in Figure 2.8, are often described by a double-oscillator model. These kinds of antennas support symmetric and antisymmetric modes which are excited by an electric field E_{inc} parallel or perpendicular to the V-shaped antenna's symmetry axis $\hat{s}$. The resulting two resonance frequencies which differ by a factor of two can cover the full phase range from 0 to 2π by carefully designing the shape of the antennas [54, 56, 57]. Hence, one can obtain destructive and constructive interference of light scattered by this kind of antenna.

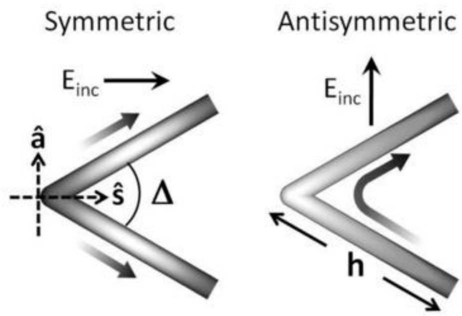

Figure 2.8 An example of a V-shaped antenna excitation. The antenna is defined by its armlength h and the opening angle Δ. When the incoming electric field E_{inc} is parallel to the unit vector $\hat{s}$, the symmetric mode is excited. When the incoming electric field is parallel to the unit vector $\hat{a}$, the antisymmetric mode is excited. The schematic current distribution is in gray scale, where lighter tones indicate larger current density [54].

2.5.2 The Pancharatnam-Berry phase approach for circularly polarized light

Another approach to introducing a 2π phase range is to utilize the Pancharatnam-Berry phase which is based on spatially varying antenna rotations of antennas exposed by circularly polarized light $E^{\sigma} = \frac{1}{\sqrt{2}} E_0 (e_x + i\sigma e_y)$, where $\sigma = \pm 1$ represents the right- or left-circular polarization state (LCP and RCP). Assuming a mirror-symmetric dipole antenna rotated by the angle θ as illustrated in Figure 2.9, the reflection and transmission tensors can be represented in a diagonal form as $\bar{\bar{M}} = diag(M_{xx}, M_{yy})$. For the rotated antenna, the matrix will be transformed to

$$\bar{\bar{M}}_{\theta} = \begin{pmatrix} \cos(\theta) & -\sin(\theta) \\ \sin(\theta) & \cos(\theta) \end{pmatrix} \begin{pmatrix} M_{xx} & 0 \\ 0 & M_{yy} \end{pmatrix} \begin{pmatrix} \cos(\theta) & \sin(\theta) \\ -\sin(\theta) & \cos(\theta) \end{pmatrix}. \tag{2.10}$$

M_{xx} and M_{yy} represent the complex scattering coefficients for light in the linear polarization basis in the x and y-direction. The reflected or transmitted light can be described by

$$\bar{\bar{M}}_{\theta} \cdot E^{\sigma} = \frac{1}{2}(M_{xx} + M_{yy})E^{\sigma} + \frac{1}{2}(M_{xx} - M_{yy})e^{i2\sigma\theta}E^{-\sigma}. \tag{2.11}$$

The first term of equation (2.11) represents scattered light with the same-handedness as the incident wave, while the second term represents light scattered with the opposite-handedness, which gains an additional phase equal to $2\sigma\theta$. This phase is called the Pancharatnam-Berry phase. The sign of the introduced phase depends on the handedness σ of the incident light field E^{σ}. The acquired phase cover a range from 0 to 2π for an antenna rotation from 0° to 180° [58].

The PB phase approach is used in many metasurface applications for spatial phase control along metasurfaces [32, 59-64]. The concept can also be applied to the nonlinear regime and will be

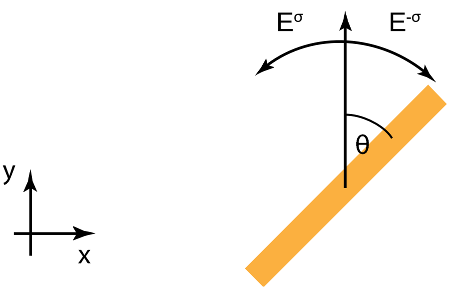

Figure 2.9 Illustration of the PB phase using a dipole antenna. When the antenna rotated by the angle of θ is illuminated with circularly polarized light E^{σ}, the phase difference which is introduced by the rotation θ between the two polarization states E^{σ} and $E^{-\sigma}$ is $\varphi = 2\sigma\theta$.

presented in a later section (see 5.2 Symmetry selection rules for circularly polarized harmonic generations).

2.6 Antenna design based on finite-difference time-domain simulations

To tune the resonance of different nanoantenna types, I use the commercial software package CST microwave studios. Within the software, one can create a 3D model of an antenna and assign different material parameters, define excitation sources and place electric and magnetic field probes and monitors [65, 66]. An example of a plasmonic dipole antenna is illustrated in Figure 2.10a. The antenna is defined by length L = 310 nm, width W = 70 nm and height H = 30 nm. As material parameter ε_A for the gold antenna, I use the experimentally measured values by Johnson and Christy [67]. The upper half-space is set to vacuum. The substrate dimensions are S_x = 500 nm, S_y = 500 nm, and S_z = 150 nm. Using periodic boundary conditions, the S_x and S_y define the unit cell dimensions in the x-y plane. The chosen refractive index of the substrate is n = 1.4 ($\varepsilon_A = n^2 = 1.96$).

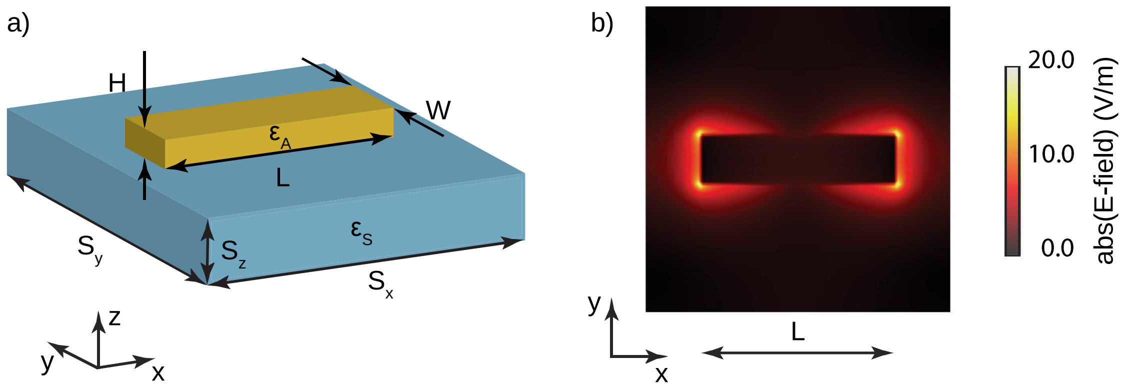

Figure 2.10 a) 3D model of a gold antenna on a substrate. The antenna is defined by its dimensions L, W, and H. The substrate dimensions are S_x, S_y, and S_z. The material parameter of the antenna and the substrate are ε_A and ε_S, respectively. b) Absolute electric field in the x-y plane in the middle of the plasmonic antenna, 15 nm above the substrate.

To optically excite the antenna, a plane wave source is selected with a field amplitude of 1 V/m, illuminating the antenna from the vacuum side and propagating in the z-direction. The source is linearly polarized along the antenna arm length L (x-direction). The investigated wavelength range is 900 nm to 1700 nm. The software calculates the evolution of the fields over time at discrete locations and times. The mesh which defines the discrete points in space is typically set to 40 cells per wavelength but can be chosen higher near the surface of the antennas where field enhancements occur. An electric field monitor can be set to record the electric field vectors for a given wavelength within the mesh cells. Figure 2.10b illustrates the absolute electric field in the x-y plane in the middle of the antenna (15 nm above the substrate) for a wavelength of 1300 nm. One can see that field enhancements occur near the surface of the antenna. Near the unit cells boundary the field strongly attenuates, so coupling between neighboring antennas can be excluded for the time being.

The design process for a nanoantenna is to match the resonance wavelength, as well as the width and strength of the resonance dip for an application. Therefore, the antenna dimensions L, W, and H are swept in a predefined parameter space and the transmittance for each set of parameters is calculated. In this example, the parameter space for the sweep is: L = (290 nm, 310 nm, 330 nm), H = (20 nm, 30 nm, 40 nm), and W = (60 nm, 70 nm, 80 nm). Figure 2.11a-c illustrates

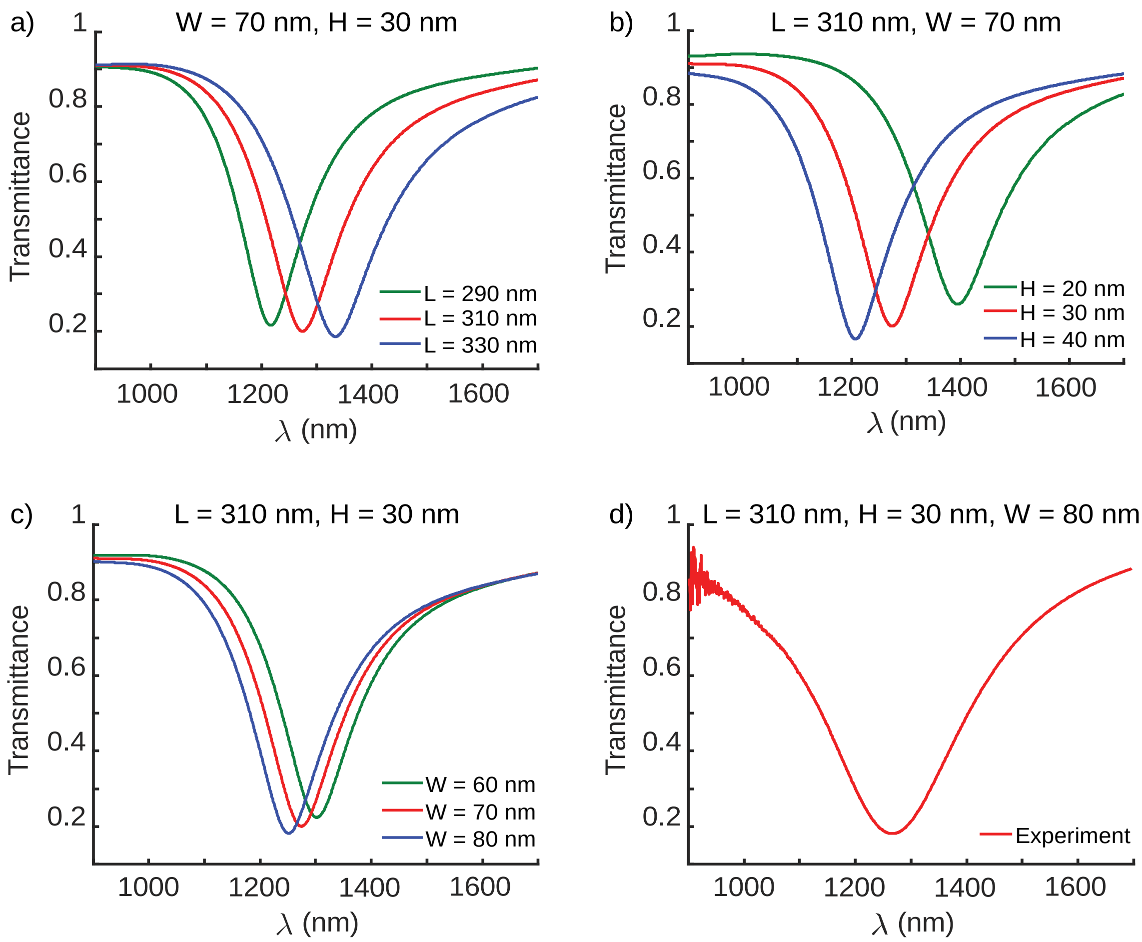

Figure 2.11 a) Calculated transmittance for a plasmonic antenna with fixed width and height for different arm length. b) Calculated transmittance for a plasmonic antenna with fixed length and width for different antenna heights. c) Calculated transmittance for a plasmonic antenna with fixed length and height for different antenna widths. d) Experimentally measured transmittance of a plasmonic antenna array with antenna dimensions L = 310 nm, W = 80 nm, and H = 30 nm.

how the resonance dip of the antenna with the dimensions L = 310 nm, W = 70 nm, and H = 30 nm behaves when the parameter L, W, and H are slightly decreased or increased.

In Figure 2.11a, the antenna width W = 70 nm and height H = 30 nm are constant, while the arm length L changes (310 nm ± 20 nm). One can see that the change in the arm length L predominantly influences the resonance wavelength of the dip. For shorter L the resonance shifts to a shorter wavelength, while for larger L the resonance shits to a longer wavelength. The transmittance only decreases slightly with increasing length L.

The impact of the change in the antenna height H = 30 nm ± 10 nm for constant L = 310 nm and W = 70 nm is shown in Figure 2.11b. In this case, the resonance dip shifts to a lower wavelength for an increasing height H. The transmittance also decreases for the increasing height of the antenna.

The change in the antenna width W = 70 nm ± 10 nm is illustrated in Figure 2.11. The antenna length and height are L = 310 nm and H = 30 nm, respectively. One can see that the resonance dips slightly shift to a shorter wavelength for increasing width W. The transmittance also decreases for increasing W.

The parameter space is only a small section around the antenna dimensions L = 310 nm, W = 70 nm, and H = 30 nm which cannot describe the parameter impact in general. However, from the plots in Figure 2.11a-c, one can see that the antenna arm length predominantly influences the resonance wavelength of the antenna by only slightly changing the transmittance. Thus, I generally change only the antenna armlength L when fabricating the first test sample for a fixed antenna width W = 70 nm and height H = 30 nm, to find out if the experiment satisfies the simulated design. The experimentally measured plasmonic nanoantenna array with antenna dimensions of L= 310 nm, W = 80 nm, and H = 30 nm is shown in Figure 2.11d. The transmittance is measured using a Fourier transform infrared (FTIR) spectrometer. The incident light is linearly polarized along the long antenna axis. One can see that the resonance wavelength is red-shifted and broadened compared to the simulation. This may be due to two reasons. First, the material parameters used in the simulations differ from the real system. Higher losses in the fabricated system can influence the resonance of the metasurface. Second, the fabricated metasurface underlay fabrication tolerances. Thus, the size of the antennas of the metasurface varies and averaging over all antenna sizes leads to a broadening and shifting of the resonance.

The design process can also be done for other geometries, as well as for other materials like dielectric nanostructures.

2.7 All-dielectric metaatoms for metasurface applications

All-dielectric metaatoms are the counterparts of plasmonic metaatoms. The basic mechanism of the excitation of a plasmonic split ring resonator and spherical dielectric nano particles is very similar and illustrated in Figure 2.12a and b. When the split ring resonator is excited by electromagnetic radiation, currents are generated along the resonator and a transverse magnetic dipole starts oscillating in the center of the split ring. The drawback of these plasmonic nanostructures is, that high ohmic losses occur when the structures are designed for the visible spectrum of light due to the excitation of intraband transitions in the metals [68-70].

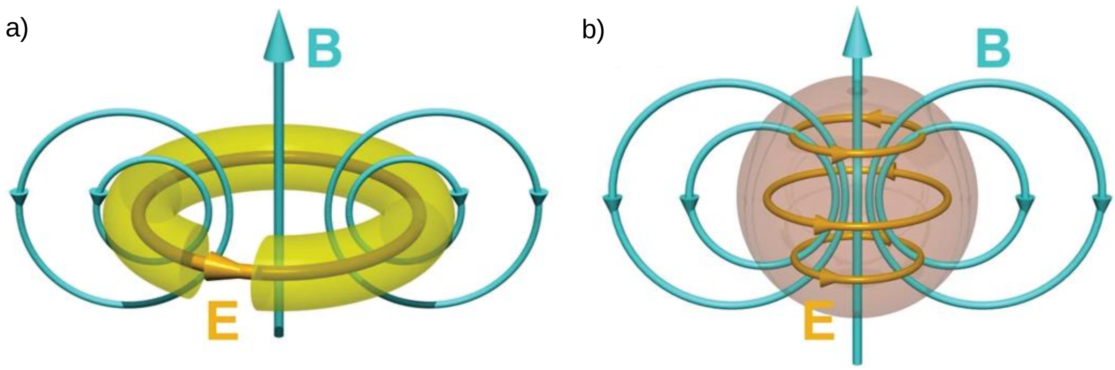

Figure 2.12 Schematic illustration of the electric and magnetic field distributions inside a a) plasmonic split ring resonator and b) dielectric spherical nanoparticle. The electric fields E and the magnetic fields B are illustrated in yellow and blue [69].

An alternative approach to overcome the high losses in plasmonic antennas and to achieve strong magnetic resonances in nano particles is the choice of another material system. From Mie theory of light scattering, one can find that strong electric and magnetic resonances can be achieved in spherical particles. Imagine a dielectric nanosphere with diameter d and refractive index n_s: If the size of the nanosphere is comparable with the wavelength of light $\lambda = n_s \cdot d$, the first resonance is the magnetic dipole resonance supported by the structure. The up and down oscillating magnetic field in the middle of the structure is coupled to displacement currents within the structure (Figure 2.12b). Moreover, multipolar modes which can be excited in the particle become important for the manipulation of the radiation pattern [71, 72].

By approaching the spherical particles through nano discs (which are much easier to fabricate) one can overlap electric and magnetic modes with equal strength to create Huygens' metasurfaces with high transmission efficiencies of 55% and simultaneously provide a 0 to 2π phase coverage [49]. Waveplates with even higher transmission about 90 % are also reported [73]. Those dielectric or high contrast materials appear as attractive candidates for metasurface applications like holography [74, 75], polarization converters[76], or lenses[16, 77-79]

2.8 Fabrication procedure of metasurfaces

So far it has been mentioned that the nanoantennas have dimensions of the light's wavelength or lower. To fabricate such small structures, standard electron-beam lithography (EBL) processes, thin-film deposition techniques like electron-beam evaporation, and plasma-enhanced chemical vapor deposition (PECVD), as well as inductively coupled reactive ion etching (ICP-RIE) are used.

2.8.1 Plasmonic metasurface fabrication

As substrate for the plasmonic nanostructures, 1 mm thick fused quartz glass is used (Figure 2.13a). To prepare the substrate for the photoresist coating, it is cleaned chemically by placing

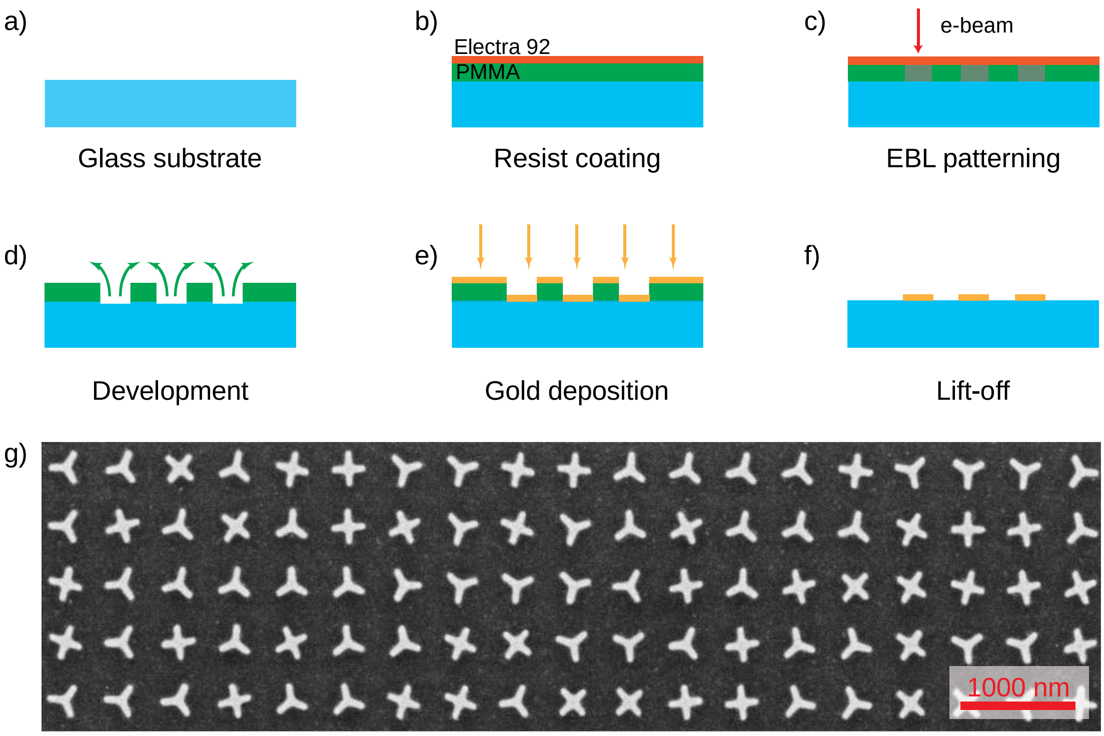

Figure 2.13 General fabrication process for planar nanostructures. a) The substrate is cleaned by acetone and isopropanol. b) PMMA and Electra 92 is spin-coated onto the substrate. c) The metasurface pattern is written into the PMMA by EBL. d) Developing of the patterned PMMA, e) deposition of Cr and Au, and f) final plasmonic metasurface after a lift-off process. g) The SEM image shows an example of a fabricated plasmonic metasurface.

the sample in a mixture of acetone and isopropanol. The cleaning is assisted by an ultrasonic bath at 80 kHz for a minimum of 5 minutes. After the sonication, the sample is rinsed with demineralized water and dried with nitrogen. As e-beam resist a 150 nm thick poly-methylene-methacrylate (PMMA 950K, AR-P 679.03) layer is used and spin-coated with 4000 rotations per minute (rpm) for 60 s on the substrate. After the spin-coating, the resist is baked on a hot plate at 180 °C for 120 s. On top of the PMMA, the conductive coating AR-PC 5090.02 (Electra 92) is spin-coated with 5000 rpm for 60 s and baked at 90 °C for 120 s (Figure 2.13b). The conductive coating ensures that the substrate is not charged during the EBL process. The desired metasurface pattern is transferred to the e-beam resist based on an EBL process. The EBL system is typically used with an acceleration voltage of 20 kV, which requires an area dose between 150 $\frac{\mu C}{cm^2}$ and 250 $\frac{\mu C}{cm^2}$ for the used e-beam resist. Note that the dose varies depending on the antenna density, size, and shape within the pattern (Figure 2.13c). After patterning, the conductive layer is removed by placing the sample in water for 30 s. The development is done using the developer AR 600-56 for 90 s, followed by 30 s in isopropanol (Figure 2.13 d). The developed patterning is deposited with 1 nm to 2 nm of chromium (Cr) as an adhesive layer, followed by 30 nm to 50 nm of gold (Au), depending on the antenna design (Figure 2.13e). The deposition is done using an electron-beam evaporator and a deposition rate of 1 Å/s for Cr and for Au. The pressure at the beginning of the deposition is typically below $7 \cdot 10^{-7}$ mbar. The lift-off is done in acetone. If the structure of the EBL pattern is very dense, the lift-off can profit from increasing the temperature and/or the usage of an ultrasonic bath (80 kHz). The acetone can be heated up to 75 °C on a hot plate. An SEM image of a final structure is shown in (Figure 2.13g).

2.8.2 Dielectric metasurface fabrication

The fabrication of a dielectric metasurface is a multistep process comprising deposition, patterning, lift-off, and reactive ion etching. In this thesis, the metasurface is made of amorphous silicon (a-Si). First, a 300 nm thick amorphous silicon film is deposited on a glass substrate by PECVD using silane (SiH_4) diluted in argon (Ar) plasma (SiH_4/Ar = 2/98). The deposition parameters are listed in Table 2.1 (PECVD). The desired pattern is then transferred onto the silicon by using a standard EBL process, the subsequent deposition of Cr as the mask (50 nm), lift-off in hot acetone (75 °C) as explained in section 2.8.1 and ICP-RIE. For the ICP-RIE process, the etching gas (Sulfur hexafluoride (SF6)) for silicon and a passivation gas (Octafluorocyclobutane (C_4F_8)) are combined in the same plasma. The details of the plasma etching parameters are listed in Table 2.2 (ICP-RIE). The residual chromium mask is removed by placing the sample inside a Cr etching solution

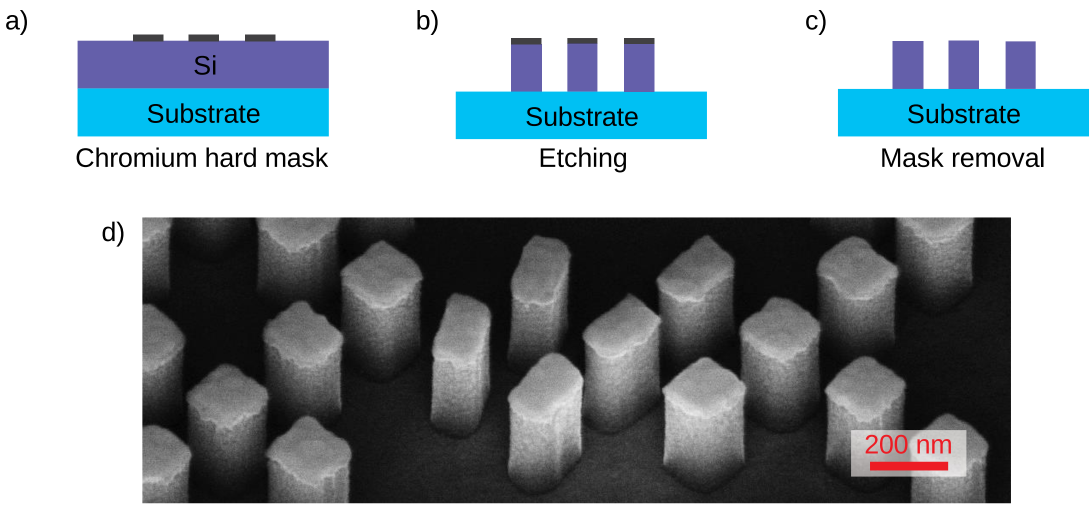

Figure 2.14 Etching nano structures out of silicon. a) The metasurface pattern is transferred to a Cr etching mask. b) During the ICP-RIE process, the uncovered area of the Si film is etched to the substrate. c) The Cr etching mask is removed by wet etching. d) An SEM image of a fabricated silicon metasurface.

(TechniEtch Cr01, components: $(NH_4)_2[Ce(NO_3)_6]/HClO_4$). The final sample consists of anisotropically etched individual silicon nanostructures following a specific pattern on the glass substrate (Figure 2.14c). An SEM image of an etched silicon metasurface is shown in Figure 2.14d. In the image, the chromium mask is still sitting on top of the silicon antennas.

PECVD				
Material	Gases flow rate	RF-Power (W)	Pressure (mTorr)	Temperature (°C)
a-Si (deposition)	SiH_4/Ar (2/98) = 400 sccm	10	1000	300

Table 2.1 List of the process parameters for the deposition of a-silicon using PECVD.

ICP-RIE					
Material	Gases flow rate	RF-Power (W)	ICP-Power (W)	Pressure (mTorr)	Temperatutr (°C)
a-Si (etching)	SF_6 = 18 sccm, and C_4F_8 = 45 sccm	41	900	10	12

Table 2.2 List of the process parameters for the etching of the silicon nanoantennas using ICP-RIE.

2.8.3 Overlay lithography

In this thesis, overlay lithography is used to stack several metasurface layers on top of each other with a 50 nm thick dielectric spacer in between. What happens when an overlay process fails is illustrated in the SEM images in Figure 2.15: In Figure 2.15a, two layers of plasmonic nanoantennas are aligned so that the unit cells of the bottom layer overlap with the unit cells of the top layer. The mismatch is neglectably small and can be estimated to ± 50 nm in the x-y plane. In Figure 2.15b, the overlay process failed. In this case, the mismatch in the x-y plane is Δx = 1850 nm ± 50 nm and Δy = 2012 nm ± 50 nm, respectively.

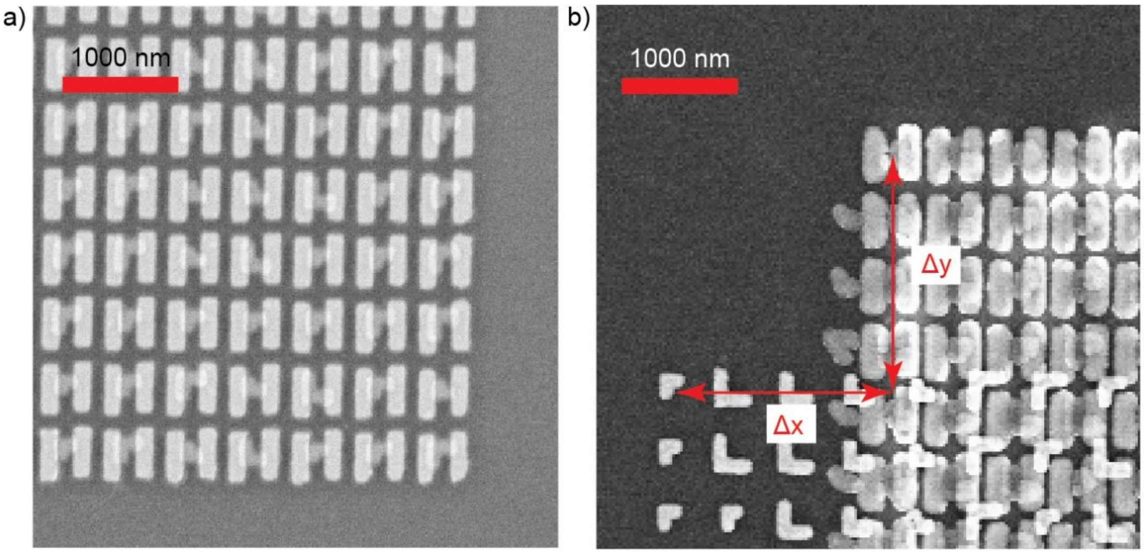

Figure 2.15 a) Illustration of stacked plasmonic nanoantennas separated by 50 nm of SiO_2 using overlay lithography with a local marker system. b) Illustration of a failed overlay of the third layer of a plasmonic metasurface. The mismatch is indicated by the arrows Δx and Δy.

The used lithography system divides the pattern into several writing fields. The different writing fields, including the nanoantenna designs, are placed on desired positions within a global coordinate system. The global coordinate system is defined by global markers which are placed on the sample surface. Within a writing field, the electron beam can be deflected without moving mechanical components like the stage which moves the sample in position. The lateral accuracy for the antenna positioning within a writing field is the highest that can be achieved by the system. However, if the pattern is larger than the writing field, which is typically 100 µm by 100 µm, the system divides the pattern into several writing fields and moves the sample mechanically to the next writing field position. Each mechanical movement causes additional alignment errors. These errors can be minimized by alignment processes.

Overlay lithography is a tool to place several layers of nanostructures at desired positions with high accuracy. Therefore, one has to place local markers within a writing field. Typically, the local markers define the corners of each writing field as illustrated in Figure 2.16. Layer 1 contains the local markers and an arbitrary pattern which is fabricated in the first fabrication step. After the lithography process, the sample is processed as described in section 2.8.1 or 2.8.2, depending on the metasurface design. If the second layer of nanostructures has to be fabricated in close proximity or on top of layer 1, the local markers can be scanned to align layer 2 on top of layer 1. Typically, alignment accuracies of about ± 20 nm can be realized [80].

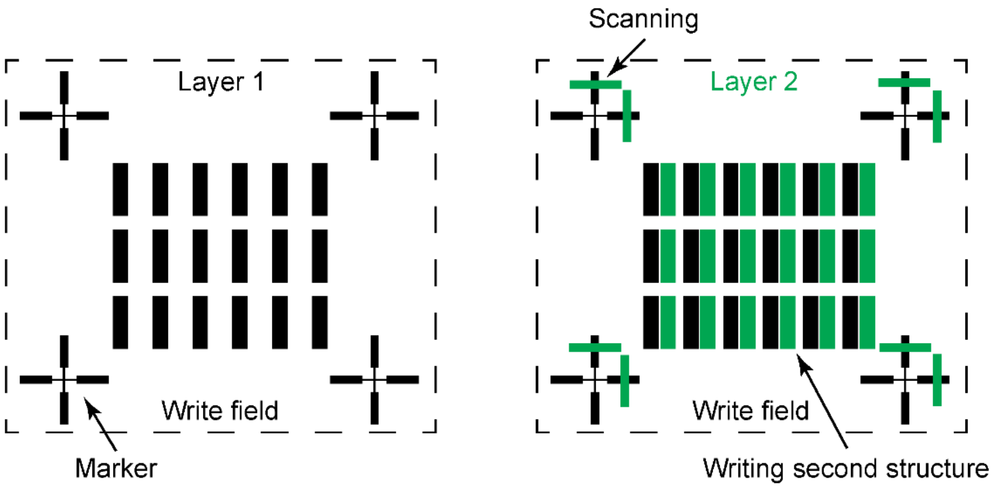

Figure 2.16 Diagram of two writing fields (dashed lines) for overlay lithography. In layer 1, the pattern (black) including markers are written by electron-beam lithography. After further processing, the overlay can be aligned by scanning the arms of the markers. The second pattern (green) can be placed with high lateral accuracy in layer 2.

2.9 Fourier plane imaging

Fourier plane imaging (also called back-focal plane imaging) is a technique to measure the angular emission pattern of a sample or light source. In contrast to real-space imaging, where the image is measured in spatial coordinates, the Fourier plane image gives information about the wavevector distribution of the sample [81]. The applications of Fourier plane imaging range from the measurement of radiation patterns of quantum emitters [82, 83] to the investigation of nanoantenna radiation [84], Fourier holograms, and many more.

The general setup for Fourier imaging is depicted in Figure 2.17. The sample or object is placed in the focal spot of a microscope objective (MO). The MO images the diffraction plane of the sample to its back-focal plane at position f_{MO}'. The back-focal plane contains information about the wavevector distribution of the sample. It is the Fourier transform of the sample surface from the real space (x and y-coordinates) to the momentum space (k_x and k_y-coordinates).

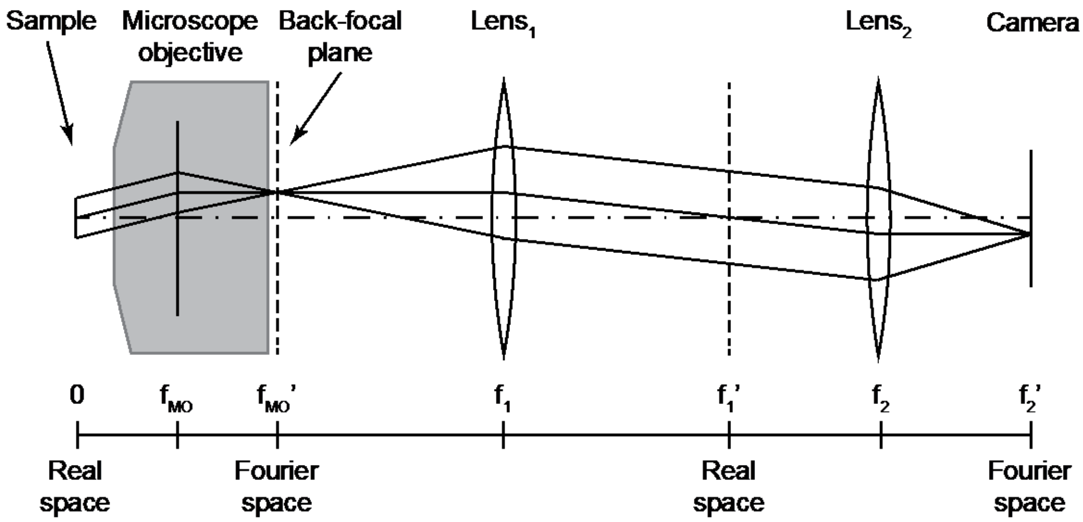

Figure 2.17 Scheme of Fourier imaging using a MO and two lenses. The sample is placed in the focal point of the MO. The diffraction plane of the sample is imaged on the back-focal plane of the MO. The back-focal plane is imaged on a camera using two lenses Lens 1 and Lens 2. In the area of focus between Lens 1 and Lens 2, the real space image of the sample appears. These plane enables spatial filtering.

Since the back-focal plane of an MO is usually within the housing of the MO, one has to image it to a camera by using two additional lenses in the 4f-arrangement. The focal point of Lens 1 is placed on the back-focal plane of the MO. Lens 1 transforms the Fourier space back to the real space at position f_1'. An observer would see the sample surface at this position. The real-space plane can be used to perform spatial filtering. By using apertures, one can spatially define areas that should be investigated and block signals which would result in noise. The real space at position f_1' behind Lens 1 is again Fourier transformed by Lens 2. At the position f_2', the Fourier image can be captured by using a camera.

In this thesis, Fourier-holograms are encoded into different metasurface designs. To reconstruct those holograms, Fourier-plane imaging based on the 4f-setup is used. Note that the measured angular range is limited by the numerical aperture of the MO. The maximum angel α measured from the optical axis which can be collected by an MO with numerical aperture NA in a surrounding medium with refractive index n is $\alpha = \sin^{-1}\left(\frac{NA}{n}\right)$. Thus, by designing an optical metasurface, one has to consider the setup so that the whole holographic image can be measured.

3 Directional holographic applications

Single-layer metasurfaces consisting of planar meta-atoms are widely used to introduce abrupt phase changes at interfaces. Those two-dimensional metasurfaces mostly exhibit weak spatial symmetry in the propagation direction of the light. As a result, they have mostly symmetric transmission features. To realize an asymmetric transmission feature in metasurfaces, it is essential to break the symmetry of the structure in the propagation direction of the light [85, 86].

Nonreciprocal optical devices like optical isolators are a prominent example of optical components which allow asymmetric transmission of light [87]. This feature can be realized based on the Faraday effect, which is utilized to protect laser cavities from back reflections [88]. In the case of linearly polarized light, one can combine two linear polarizers with a Faraday rotator between them to build an optical isolator. If the input polarizer is arranged parallel to the laser light, for instance vertically, it will pass through the Faraday rotator. The faraday rotator consists of a magnetooptical material and is designed to rotate the linear polarized light clockwise by 45 degree when a magnetic field B is applied parallel to the propagation direction of the light [89]. The output polarizer (analyzer) is also rotated by 45°, so that the light can propagate in a forward direction. In the backward propagation direction, light becomes polarized linearly at 45° by the analyzer. The Faraday rotator will again rotate the backward propagating light by 45°, resulting in horizontally polarized light, which will be blocked by the vertically arranged input polarizer.

Now the question arises, how directional optical properties can be realized in metasurface optics. The coding of holograms in particular polarization or wavelength channels is already an anti-counterfeiting feature that is well known [90]. One way to introduce a directional behavior to the metasurface as an additional degree of freedom is to use chiral meta-atoms [91, 92]. Another possibility is the stacking of different planar structures [85, 93, 94]. As long as the stacked meta-atom dimensions are still in the subwavelength range, they can be considered a two-dimensional metasurface.

Note that directional metasurfaces are not necessarily non-reciprocal optical devices. If we treat the forward and backward propagation directions as two modes A and B, and our metasurface as a connector, a non-reciprocal device would transfer light from mode A to mode B but not from mode B to mode A. This behavior can be described by the scattering matrix of the connector. In the non-reciprocal case, the scattering matrix must be asymmetric [88].

3.1 Directional polarization encryption by a layered plasmonic metasurface

In this section, a directional metasurface hologram is presented. The design of the metasurface has two layers of plasmonic meta-atom arrays. Each layer exhibits different functionalities to finally realize asymmetric holographic image encryption. An L-shaped antenna design is used to store the holographic phase information in a linear cross-polarization channel. In the following, this layer is called the holographic layer. The L-shaped layer alone would show symmetric transmission behavior in the sense that the hologram would appear by illuminating the metasurface from the front side and also by illuminating the metasurface from the back side. By adding a second layer of nanoantennas which act as a polarizer, the symmetric behavior can be suppressed (this layer is called the polarizing layer). By stacking the holographic layer with the polarizing layer, one can realize asymmetric transmission properties as illustrated in Figure 3.1. By illuminating the stacked metasurface from the front side with vertically polarized light, a Fourier-hologram shows the initials of our institutes and the word META on the screen in the horizontally polarized output channel. By flipping the sample, illuminating the metasurface from the back side, the hologram disappears in the same polarization state.

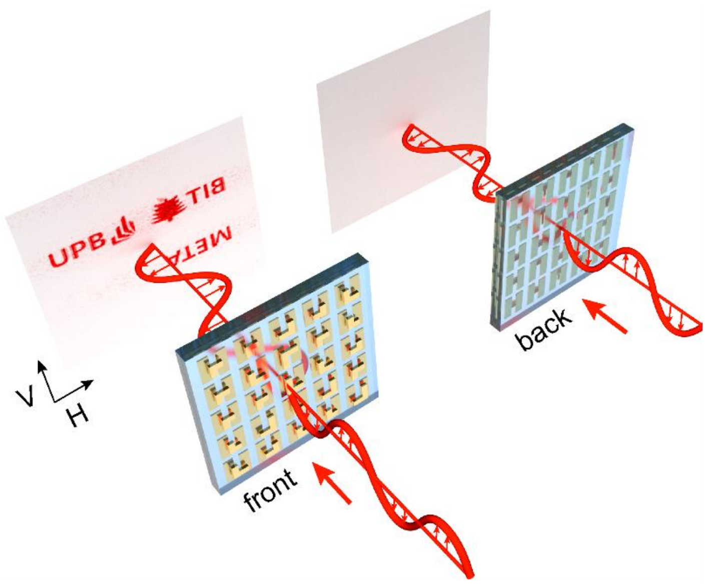

Figure 3.1 Schematic illustration of the directional two-layer polarization-sensitive metasurface-hologram. Left: By illuminating the sample from the front side (L-shaped on top) with V-polarized light, the holographic image is reconstructed in the cross-polarization state (H). Right: By flipping the sample so that the back side is illuminated (plasmonic dimers first), the holographic image is hidden in the cross-polarization state (V to H) [30].

3.1.1 An idealized description of a layered metasurface with directional transmission properties

The directional functionality of stacked metasurfaces can be understood in a simple model based on the Jones formalism. The upper layer is made of plasmonic L-shaped antennas. These antennas can convert linearly polarized light in their co- and cross-polarized state. In general, the transmission matrix t_L^f of an L-shaped antenna illuminated in forward direction consists of nonzero diagonal and off-diagonal elements:

$$t_L^f = \begin{pmatrix} t_{HH}^f & t_{HV}^f \\ t_{VH}^f & t_{VV}^f \end{pmatrix}. \tag{3.1}$$

The superscript denotes the propagation direction (f for forward and b for backward propagation). The off-diagonal matrix elements t_{HV}^f and t_{VH}^f are complex transmission coefficients that describe the cross-polarization conversion of the L-shaped antenna from linear vertically (V) to linear horizontally (H) polarized light and vice versa. The diagonal elements describe the transmission in the co-polarized state horizontal to horizontal and vertical to vertical (t_{HH}^f and t_{VV}^f). If the same L-shaped structure is illuminated in the backward propagation direction, the transmission can be expressed as

$$t_L^b = \begin{pmatrix} t_{HH}^b & t_{HV}^b \\ t_{VH}^b & t_{VV}^b \end{pmatrix} = \begin{pmatrix} t_{HH}^f & -t_{VH}^f \\ -t_{HV}^f & t_{VV}^f \end{pmatrix} \tag{3.2}$$

Compared to the forward direction, the diagonal elements remain unchanged. However, the off-diagonal elements exchange and undergo a sign change [95]. Hence, one can generally not expect asymmetric transmission properties from anisotropic structures as single-layer planar nanoantenna arrays. To introduce a certain symmetry break perpendicular to the metasurface, a second layer consisting of plasmonic dimer antennas is introduced. If this layer is considered to be an ideal linear polarizer that ideally transmits horizontally polarized light and ideally reflects vertically polarized light, one can express the transmission matrix t_{II}^f of the dimer layer (by neglecting any losses) as:

$$t_{II}^f = \begin{pmatrix} 1 & 0 \\ 0 & 0 \end{pmatrix}. \tag{3.3}$$

If only the idealized system is considered and potential Fabry-Perot-effects and near-field couplings are neglected, one can describe the transmission of the layered system by matrix multiplication. In the co-polarization state, the transmission from the incoming H-polarization state $|H\rangle$ to target H-polarization state $\langle H|$, as well as the vertically polarized channel, is investigated and one can find

$$\langle H|\, t_{II} \cdot t_L^f |H\rangle = \begin{pmatrix}1\\0\end{pmatrix}^T \begin{pmatrix}1 & 0\\0 & 0\end{pmatrix} \begin{pmatrix}t_{HH}^f & t_{HV}^f\\ t_{VH}^f & t_{VV}^f\end{pmatrix} \begin{pmatrix}1\\0\end{pmatrix} = t_{HH}^f \tag{3.4}$$

$$\langle V|\, t_{II} \cdot t_L^f |V\rangle = \begin{pmatrix}0\\1\end{pmatrix}^T \begin{pmatrix}1 & 0\\0 & 0\end{pmatrix} \begin{pmatrix}t_{HH}^f & t_{HV}^f\\ t_{VH}^f & t_{VV}^f\end{pmatrix} \begin{pmatrix}0\\1\end{pmatrix} = 0 \tag{3.5}$$

$$\langle H| t_L^b \cdot t_{II} |H\rangle = \begin{pmatrix}1\\0\end{pmatrix}^T \begin{pmatrix}t_{HH}^f & -t_{VH}^f\\ -t_{HV}^f & t_{VV}^f\end{pmatrix} \begin{pmatrix}1 & 0\\0 & 0\end{pmatrix} \begin{pmatrix}1\\0\end{pmatrix} = t_{HH}^f \tag{3.6}$$

$$\langle V| t_L^b \cdot t_{II} |V\rangle = \begin{pmatrix}0\\1\end{pmatrix}^T \begin{pmatrix}t_{HH}^f & -t_{VH}^f\\ -t_{HV}^f & t_{VV}^f\end{pmatrix} \begin{pmatrix}1 & 0\\0 & 0\end{pmatrix} \begin{pmatrix}0\\1\end{pmatrix} = 0 \tag{3.7}$$

This shows that, in the case of the co-polarization transmission, the layered system is independent of the propagation direction. In the case of horizontally polarized light, the transmission depends on the diagonal element t_{HH}^f of the L-shaped antenna's transmission matrix in forward and backward directions. In the case of vertically polarized light, the transmittance is zero.

This behavior changes in the linear cross-polariton channels. In the experiment, one can utilize the cross-polarization transmission from the initial state $|V\rangle$ the target state $\langle H|$ and vice versa. Thus, it holds:

$$\langle H|\, t_{II} \cdot t_L^f |V\rangle = t_{HV}^f \tag{3.8}$$

$$\langle H| t_L^b \cdot t_{II} |V\rangle = 0 \tag{3.9}$$

$$\langle V|\, t_{II} \cdot t_L^f |H\rangle = 0 \tag{3.10}$$

$$\langle V| t_L^b \cdot t_{II} |H\rangle = -t_{HV}^f \tag{3.11}$$

It is apparent that the transmission of the layered system depends on the off-diagonal element of the L-shaped structure. In the forward direction, the transmission for the input polarization state $|V\rangle$ and the output polarization state $\langle H|$ is described by t_{HV}^{f} (Eq. (3.8)). In backward propagation direction with the same polarization state, the transmission is equal to zero (Eq. (3.9)). Further, if the input linear polarization state and the output polarization state are changed to $|H\rangle$ and $|V\rangle$, respectively, the behavior of the sample changes and the transmission is equal to zero in the forward direction and nonzero in the backward direction (Eq. (3.10) and (3.11)). The idealized description illustrates the transmission behavior of such layered L-shaped and dimer configurations. Losses, reflections, spacing, and coupling effects are not considered in this simple picture.

3.1.2 Design of the layered metasurface

To realize a directional metasurface hologram, it is important to control the spatial phase distribution along the metasurface. Therefore, the metasurface is divided into an array of pixels. Each pixel consists of two different nano structures on top of each other, separated by a spacer. The upper structure is a L-shaped antenna made of gold. The width and height of the antenna is 100 nm and 50 nm, while the arm lengths L_x and L_y are varied to modulate the phase of the transmitted light (Figure 3.2a). The lower structure is a dimer pair consisting of two gold antennas with dimensions of 160 nm × 450 nm × 50 nm (width × length × height) separated by a 100 nm gap (Figure 3.2b). A final pixel consists of an L-antenna on top of a dimer pair separated by a SiO_2

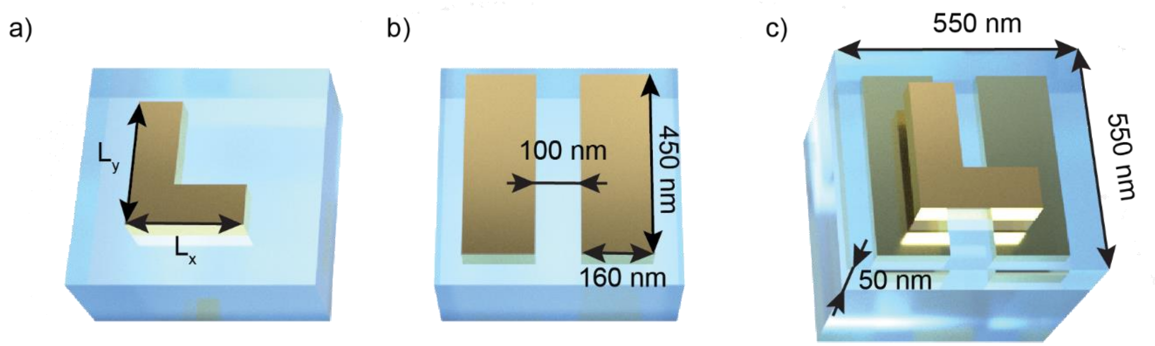

Figure 3.2 Unit cells of the layer metasurface structure for directional holography. Schematic illustrations of the unit-cells of the a) holographic layer and the b) polarizing layer. Each L-shaped antenna is determined by its arm lengths L_x and L_y. Two dipole antennas for the polarizer layer form a pair (dimer). c) In the final design, the polarizer layer is placed on a fused quartz glass substrate. The L-shaped nanoantenna is centered above two dipole antennas, separated by a SiO_2 spacer with a thickness of 50 nm. Each unit cell has a periodicity of 550 nm [30].

layer of 50 nm as illustrated in Figure 3.2c. The free parameters for the mainly phase modulation are therefore the antenna dimensions L_x and L_y. The unit-cell size of each pixel is 550 nm by 550 nm.

3.1.3 Calculated phase and amplitude modulation

To encode a phase-hologram into the L-shaped structure, the phase shift introduced by the L-antenna in dependence on the arm lengths must be known. Therefore, the phase and amplitude modulations are calculated in the transmission channels t^f_{HH}, t^f_{HV}, t^f_{VH}, and t^f_{VV} at the chosen design wavelength of $\lambda = 1150$ nm. The parameter sweeps over the antenna arm length L_x and L_y of the full metasurface pixel stack including the substrate, dimer, spacer, and L-shaped antenna are shown in Figure 3.3. The refractive index of the spacer and the substrate is set to n = 1.4 and for the dielectric function of gold, the values given by Johnson and Christy are taken [67]. As expected from the dimer design, one can find an increased transmission amplitude in the

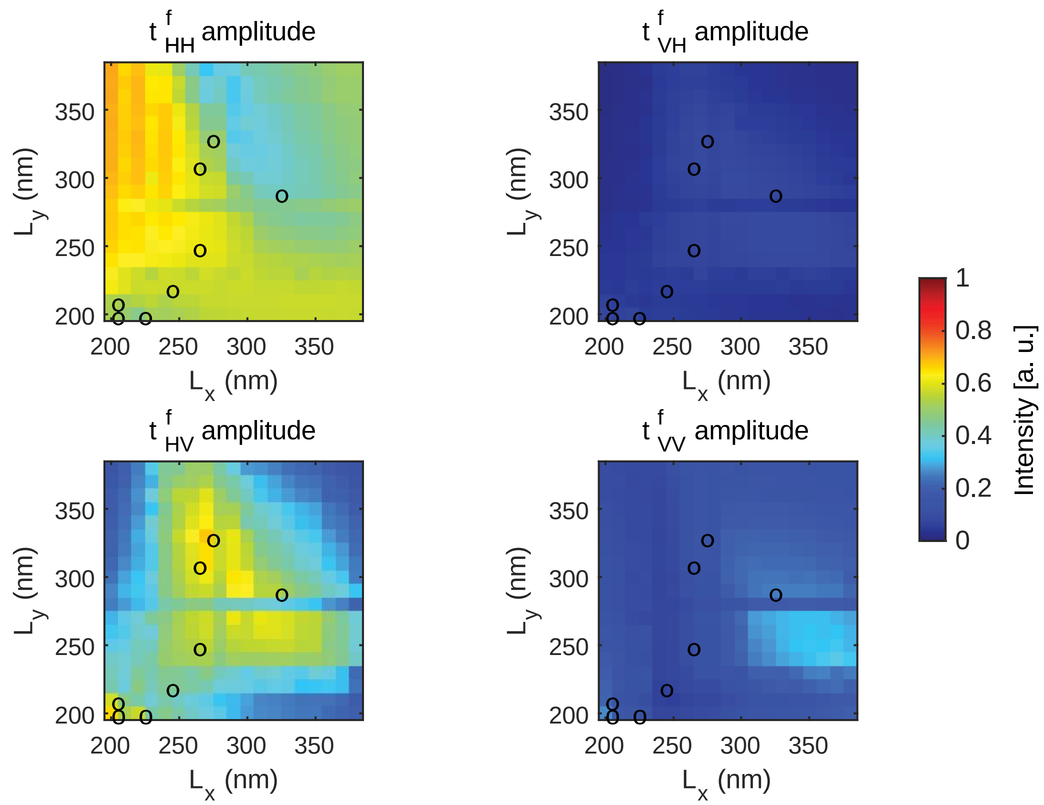

Figure 3.3 Simulated transmission amplitude of the combined double layer system by sweeping the two arm lengths of L_x and L_y, for a spacer thickness of 50 nm. The black circles indicate the selected antenna dimensions for the hologram design.

horizontal output channel $\langle H|$. In the vertical output channel $\langle V|$, the amplitude of the transmission coefficients is suppressed close to zero within the parameter range.

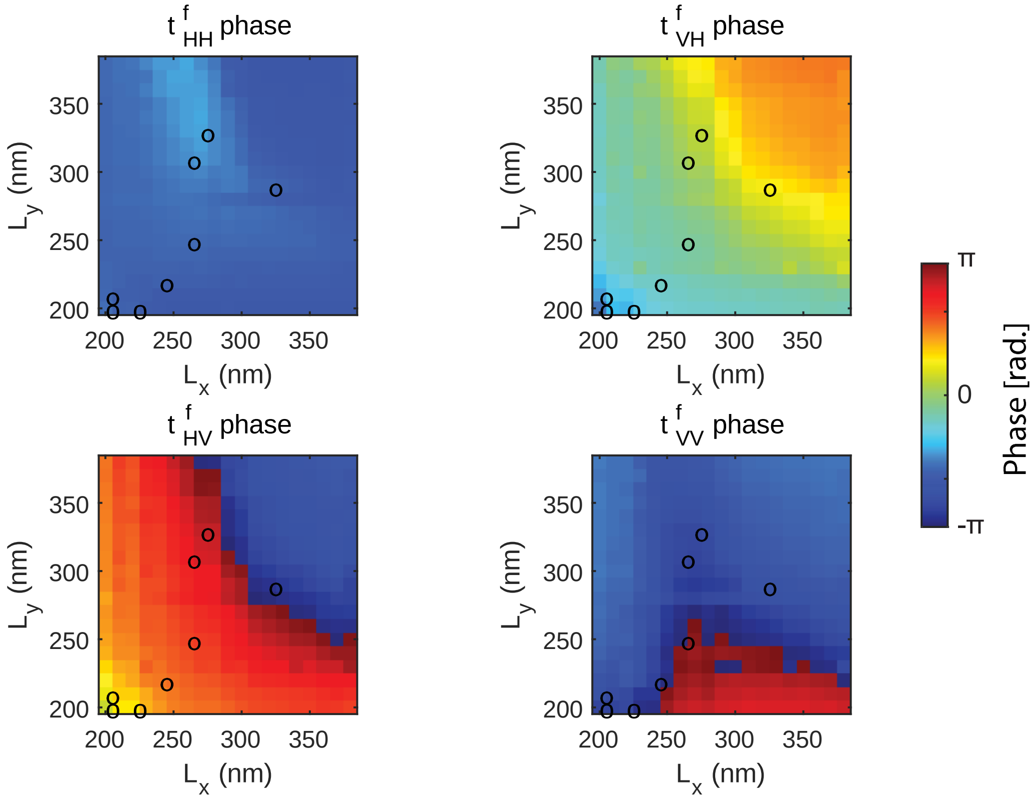

Figure 3.4 Simulated transmission phase of the combined double layer system by sweeping the two arm lengths of L_x and L_y, for a spacer thickness of 50 nm. The black circles indicate the selected antenna dimensions for the hologram design.

The calculated phase modulation is shown in Figure 3.4. In the co-polarization channels t^f_{HH} and t^f_{VV}, the phase is unsensitive over almost the whole parameter range of L_x and L_y. Thus, encoding a phase hologram in these polarization channels is extremely limited by the small phase range which could be introduced by the structure. However, considering the cross-polarization channels t^f_{VH} and t^f_{HV}, the phase range reaches approximately from $-\pi$ to 0 and from 0 to π, respectively. For the phase-hologram design, eight different antenna pairs from the polarization channel t^f_{HV} are selected for the image encryption, ranging from 0 to π, while the amplitude of the selected antennas is preferably constant. The selection is indicated by the black circles in Figure 3.3 and Figure 3.4. Due to the choice of the L-shaped structure, one can achieve the remaining phase range from $-\pi$ to 0 by also considering the mirrored structures of the eight selected antennas, which leads to a phase shift of π. Thus, one ends up with 16 different phase levels covering the full phase range from $-\pi$ to π.

For better demonstration, the transmission coefficients and the corresponding phase values are plotted for the eight selected antennas in Figure 3.5a and b. The phase slope of the transmission

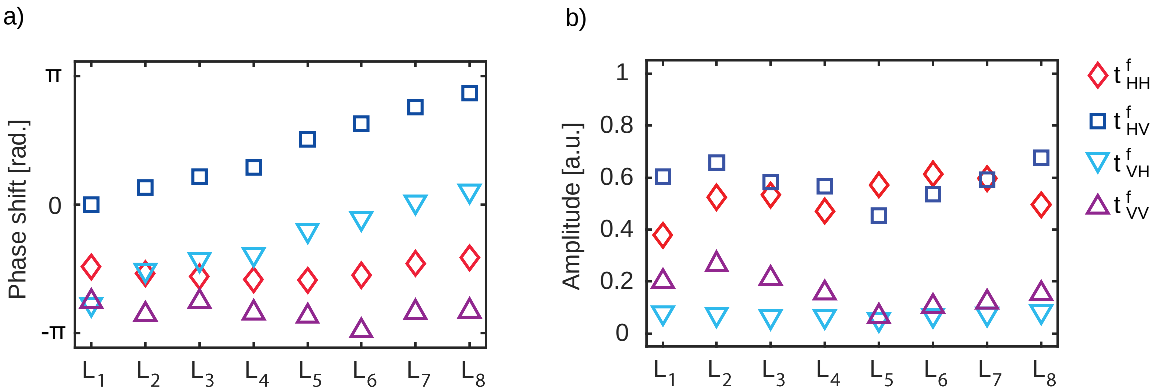

c)

Antenna index	1	2	3	4	5	6	7	8
L_x (nm)	320	200	200	200	240	260	260	270
L_y (nm)	290	200	210	200	220	250	310	330

Figure 3.5 Simulated transmission coefficients of the combined L-dimer unit cell. a) Phase modulation of the co- and cross-polarized transmission coefficients for eight different L-shaped geometries (L1 - L8). The transmission coefficients t^f_{HV} and t^f_{VH} provide a phase range over π, respectively. b) The transmission amplitudes t^f_{HH} and t^f_{HV} of the selected antenna pairs are similar and drop significantly for the opposite polarization states t^f_{VV} and t^f_{VH}. c) Table of the selected antenna dimensions [30].

coefficients t^f_{HV} and t^f_{VH} cover the whole phase range from 0 to π and from $-\pi$ to 0, while the phase modulation in the co-polarization channels t^f_{HH} and t^f_{VV} is relatively constant for the eight selected antenna pairs. The transmitted amplitude is approximately 0.6 and relatively constant in the horizontally polarized output channel $\langle H|$, while the transmission in the case of the vertically polarized output channel $\langle V|$ is significantly smaller. The selected antenna parameters are listed in Figure 3.5c.

3.1.4 The fabricated metasurfaces and their polarization conversion efficiency

The layered metasurface hologram is fabricated based on electron-beam lithography (EBL) and thin-film deposition. After the dimer layer is patterned, 50 nm of gold is deposited and a lift-off is performed according to the process described in section 2.8.1. Subsequently, the 50 nm thick SiO_2 layer is deposited and the holographic L-shaped layer is fabricated on top. The thickness of the L-shaped antennas is 50 nm of gold. Before every depositing of gold, 1 nm of chromium is deposited as an adhesive layer.

The fabricated structure is imaged by an SEM shown in Figure 3.6. To investigate not only the layered metasurface but also the optical properties of the single holographic L-shaped layer and the polarizing dimer layer, all three combinations are fabricated. Note that the L-shaped antennas and the dimer structure are covered with 50 nm SiO_2 (Figure 3.6a and b). Thus, the corners of the covered structure look fuzzy in the SEM image. However, despite the relatively thin spacer compared to the gold film (both 50 nm), the L-shaped structure on top of the SiO_2 seems to be unaffected by the potentially surface roughness of the underlying layer (Figure 3.6c). The L-shaped layer on top of the SiO_2 is placed in the air.

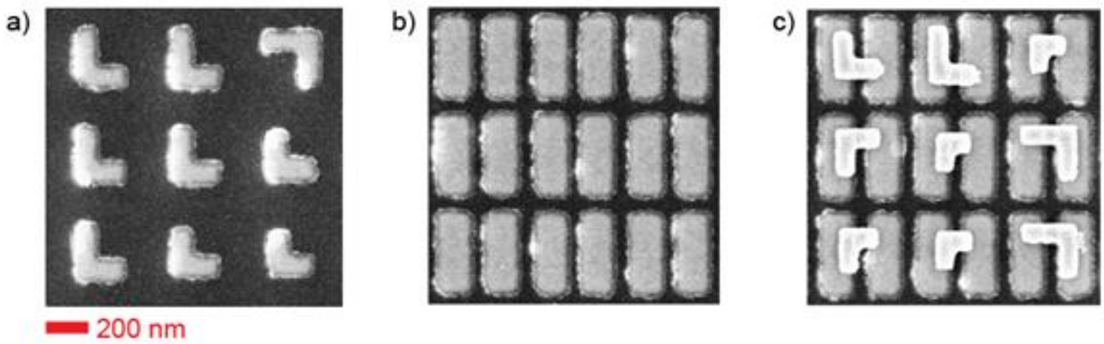

Figure 3.6 SEM image of the fabricated metasurface. a) Single layer L-shaped antennas, b) single layer dimer antennas, and c) double layer dimer and L-shaped antennas separated by 50 nm of SiO_2.

After the fabrication of the samples, the transmittance and the resulting polarization conversion efficiency are measured by Fourier-Transform-Infrared (FTIR) spectroscopy for all three combinations. As shown in Figure 3.7a, the maximum amplitude in the operation channel t_{HV}^{f} and t_{VH}^{b} is at 1270 nm, 120 nm red-shifted from the design wavelength of 1150 nm. This can be due the fabrication process, which tends to produce larger nanoantenna dimensions compared to the initial design. This effect is more pronounced for dense structures like the dimer layer, where the proximity effect becomes more dominant. The layered hologram shows a polarization conversion efficiency up to 6.7 % at 1270 nm for a vertically polarized input and horizontally polarized output beam in the forward direction (t_{HV}^{f}), while the complementary polarization channel's amplitude is suppressed below 0.5 % (t_{VH}^{f}). In the backward direction, the polarization dependency flips as expected. For horizontal input and vertical output polarization (t_{VH}^{b}), the transmittance is significantly higher than for the opposite linear polarization channel (t_{HV}^{b}), which is again suppressed below 0.5 %.

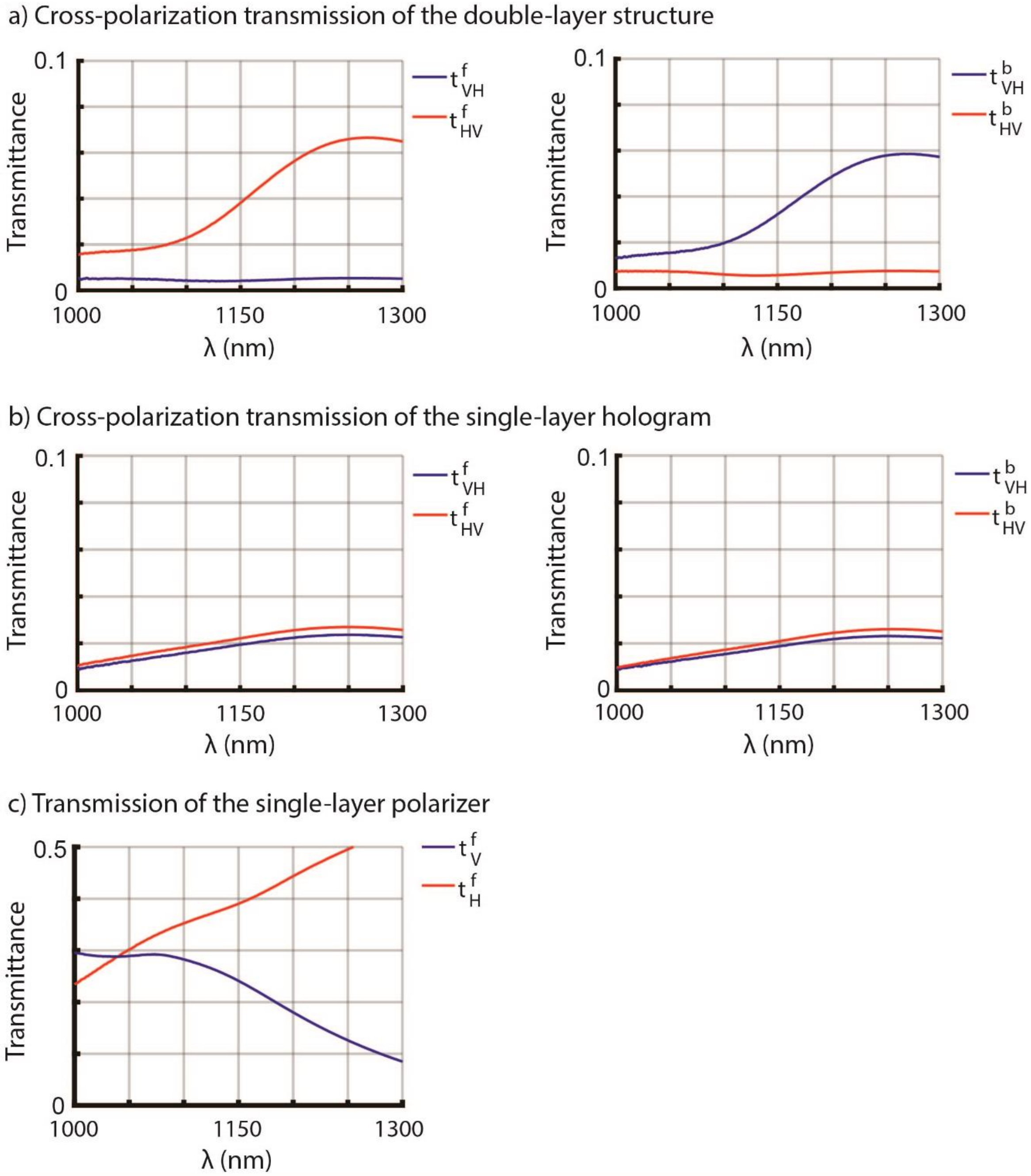

Figure 3.7 Transmittance of the metasurfaces in the for- and backward direction measured by FTIR spectroscopy. a) Measured transmittance of the layered metasurface in the cross-polarization channels, b) transmittance of the single-layer holographic layer, and c) transmittance of the single dimer layer under vertically and horizontally polarized incident light.

For the single-layer hologram, one can find a symmetric behavior as shown in Figure 3.7b. In all four transmission channels t_{VH}^{f}, t_{HV}^{f}, t_{VH}^{b} and t_{HV}^{b} the transmittance is ca. 2 % between 1150 nm and 1300 nm. It is expected that the single-layer results in a symmetric transmittance in the cross-polarization channels, but surprisingly, the conversion efficiency is lower than in the case of the layered system. This indicates how sensitive plasmonic nanostructures are to changes in the environment and that it is crucial to optimize the combined structure in the simulations.

In Figure 3.7c, the transmittance of the dimer layer is plotted for a vertically and a horizontally polarized input beam. Surprisingly, the single-layer polarizer does not resemble a conventional linear polarizer. One would expect from the design that vertically polarized light, parallel to the long axis of the dimer antennas, is reflected. Horizontally polarized light, parallel to the short axis of the dimer antennas should ideally be transmitted. The measured data show that the behavior seems to be the opposite, but a clear trend is not obvious.

However, the spectra of the single-layer underline that it is important to consider the combined structure in the simulation for the parameter optimization. Since the two layers of plasmonic nanoantennas are only separated by 50 nm, strong coupling effects can occur. In this case, the coupling seems to be so strong, that the property of the dimer polarizer completely vanishes by the absence of the L-shaped antennas. This also underlines that the simple description of section 3.1.1 can only be used to explain the dependencies of the polarization channels.

3.1.5 Holographic image reconstruction

To reconstruct the hologram of the layered metasurface, a Ti:Sapphire pumped optical parametric oscillator (OPO) is used as a light source. As illustrated in Figure 3.8a, the linear polarized laser light with a wavelength of 1150 nm is focused on the metasurface. The polarization of the light source can be rotated by a halfwave plate. The transmitted laser light is collected by a MO with 40x magnification and NA = 0.6. Since a Fourier hologram is encoded in the metasurface, the back focal plane of the MO is imaged on a CMOS camera using two lenses. Therefore, the first lens behind the MO is placed at a distance equal to its focal length from the back focal plane. The second lens behind the MO is placed at a distance equal to the sum of both

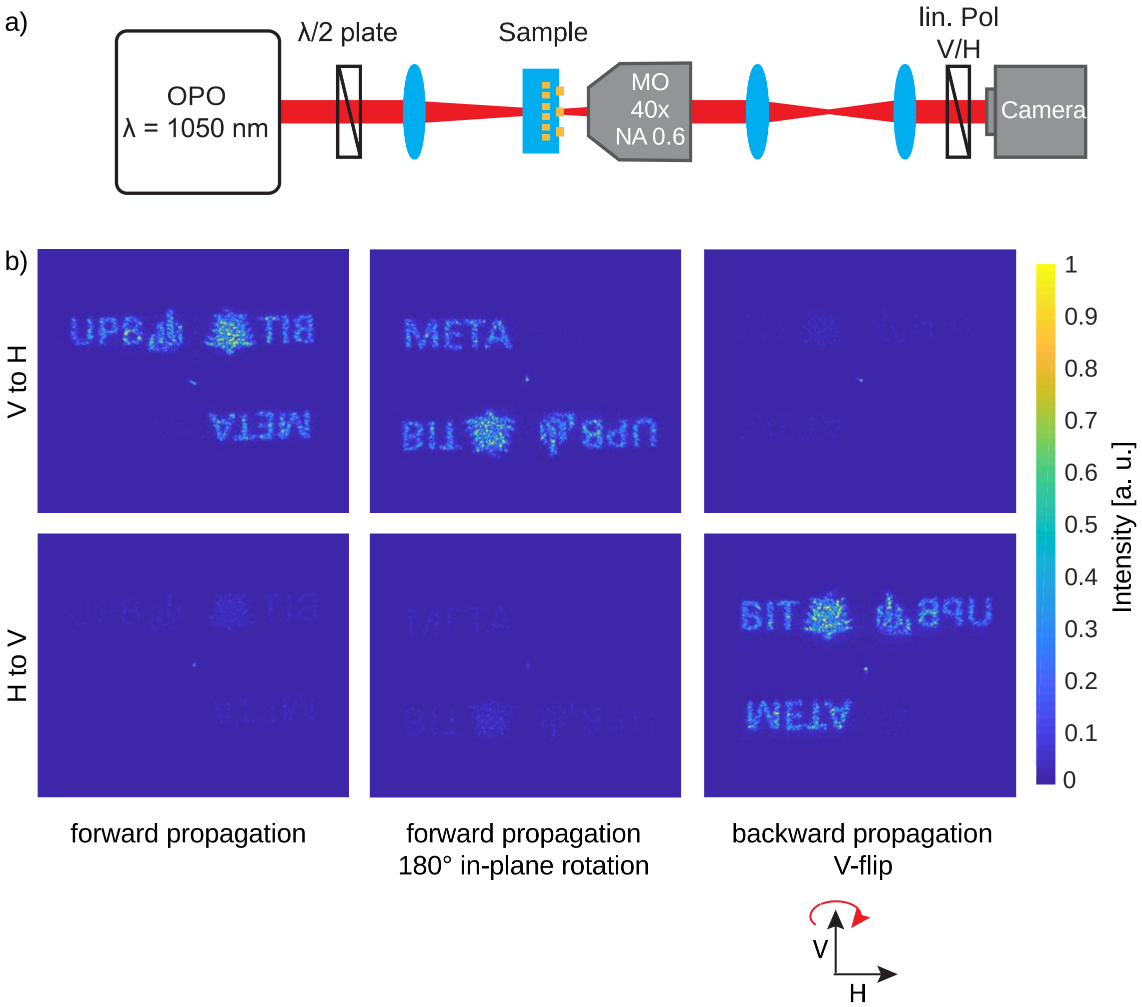

Figure 3.8 Optical setup and holographic images measured for the design wavelength of 1150 nm in different orientations. a) As the light source an OPO is used and tuned to 1150 nm excitation wavelength. The linear polarization state can be rotated by a half-wave plate. The output polarizer is always oriented perpendicular to the input polarization state to image the cross-polarization channel. The light is focussed on the sample and collected with a MO with 40x magnification and NA = 0.6. Using a 4f-setup, the Fourier-hologram is imaged on a CMOS camera. b) Reconstructed holograms for the cross-polarization states from linear vertically polarized light to linear horizontally polarized light (V to H) and vice versa. In the forward propagation direction, the hologram appears in the V to H channel and disappears in the H to V channel. An in-plane rotation of the sample results in an in-plane rotation of the hologram. In backward propagation direction, the hologram disappears in the V to H channel and appears in the H to V channel [30].

focal lengths behind the previous lens and the camera is placed in the focal spot of the second lens. This arrangement is called the 4f-setup since the positions of lenses and cameras are defined by the focal lengths of the lenses. A linear polarizer in front of the camera is used to image the different polarization channels of interest.

The reconstructed holograms are shown in Figure 3.8b. In the measurement for the hologram reconstruction, the orientation of the sample and the corresponding polarization channel is important. In forward propagation direction, the hologram consists of the initials of our institutes and the word 'META' and appears when linear vertically polarized light passes the sample, and the horizontally polarized output is imaged on the camera (V to H). The hologram is visible including a small 0th-order spot in the center of the image, originating from the unideal polarization filtering. An in-plane rotation of 180° of the sample results in an in-plane rotation of the holographic image in the V to H channel, as one would expect. However, if the sample is rotated around the vertical axis, illuminating it from the back side, the holographic image disappears in the V to H channel. On the other hand, considering the case of the horizontally polarized input beam and vertically polarized output, the behavior changes. In forward propagation, the holographic image disappears, while it is visible in the backward propagation direction when the hologram is flipped around the vertical axis. Due to the rotation around the vertical axis, the hologram is mirrored along the vertical axis. For imaging, a time-averaged laser power of 4 mW and an exposure time of 20 ms is used.

To investigate the spectral behavior of the layered hologram, the image reconstruction is measured for the wavelength of 1050 nm and 1250 nm. The reconstructed holograms are shown in Figure 3.9a and b in the same configuration as for the design wavelength at 1150 nm. It is shown that the directional optical properties do not suffer from a change in wavelength of about 100 nm. At this point, wavelengths longer than 1250 nm are not characterized because the sensitivity of the camera strongly decreases. In the case of 1050 nm wavelength, the time-averaged laser power is set to 1 mW with an exposer time of 4 ms. For 1250 nm wavelength, the laser power is increased to 10 mW with an exposure time of 10 s.

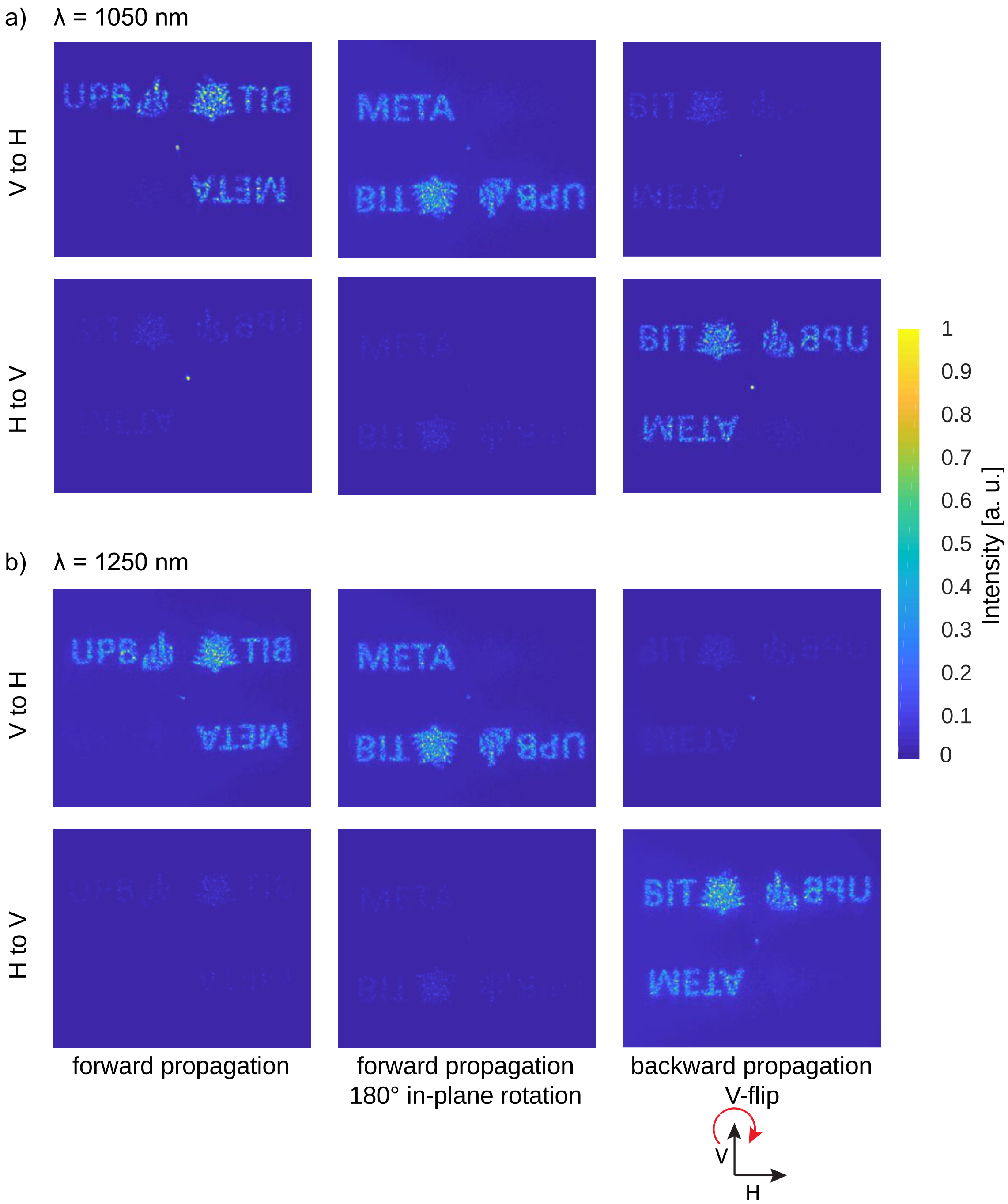

Figure 3.9 Reconstructed holograms for the cross-polarization states from linear vertically polarized light to linear horizontally polarized light (V to H) and vice versa at the wavelength of a) 1050 nm and b) 1250 nm for different sample orientations.

From the FTIR spectra, we found a polarization conversion efficiency of ca. 3.8 % at the design wavelength of 1150 nm. Thus, the hologram reconstruction is investigated without using the output polarizer in front of the camera. In this case, the vertically polarized input beam is focused on the sample and the transmitted light is imaged on the camera without polarization filtering. Figure 3.10a shows that the hologram can still be detected in the forward propagation direction, but with a larger zeroth-order spot in the center of the image, which is caused by the strong vertical component of transmitted light. In backward propagation, the hologram disappears almost entirely. In the co-polarization channels, no holograms are visible in Figure 3.10b. Therefore, the device can also be used without an output polarizer, but with lower image quality.

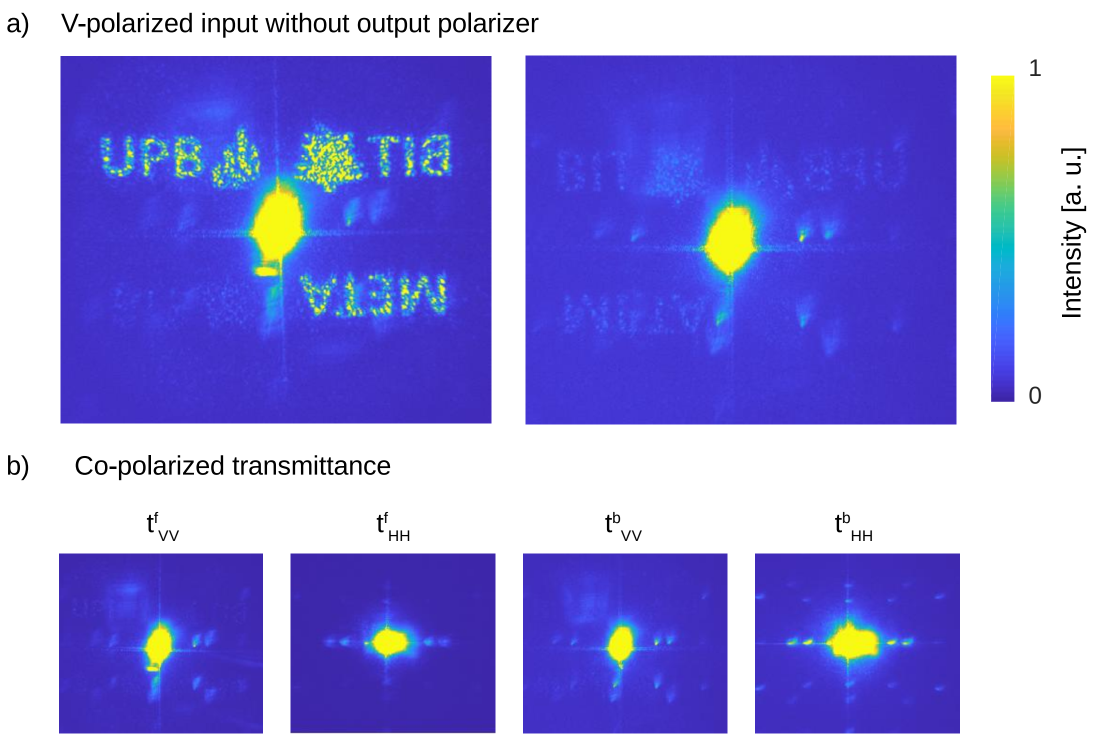

Figure 3.10 Operation results for different polarization settings. a) Measured hologram in for- and backward direction without output polarizer. b) Fourier-imaging in the linear co-polarization channels in the for- and backward direction.

To compare the directional metasurface with its non-directional counterpart, the single-layer holograms without a dimer-layer are characterized. The calculated target image for the forward and backward directions is shown in Figure 3.11a. In comparison, the experimentally reconstructed holograms in the linear cross-polarization channels are shown in Figure 3.11b. As expected, a single layer metasurface hologram without symmetry break perpendicular to the surface does not show asymmetric transmission properties in either case. A flip of the hologram around the vertical axis results in the mirrored holographic image.

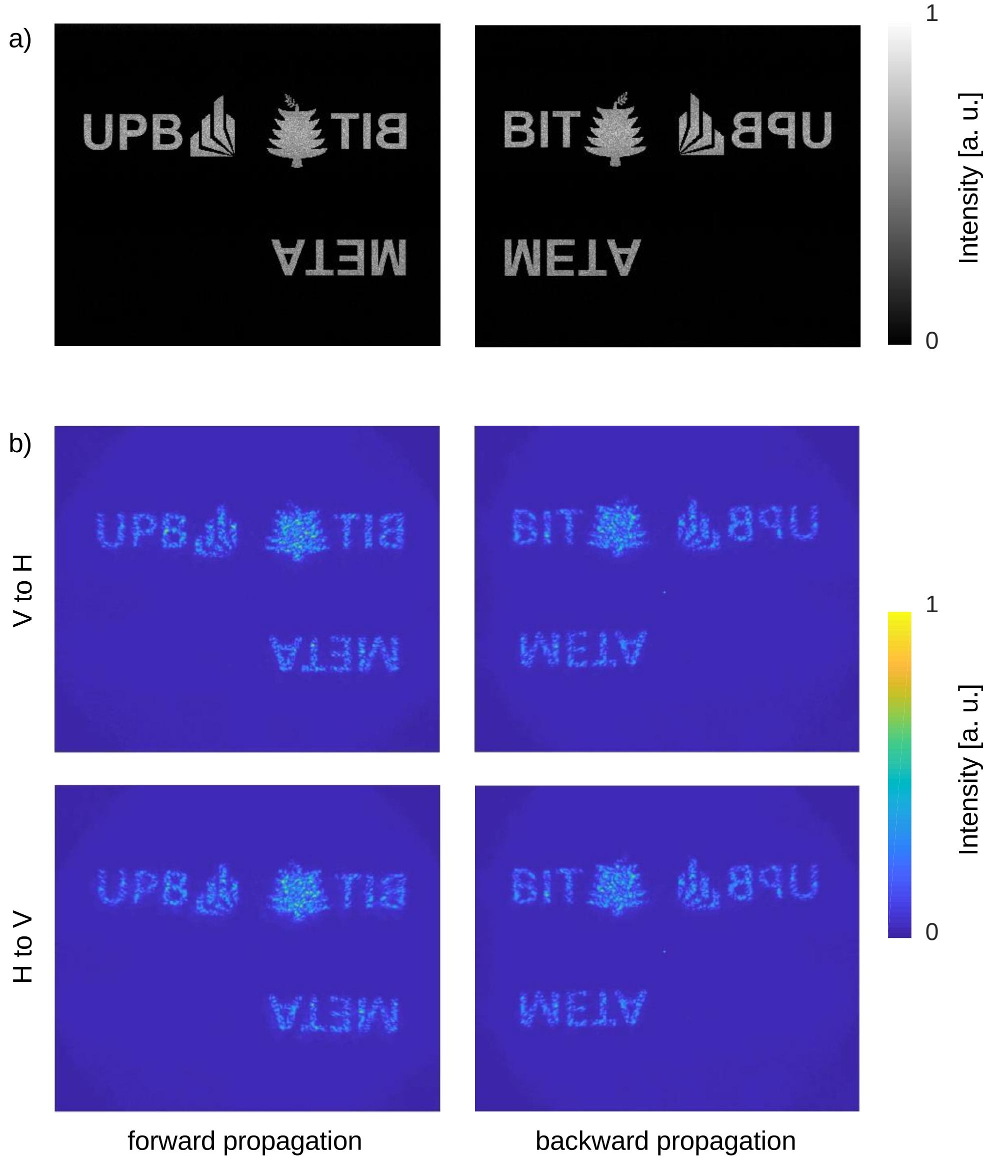

Figure 3.11 Holographic image reconstruction of the single-layer L-shaped antennas. a) Calculated image reconstruction for the forward and backward direction. b) The measured holograms appear in for- and backward propagation direction in both cross-polarization channels, V to H and H to V. Flipping the sample around the vertical axis result in the mirrored image.

3.1.6 Short conclusion of directional holography based on layered metasurfaces

In conclusion, a layered-metasurface system is realized with tailored amplitude and a phase modulation range of 2π in the two different information channels t_{HV}^{f} and t_{VH}^{b}. It is shown that a hologram can be encoded in the layered system where the reconstruction of the hologram is only possible in a certain polarization channel and propagation direction. The calculations and experiments show, that the single-layer properties of the used geometries cannot provide sufficient information about the combined system, since coupling effects caused by the small distance between the layers strongly influence the overall performance of the system. Even if the maximum polarization conversion efficiency is ca. 6.7 % and therefore weak compared to other linear holograms based on plasmonic metasurface holograms [41], the holographic images can be reconstructed with laser powers of several milliwatts and exposure times of milliseconds.

This is an example for a functional metasurface hologram with phase and amplitude control. The metasurface hologram is relatively easy to fabricate based on standard processes and has a thickness of only 150 nm. In principle, the metasurface hologram could be expanded by additional layers to introduce more phase levels while maintaining the directionality.

4 Colored metasurface holograms

Color holography is an interesting research area because colorful holograms are attractive for the human eye and can potentially be used in display applications. The high amount of metasurface designs and material choice provides opportunities for multicolor metasurface-based holograms [96]. Several strategies like angular multiplexing [97], polarization multiplexing [25], or narrow band filtering [23] are used to create multicolored metasurface holograms.

The angular multiplexing method only requires one nanostructure type, for instance, a nanorod. The structure is designed to imprint a geometric phase for three different colors, e.g., red (R), green (G), and blue (B), which have different angles of incidence (Figure 4.1a). Crosstalk can be avoided by choosing a clever observation plane, so that twin images are out of view. Further, because of using only a single nanostructure for three different colors, the antenna density can be relatively high. A disadvantage is the reconstruction setup which must provide RGB light coming from different angles [59, 97, 98].

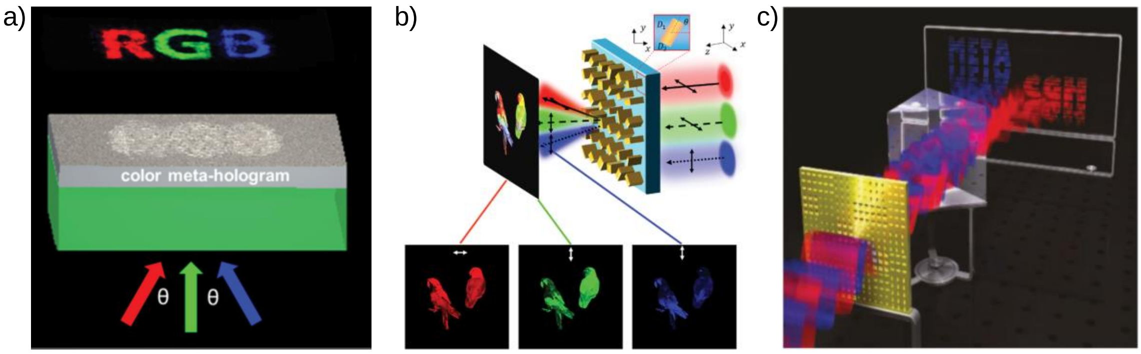

Figure 4.1 a) Illustration of a wavelength multiplexed metasurface hologram. The 'RGB' letters are reconstructed for particular angles of incidence of the red, green, and blue light [59]. b) A polarization multiplexed full color vectorial holographic metasurface. The phase information is coded in the arrangement of TiO_2 rectangular antennas [25]. c) Plasmonic fishnet metasurface consisting of a gold - magnesium oxide – gold multilayer including rectangular and square holes with different dimensions for wavelength-multiplexed amplitude holography [101].

Polarization multiplexing for colored metasurface holograms can be realized by designing nanostructures that work as birefringent elements with certain orientation angles [25]. The colored image which will be encoded is decomposed in the RGB components. The three different images are then encoded in different polarization channels of the metasurface as phase-only holograms, while the information is stored in the rotation of the antennas (Figure 4.1b). The different polarization channels can be linear, circular, co- or cross-polarized, or topologically charged beams [99].

Since nanoantennas can be tuned to respond only to narrow bands of wavelength, one can also design different nano filters for each color. This means, that each color component of the hologram is stored in a distinct nanoantenna design, which only transmits or reflects light in a narrow spectral range. For an RGB hologram, one would need three different nanoantenna types [23, 60]. It has been demonstrated that a combination of narrow filtering and polarization multiplexing can be used to change the color of not only the entire holographic image but also defined parts of it [100].

Apart from phase-holograms, metasurfaces also allow very simple binary amplitude modulation. Walther et al. designed a plasmonic fishnet metasurface consisting of different types of square and rectangular nano holes to encode two amplitude holograms at two different wavelengths in the near-infrared, as illustrated in Figure 4.1c [101]. The geometry used for the amplitude modulation can potentially be extended for complex metasurface designs combining amplitude and phase modulation in different spectral ranges. In this section, I want to demonstrate how amplitude holograms can be combined with phase holograms and enable the encoding of images in different wavelengths and polarization channels. The hologram design is based on the photon sieve principle, similar to the fishnet metasurface, and combined with spatial nano filters.

4.1 Color holography based on photon sieves

Photon sieves are diffractive devices and were originally invented for light focussing in the X-ray regime to overcome high absorption losses in bulky lenses. Photon sieves consist of nanoholes arranged in a metal film similar to Fresnel rings in zone plates [102, 103]. A binary Fresnel zone plate is illustrated in Figure 4.2a. The transparent white rings transmit the light in such a way that it interferes constructively at the focal point of the zone plate. The rings of the zone plates can be replaced by holes and thereby form a photon sieve as illustrated in Figure 4.2b. The holes are arranged circularly at certain radii r_n, where n is an integer and indicates the nth ring, similar to the zone plates. Figure 4.2c shows a photon sieve which focuses the light of a point source at a distance p from the photon sieve to a focal point at distance q. The source and the focal point are on the optical axis. To obtain a first-order spot, the path difference between the light passing through the center hole and a hole at the distance r_n from the center is a multiple of the wavelength λ, given by

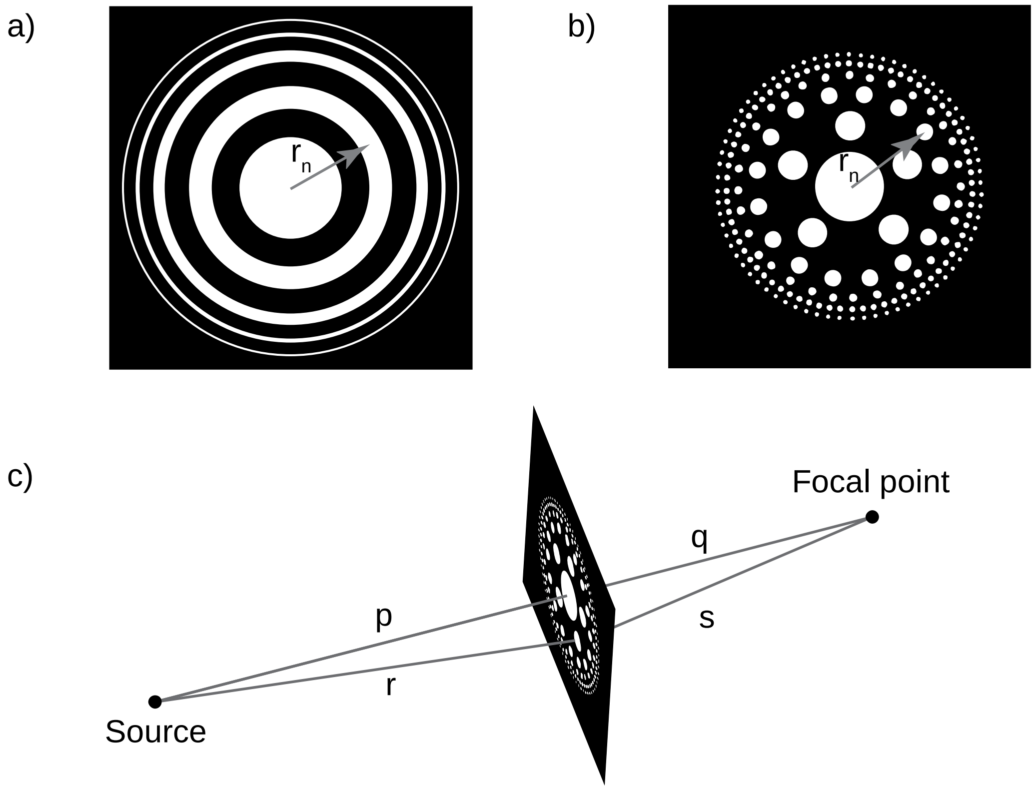

Figure 4.2 a) Illustration of a binary zone plate for light focusing. b) Illustration of a photon sieve consisting of nanoholes for light focusing. The holes of the photon sieve are radially placed at a distance r_n from the center. c) Illustration of point-to-point focusing using a photon sieve.

$$\sqrt{p^2 + r_n^2} + \sqrt{q^2 + r_n^2} = p + q + n \cdot \lambda. \tag{4.1}$$

A useful feature of photon sieves is that the position and distribution of the holes can be utilized to correct aberrations and suppress higher-order diffraction [102]. By using complex arrangements of photon sieves' holes, arbitrary amplitude distributions can be formed. Thanks to computational resources and modern algorithms, the nanohole distributions for desired amplitude modulations can be calculated. First applications in vortex beam generation [104] and holographic image encoding have been demonstrated [46, 105]. So far, holographic applications based on the photon sieve principle are rare, so multiplexing technologies have not been applied to expand the functionality of photon sieve devices yet.

Xu et al. recently presented two quantitatively correlated amplitude holograms based on the photon sieve principle as illustrated in Figure 4.3 [105]. The photon sieve is designed as a binary amplitude hologram where holes are placed in a chromium film to transmit light at certain positions. The correlation can be understood in the sense that the photon sieve hole pattern of sample A forms a subset of the hole pattern of sample B. This means, that sample B is made by

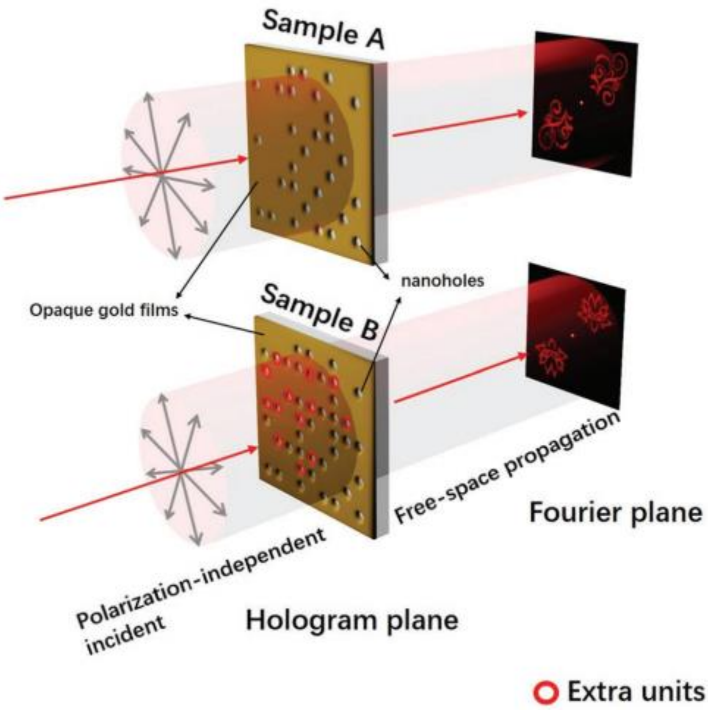

Figure 4.3 Principle of a quantitatively correlated amplitude hologram based on photon sieve design by Xu et al. By adding extra holes to sample A, one can form sample B, so that A forms a subset of B. It is demonstrated that one can form two completely different holographic images in the Fourier plane [105].

adding more holes to the pattern of sample A, resulting in a completely different holographic image. Despite the amplitude correlations, the photon sieve holograms are two steady devices, and the two different images can only be reconstructed if the sample is changed.

To make the photon sieve concept more flexible and enable optically switchable holograms, the nanoholes are replaced by an aperiodic arrangement of square and rectangular apertures to create a binary amplitude hologram. By filling the apertures with silicon nanofins which act as spectral nano filters, a wavelength selectivity is introduced. In addition, the rectangular aperture shape is utilized to encode a third independent phase-only hologram based on the Pancharatnam-Berry phase. Thus, three information channels can be read out depending on the reading beams' wavelength and polarization. Parts of this work have been published in [31].

4.1.1 The basic scheme of a photon sieve for bi-color holography

As building blocks for a wavelength selective photon sieve combined with a phase-only hologram, three major units cells are used: rectangular apertures, square apertures, and the gold film. The apertures are filled with silicon (Si) fins with the same lateral cross-section and designed as narrow bandpass filters. The structures are illustrated in Table 4.1. The square structure and the rectangular structure are designed to transmit light at 575 nm in a circular co-polarization

Structure	Wavelength (nm)	Amplitude-only hologram	Phase-only hologram
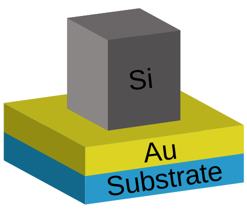	575	co-polarization (A)	-
	670	co-polarization (B)	-
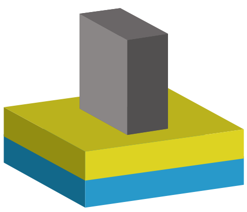	575	co-polarization (A)	-
	670	-	cross-polarization (C)

Encoded holographic images: (A) musical notes, (B) bass clefs, (C) treble clef

Table 4.1 Illustration of the nano filters geometry, the operation wavelengths, and the corresponding hologram type. The combination of square and rectangular structures can reconstruct the amplitude-only hologram A at 575 nm in the co-polarization channel. At 670 nm, the square structure reconstructs the hologram B in the co-polarization, while the rectangular structure reconstructs hologram C in the cross-polarization channel.

channel. An amplitude-only hologram (A) showing musical notes is encoded in the spatial arrangement of the square and rectangular Si blocks in a gold film. Additionally, the square structure is designed to transmit light at a second wavelength of 670 nm. At this wavelength, a second amplitude-only hologram (B) consisting of bass clefs is encoded in the arrangement of the square structures only. To encode a third phase-only hologram (C) consisting of a treble clef, the rectangular structure is utilized and the hologram is encoded based on the Pancharatnam-Berry phase. Hence, the proposed design can carry three different holographic images which can be separately reconstructed depending on the wavelength and polarization channel of the transmitted light.

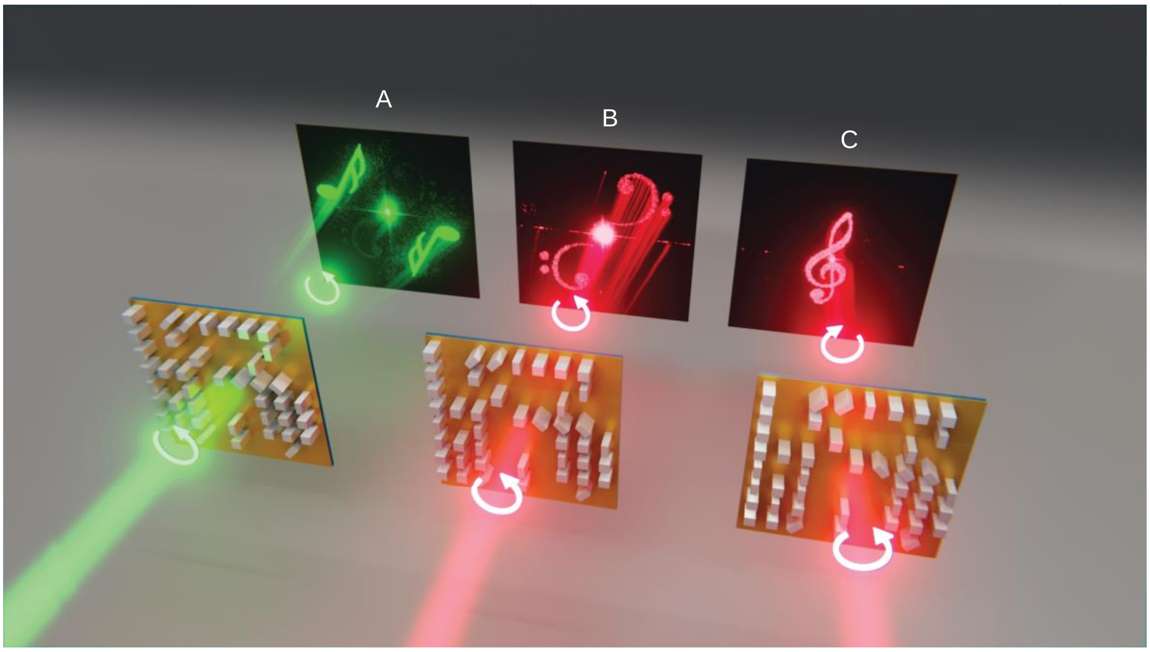

Figure 4.4 Illustration of the modified photon sieve metasurface. The metasurface hologram is designed based on an aperiodic arrangement of rectangular and square shaped apertures filled with Si nanoantennas. By tuning the transmittance of the individual nanoantennas, a dual-amplitude hologram is realized (A and B). By further utilizing an anisotropic shape, a third phase-only hologram is encoded based on the Pancharatnam-Berry phase (C). The holograms can be reconstructed depending on the light's wavelength and polarization channel as illustrated [31].

The metasurface hologram scheme is illustrated in Figure 4.4. In the circular co-polarization channel, from right-handed polarization to right-handed polarization (RCP to RCP), the amplitude holograms A and B are reconstructed. Illuminating the sample with green light reconstructs the musical notes while illuminating the hologram with red light reconstructs the bass clefs. By changing the output polarization from right-handed polarization state to left-handed polarization state (RCP to LCP), the phase-only hologram is reconstructed.

4.1.2 Correlated amplitude holograms

Generally, the transitivity and reflectivity of local unit cells of a metasurface can be designed for different amplitude levels. However, for the photon sieve principle, binary amplitude modulation is a superior design approach. If the photon sieve is designed based on a 2D $n \times m$ array, the different pixels can be considered as light transmitters or light blockers. Ideally, this functions like a digital coding of the metasurface, where each pixel can either have a transmittance $t_{n,m} = 1$ or $t_{n,m} = 0$: 1 meaning the pixel transmits light, 0 meaning the pixel blocks light.

The level of the quantitative correlation between two amplitude profiles is illustrated in Figure 4.5. On the left side, the yellow pixels of the metasurface schemes represent the nontransparent gold film (0), while the green pixels represent the nano hole pattern of a hologram A and the blue pixels represent a nano hole pattern of another hologram B (1). Both hole patterns can be considered as sets A and B, as illustrated on the right side. If the green and blue pixels do not overlap as depicted in Figure 4.5a, set A does not share pixel positions with set B. There is no correlation between A and B. If the green and blue pixels partially overlap as illustrated in Figure

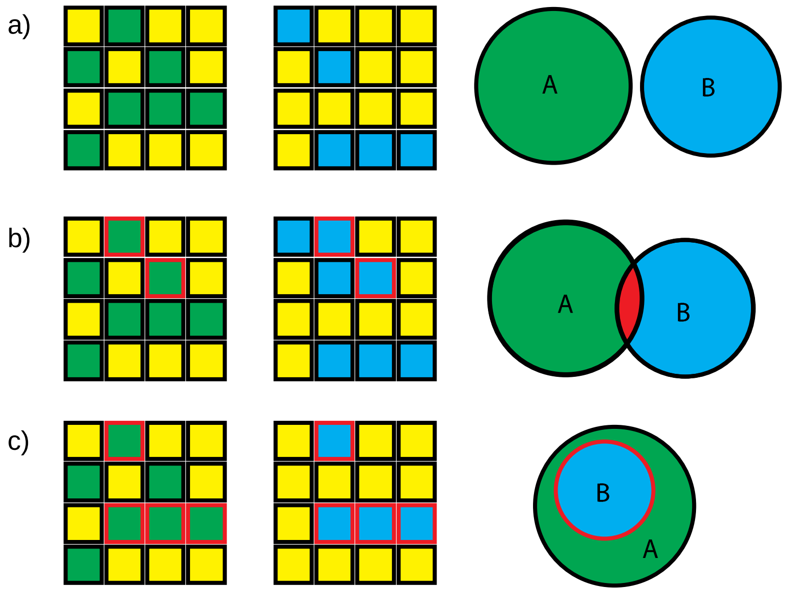

Figure 4.5 Schematic illustration of a photon sieve hologram correlation. The left side schematically illustrates metasurfaces consisting of 4 by 4 pixels. The yellow pixels represent the gold film, while the green pixels correspond to set A (hologram A) and the blue pixels correspond to set B (hologram B) of holes. a) The green and blue pixels of the two illustrated metasurfaces have no overlap and form two separated sets A and B. b) The green and blue pixels have a spatial overlap, indicated in red, so that the sets A and B have an overlap and share some pixels in the hole pattern. c) The blue pixels form a complete subset of the green pixels, so that B ⊆ A. Thus, all blue pixels are included in the green pattern.

4.5b, an intersection of set A and set B is generated so that $\mathrm{A} \cap \mathrm{B} \neq \emptyset$, $\mathrm{A} \cup \mathrm{B} \neq \{\mathrm{A}, \mathrm{B}\}$. The intersection of the pixels and the sets is marked in red. A strict subset $\mathrm{B} \subseteq \mathrm{A}$ is generated if the blue pixel pattern completely overlaps with a part of the green pixel pattern as depicted in Figure 4.5c.

If one finds an amplitude correlation $\mathrm{B} \subseteq \mathrm{A}$, the pixels of A and B can be considered as two bits of information. Thus, the metasurface design can be described by the states (0,0), (1,0), (0,1) and (1,1). In the physical system, these two bits can be realized by using different wavelengths, polarizations, spatial overlapping as information channels. In the case of the dual-amplitude hologram, the binary transmittance $(t_{n,m}(\lambda_1 = 575\,nm), t_{n,m}(\lambda_2 = 670\,nm))$ is utilized to encode the two different holograms A and B.

Figure 4.6 depicts a method to generate two correlated binary amplitude holograms that end up in the relation $\mathrm{B} \subseteq \mathrm{A}$. First, two independent amplitude holograms, original A and original B, are generated based on a modified Gerchberg-Saxton algorithm [105]. Thus, both holograms consist

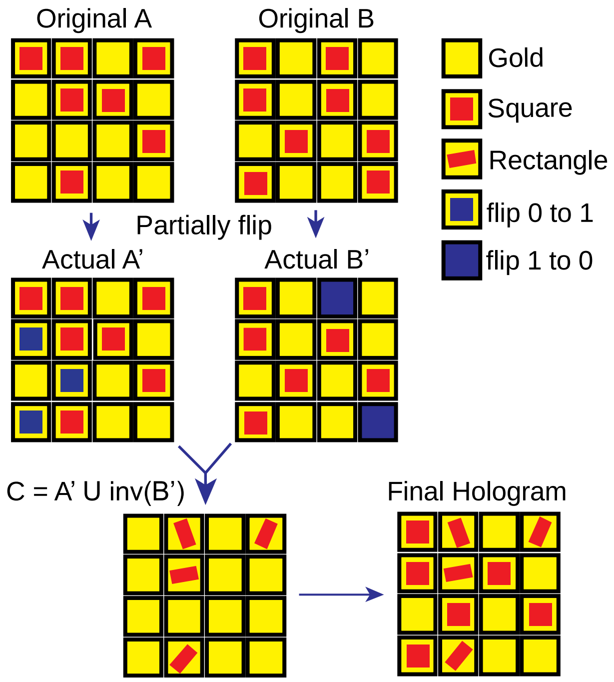

Figure 4.6 Schematic diagram of the holographic algorithm. First, the two holograms original A and original B are calculated independently. Second, transparent pixels are added to the hologram original A randomly, while nontransparent pixels are added to original B randomly, to form the holograms actual A' and actual B' under the condition that the change in the hologram is neglectably small. The wavelength multiplexing is achieved by replacing all squares in A' which are not included in B' with rectangles. An additional arbitrary phase-only hologram can be encoded in the cross-polarization channel by rotation of the rectangular structures [31].

of an individual arrangement of transmitting and blocking pixels. The transmitting pixels are visualized by the red squares and the nontransparent pixels are colored in yellow. Moreover, random pixel flips are performed to both holograms by partially flipping transparent pixels to nontransparent pixels (binary flip from 0 to 1) and vice versa, resulting in the holograms actual A' and actual B'. To ensure a correlation of the two holograms A and B, transparent pixels are added to A and nontransparent pixels are added to B, randomly. Due to the relatively robust nature of holograms against extra phase and amplitude noise, the image quality of the reconstructed hologram actual A' and actual B' should approximate the image quality of original A and original B. While iteratively flipping pixels under comparison of the image qualities between the original and the actual holograms, actual B' can form a subset of actual A'. If condition B' ⊆ A' is achieved, both holograms are compared bitwise. A pattern C is generated and filled with the rectangular structures under the conditions that all antennas which are included in A' but not in B', are replaced by a rectangular structure (C = A' ∪ inv(B')). The final step is to unite C with actual B', which results in the wavelength selective final hologram.

If the final hologram is illuminated with light of $\lambda_1 = 575\ \mathrm{nm}$, both structures transmit the light, and the hologram actual A' is reconstructed. In case of illumination with $\lambda_2 = 670\ \mathrm{nm}$, only the squares transmit the light and actual B' is reconstructed. To add the phase-only hologram to the scheme, the calculated phase-hologram must be translated to the corresponding antenna rotation of the rectangular structures. Thus, the third hologram can be simply reconstructed at $\lambda_2 = 670\ \mathrm{nm}$ by switching from the circular co- to the circular cross-polarization state.

4.1.3 The photon sieve antenna design

To design the antenna dimensions for the square and rectangular shapes, a parameter sweep over the antenna length L and width W is performed. The unit cell of a transparent pixel is illustrated in Figure 4.7a. The unit cell size is set to 300 nm × 300 nm, the silicon height is set to 300 nm, and the gold thickness is set to 40 nm. For the refractive index of amorphous silicon, measured values based on ellipsometry are chosen [31]. As optical constants for gold, the values by Johnsen and Christy are taken [67]. The substrate has a constant refractive index n=1.4 in the simulation. As parameter space for the antenna width W and length L, L ∈ [50 nm, 220 nm] and W ∈ [50 nm, 220 nm] is selected. The parameter space is based on the fabrication experience for those kinds of structures. For this system, approximately 50 nm × 50 nm are the smallest cross-sections that can be fabricated repeatably with sufficient shape quality for these kinds of antennas. The upper limit of 220 nm × 220 nm is primarily limited by the photoresist, which underlies the Proximity effect during the EBL pattern, as well as the lift-off process, which can become difficult for dense structures [106].

Figure 4.7b shows the resulting calculated transmittance T_{co} and T_{cross} for the circularly co- and cross-polarized state depending on the lateral antenna dimensions L and W. As co-polarization state, RCP to RCP is chosen, while the cross-polarization state is RCP to LCP. The parameter sweep

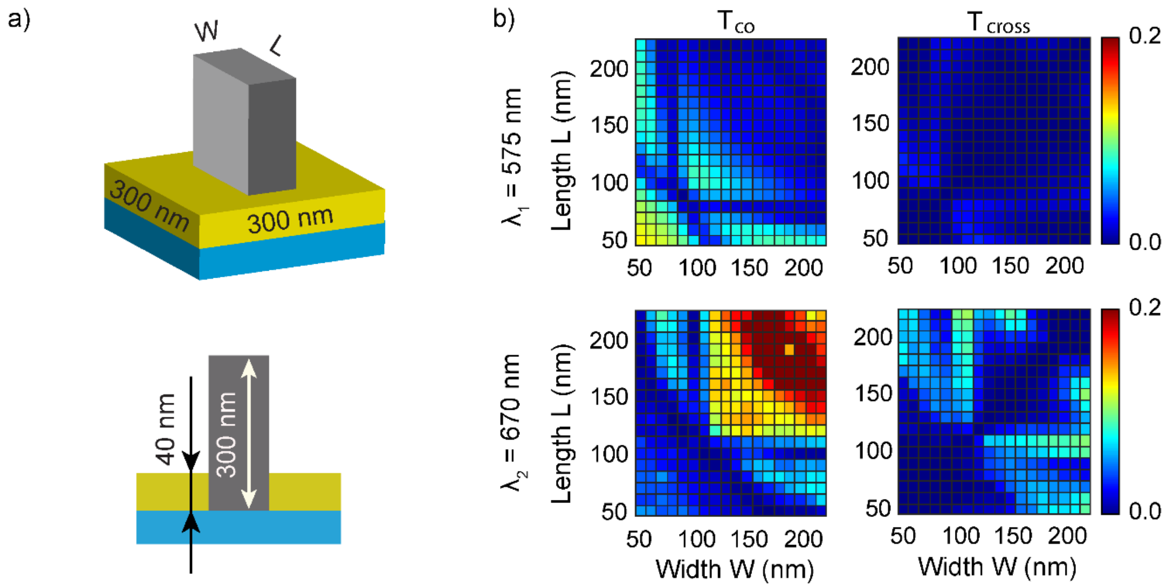

Figure 4.7 Simulated and measured transmission spectra. a) Selected antenna dimensions for the structure depicted in 3D and 2D cross-section. b) parameter sweep over the lateral antenna dimension for a set height of 300 nm for the silicon fins. The transmittance is calculated for the co- and cross-polarization channels at the design wavelengths $\lambda_1 = 575\ nm$ *and* $\lambda_2 = 670\ nm$ *[31].*

is calculated for the incidental design wavelengths $\lambda_1 = 575$ nm and $\lambda_2 = 670$ nm. Due to the geometry of the antennas, the transmittances are mirror-symmetric along the diagonal from the lower-left corner to the upper right corner. Further, the transmittances reach from 0 to 0.2 in the parameter space.

From the parameter sweep, a cross-section of 100 nm × 200 nm for the rectangular structure and a cross-section of 150 nm × 150 nm for the square structure is selected to achieve an equal transmittance of both structures at 575 nm and high contrast of the transmittances between both structures at 670 nm. The calculated spectral transmittance for a wavelength range from 500 nm to 700 nm for both the square and the rectangular structure is plotted in Figure 4.8a. In the circularly co-polarized channel, the transmittance of the rectangular structure (Rec T_{co}) is equal to the transmittance of the square structure (Squ T_{co}) at the design wavelength of 575 nm (the red and green solid lines cross). The transmittance is equal to 0.023. At the second design wavelength of 670 nm, the transmittance of the square antenna is equal to 0.124 and therefore significantly higher than the transmittance of the rectangular structure, which is equal to 0.003.

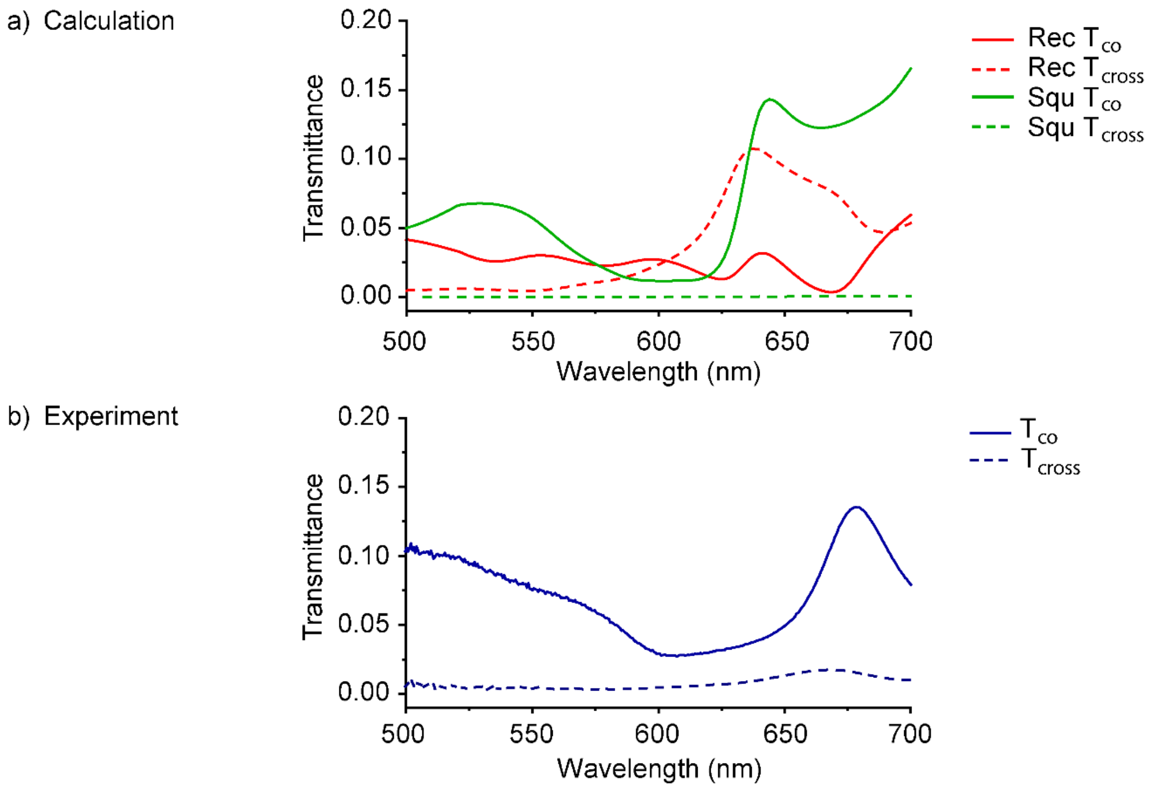

Figure 4.8 a) Calculated transmittance for the rectangular antenna in the circular co and cross-polarization channel (red solid and dashed lines), and the square antenna (green solid and dashed lines). b) Measured transmittance of the fabricated metasurface hologram in the circular co and cross-polarization channel (blue solid and dashed lines).

The large transmittance contrast is necessary to reconstruct only the amplitude profile of the square structure at 670 nm. This contrast is the basis for being able to generate the subset $\mathrm{B} \subseteq \mathrm{A}$ for the amplitude holograms.

In the circularly cross-polarized polarized channel the square antenna transmittance (Squ T_{cross}) is equal to zero. This is expected because of the lateral isotropy of the structure. However, the rectangular structure can convert light in the circularly cross-polarized channel. The calculated transmittance (Rec T_{cross}) of a pixel reaches a maximum of 0.108 at 638 nm.

The transmittance of the photon sieve hologram is measured using a supercontinuum laser as the light source and a spectrometer. The incident light is circularly polarized (RCP) by using a linear polarizer followed by a quarter-wave plate and focused on the photon sieve hologram using a lens with a focal length of 500 mm. The transmitted light is collected with a microscope objective (20x magnification, NA = 0.7) and passes a quarter-wave plate followed by a linear polarizer to detect either the co- or cross-polarization channel (RCP to RCP/RCP to LCP). An aperture is used as a spatial filter to ensure that only light passing through the metasurface is measured (as described in section 2.9). The spectrum is measured with a spectrometer. As reference signal, the transmittance of the substrate without gold film is used.

The measured transmittance of the fabricated photon sieve hologram is shown in Figure 4.8b. Note that the fabricated sample consists of 1200 by 1200 pixels, where 47.91% of the pixels are filled with gold, 31.24% are filled with square-shaped structures, and 20.85% are filled with rectangular structures. Compared to the calculated transmittance with periodic boundary conditions where each pixel is transparent, the experimentally measured transmittance in the co-polarization channel is relatively high. At the design wavelength of 575 nm, the transmittance is 0.061, which is approximately five times higher than the calculated transmittance (0.521 × 0.023 = 0.012) for the rectangular and square structure, considering the filling ratio of 52.09%. The second design wavelength seems to be shifted by 8 nm to 678 nm in the transmission spectrum. At the local maximum, the transmittance is equal to 0.135, which is approximately three times higher than the calculated transmittance (0.312 × 0.135 = 0.042) if one considers the filling ratio of 31.24% with square structures.

In the cross-polarization channel, the experimentally measured cross-polarization conversion reaches its maximum of 0.018 at 668 nm. When considering the filling ratio of the rectangular structures, the theoretically calculated maximum is 0.107 × 0.209 = 0.022 at a wavelength of 638 nm. Thus, the magnitude of the transmittance is in good agreement with the calculation. However, the position of the transmittance maximum of the experiment is 30 nm red-shifted in the spectrum compared to the simulation. Such shifts can be caused by fabrication tolerances.

The measured transmittance and the calculated transmittance show similarities, but a statement about the functionality of the metasurface hologram can only be made by reconstructing the encoded images. Note that the measurement uncertainty of the measured transmittance might be high because of the elaborate spatial filtering in a self-made transmission setup ($\Delta\lambda = \pm 5\ \mathrm{nm}, \Delta\mathrm{T} = \pm 0.010$). Furthermore, the comparison between simulation and experiment is a rough estimation, because the arrangement of the nanostructures is different in both cases.

4.1.4 Fabrication of the photon sieve hologram

The fabricated photon sieve hologram is shown in the SEM image in Figure 4.9a at a 45° viewing angle. The silicon (Si) antennas are set into the apertures in the gold (Au) film in an aperiodic arrangement. To fabricate the sample, we use a standard process based on electron-beam lithography as illustrated in Figure 4.9b, which is described in detail in section 2.8.1. A 50 nm thick

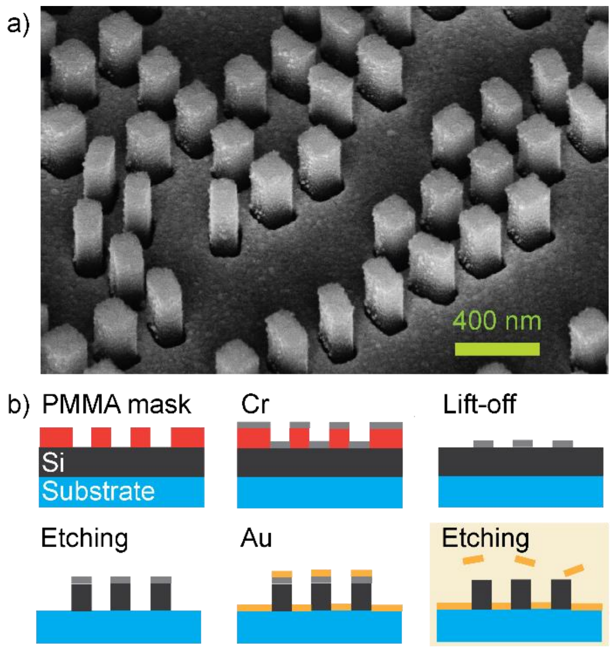

Figure 4.9 a) SEM image of the fabricated sample at 45° viewing angle. b) Depicted fabrication steps. A 50 nm Cr hard mask is fabricated based on a standard EBL process, Cr deposition, and a lift-off process. The 300 nm thick Si antennas are etched by an ICP-RIE process. The 40 nm Au film is deposited and the sample is baked at 270°C for 3 hours. The Au on top of the Si structures is removed by wet etching [31].

chromium (Cr) layer is deposited on the patterned PMMA. After a lift-off process in hot acetone (75 °C), the etching hard mask remains on the 300 nm thick Si layer. The Si nanostructures are etched using an inductively coupled reactive ion etching (ICP-RIE) process (the detailed process parameters are listed in section 2.8.2). After etching, a 40 nm Au layer is deposited using an electron-beam evaporator. After the deposition, the sample is baked at 270 °C for 3 hours to anneal the Au cups on top of the nanostructures, so that the Cr between the Au cups and the Si antennas is accessible from the side walls for a Cr etching solution. The chromium etching solution (TechniEtch Cr01) is used to etch the 50 nm thick sacrificial Cr layer to remove the metals on top of the Si antennas. Thus, the Au cups sitting on top of the Cr layer detach from the Si antennas. Note that the sample is placed upside-down into the etching solution so that the Au particles do not fall onto the metasurface or stick to the Si antennas. The wet etching process takes 3 hours, while it is assisted by sonication at 80 kHz every hour for 10 min.

4.1.5 Reconstruction of the photon sieve holograms

To reconstruct the three different encoded Fourier holograms, a 4f-setup is used as illustrated in Figure 4.10a. A supercontinuum laser combined with a monochromator is used as a tunable light source. The wavelength range covers the visible spectrum and the bandwidth of the monochromator is set to 5 nm. The laser light is converted into the circularly cross-polarized state by using a linear polarizer followed by a 45° rotated quarter-wave plate. It is focused on the metasurface hologram by a lens with a 500 nm focal length. The transmitted light is collected by an MO with 20× magnification and numerical aperture NA = 0.7. The back-focal plane of the MO is projected on a monochrome camera by using two lenses with a focal length of 100 mm in the 4f-arrangement. A second polarizer unit in reverse order can be used to filter out the circularly co- or cross-polarized channel.

The calculated image reconstruction of the holograms at the design wavelengths is illustrated in Figure 4.10b. The holograms are reconstructed under the consideration of the simulated transmittances of both aperture types (Figure 4.8a). At 575 nm, the off-axis placed musical notes are expected in the circular co-polarization channel. The sub-image of the bass clefs is barely visible. At 670 nm, the bass clefs are expected. The musical notes are strongly suppressed due to the theoretically expected transmittance of 0.003 of the rectangular nanoapertures. Changing the polarization to the cross-polarization channel, the phase-only hologram is reconstructed. The treble clef is expected at 670 nm, with a weak background signal.

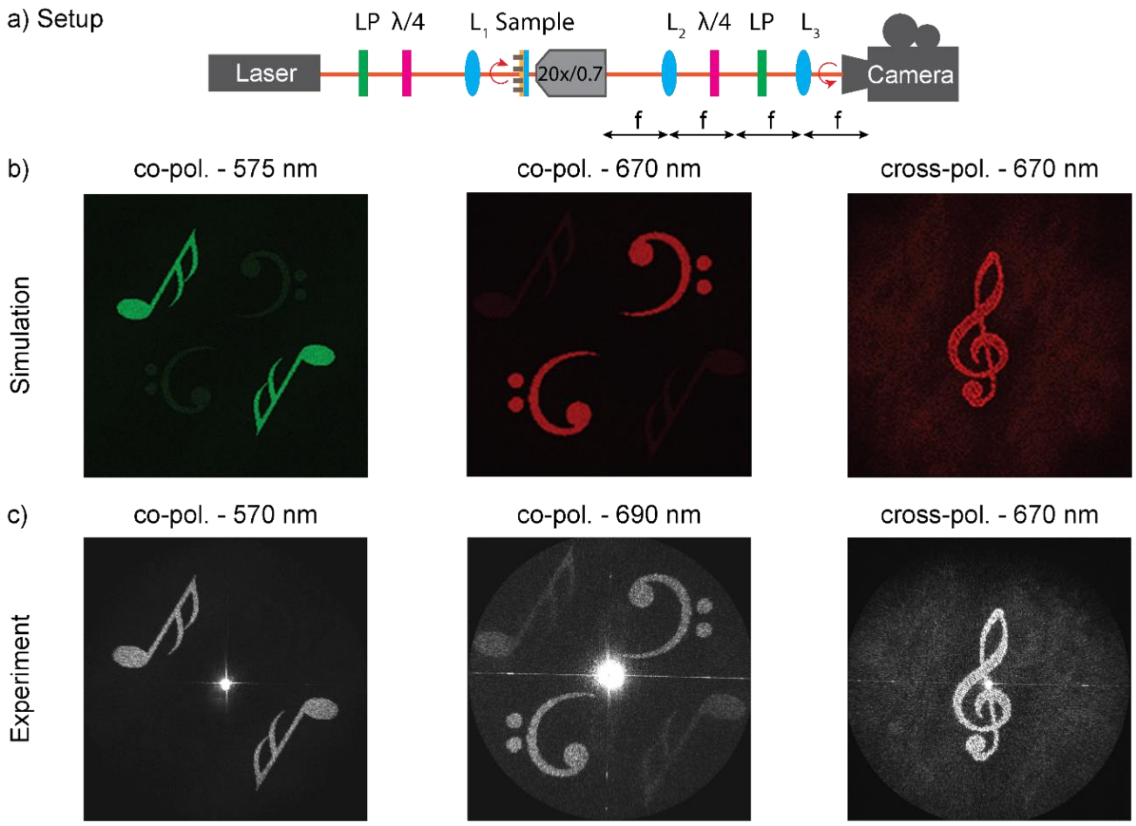

Figure 4.10 Experimental setup, target images and measured holograms. a) As laser source, a super-continuum laser with monochromator is used with tunable wavelength. The input polarization state is circular, while the output state can be changed from the co- to the cross-circular polarization state. The encoded Fourier-holograms are imaged using a monochrome camera and a 4f-setup. b) Simulated holograms. The musical notes and bass clefs are the target images at 575 nm and 670 nm in the circular co-polarization state. In the cross-polarization state, at 670 nm, the treble clef appears based on the Pancharatnam-Berry phase. c) Experimentally measured holograms in the corresponding polarization channels. The wavelengths for optimal image reconstruction are slightly shifted in the co-polarization channel compared to the design wavelength [31].

The experimentally measured holograms are shown in Figure 4.10c. To investigate the holograms' spectral characteristics, the incident wavelength is tuned through the visible spectrum in 10 nm steps. The two images in the co-polarization channel which come closest to the theoretical expectations are imaged at 570 nm and 690 nm. At 570 nm, the musical notes are visible without the presence of the sub-images. The zeroth-order spot originates from unconverted light which passes the metasurface and unideal polarization filtering. At 690 nm, the bass clefs are dominant and the musical notes are mostly suppressed. The zeroth-order spot becomes stronger. This behavior can be explained by the unideal fabrication of the nanostructures. The surface roughness of the silicon fins and the unideal shape deviate from the ideal case in the simulation.

Thus, the transmittance of the individual structures can deviate from the design. The fact that the wavelength is shifted by 20 nm to a longer wavelength compared to the design wavelength is also an indicator of fabrication tolerances since the fabricated antennas tend to be larger than originally designed. In both holograms the sub-images cannot be avoided completely because a decent amount of crosstalk is tolerated in the hologram design. However, in both cases of the amplitude holograms, the target holographic images are dominant and coincide with the calculated target images.

To reconstruct the phase-only hologram, the output polarizer is rotated so that the circular cross-polarization state is passing to the camera. Thus, the treble clef based on the Pancharatnam-Berry phase is reconstructed for the design wavelength of 670 nm, near the highest cross-polarization conversion efficiency (see Figure 4.8b). The zeroth-order spot is neglectably small and primarily originates from imperfect polarization filtering. The high-quality holographic image is embedded in a low background signal predicted from the hologram design. In general, phase-only holograms based on the Pancharatnam-Berry phase are wavelength-independent. However, since the antennas' operation range is limited, the phase-only hologram can only be reconstructed in a certain range where the hologram transmittance is larger than zero (compare to Figure 4.8a and b).

In addition to the image reconstruction of the amplitude holograms at the design wavelength 575 nm and 670 nm, the transition in between is investigated, as well. From the calculated transmittance of the individual structures shown in Figure 4.8a, one would expect a change in the contrast between the two sub-holograms. The experimentally measured images for the wavelengths of 600 nm, 630 nm, and 660 nm confirm the assumption (Figure 4.11). For wavelengths where the transmission ratio between the nanostructures deviates from the design

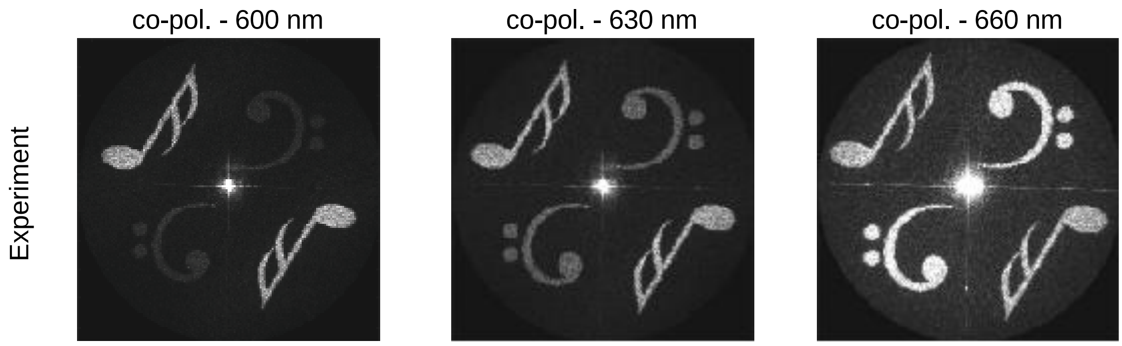

Figure 4.11 Characterization of the amplitude holograms at wavelengths different from the design wavelength. Changing the input wavelength results in different brightness of the partial holograms [31].

wavelengths, both holograms are reconstructed with different brightness. Note that the images are all grayscale because of the use of a monochrome camera. This camera is used because of its high sensitivity and large detector area to achieve a high image quality.

In addition, the photon sieve holograms are reconstructed by using a commercially available webcam instead of the monochrome camera in the setup. The colored images of the amplitude holograms in the circular co-polarization channel RCP to RCP are shown in Figure 4.12a. The transition from 510 nm to 710 nm is equal to the measurement with the monochrome camera. For longer wavelengths above 630 nm, the zeroth-order spot increases and the background becomes more dominant.

Figure 4.12b shows the reconstructed phase-only hologram in the cross-polarization channel from RCP to LCP at the wavelength of 640 nm, 670 nm, and 700 nm. The phase-only hologram is generally wavelength independent. However, in the case of 640 nm, the weak background signal

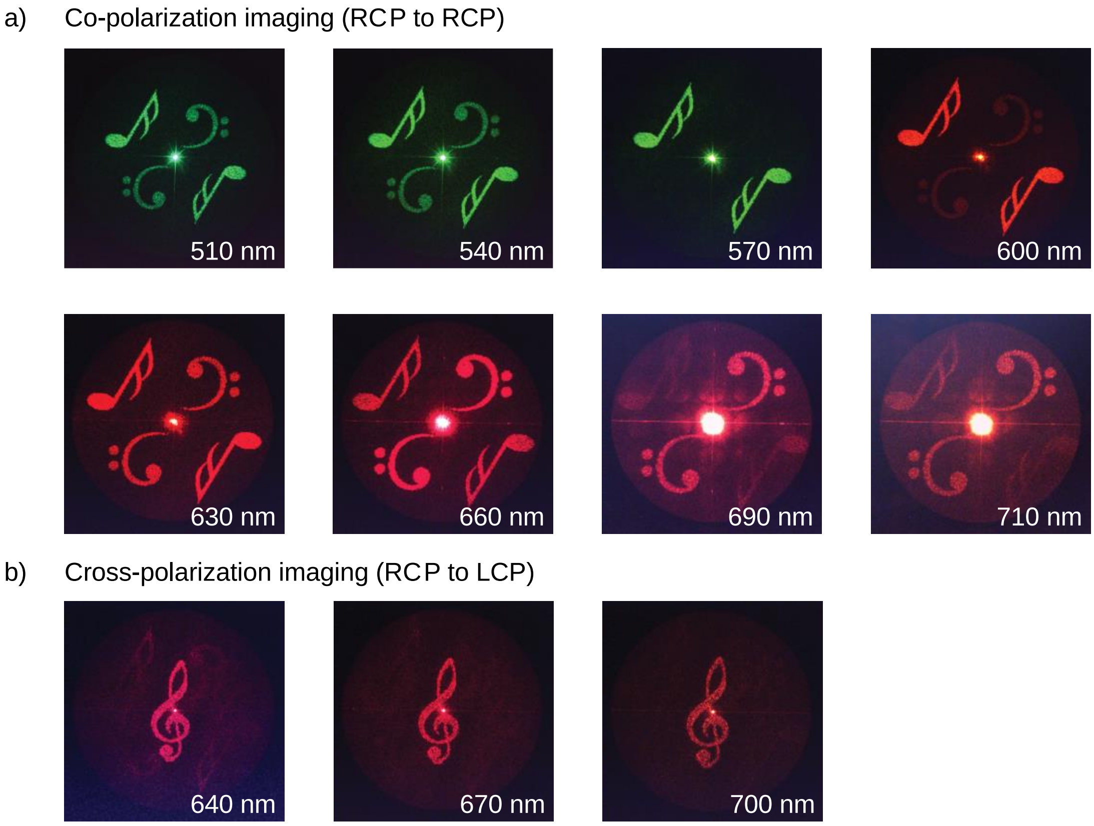

Figure 4.12 Reconstruction of the photon sieve hologram by using an RGB camera. a) Reconstruction of the amplitude-only holograms from 510 nm to 710 nm in the polarization channel from RCP to RCP. b) Reconstruction of the phase-only hologram at the wavelength of 640 nm, 670 nm, and 700 nm in the polarization channel from RCP to LCP.

contains information of the other images. In all cases the incident laser power and the exposure time of the camera are adapted so that the detected image is not saturated. Saturation is only accepted in the zeroth-order spot.

4.1.6 Short conclusion of colored photon sieve holography

In conclusion, a wavelength-multiplexed dual-amplitude hologram combined with a phase-only hologram is designed based on the photon sieve principle. The photon sieve consists of a gold film filled with square and rectangular apertures in an aperiodic arrangement. The wavelength selectivity of the used apertures is realized by filling them with silicon antennas with identical cross-sections for spectral filtering. By tuning the lateral dimension of the silicon antennas, the transmittance is tuned to an equal value for both antenna types in a circular co-polarization channel. At the second design wavelength, the square structure transmits light, while the rectangular structures transmittance is a multiple smaller in the same polarization channel. This behavior is utilized to encode two correlated amplitude-only Fourier-holograms in the arrangement of the two aperture types. In addition, due to the rectangular design, a third phase-only Fourier-hologram is added to the metasurface hologram in the circular cross-polarization channel. The different holograms can be read out by switching the wavelength and changing the polarization channel.

The fabrication of the photon sieve hologram is comparable to the standard fabrication process of all-dielectric nanostructures based on EBL, lift-off, and etching processes except for one difference: The gold film must be placed between the antennas. This is realized by depositing the gold layer after the ICP-RIE etching of the silicon antennas and utilizing an optimized chromium etching mask as a sacrificial layer to remove the gold on top of the silicon antennas by an additional wet etching process.

5 Nonlinear metasurface color-holography

Similar to linear metasurface holograms, phase modulation techniques have been transferred to the nonlinear regime, enabling the creation of holographic images on wavelengths different from the incoming beam [107-111]. The incoming laser beam with frequency ω can interact with plasmonic or dielectric nanoantenna arrangements and thus create new signals of frequency 2ω, 3ω, or higher order. Due to the subwavelength thickness of metasurfaces, quasi-phase-matching techniques like the poling of nonlinear crystals in not required [112-114]. In the case of plasmonic nanoantennas, the light interacts with the metal's conduction band electrons. Strong electric field enhancements can occur at the surface of the nanoantennas so that higher harmonics are generated, depending on the symmetry of the particle or lattice [62]. Mao et al. presented a diatomic nonlinear metasurface for Fourier- and real-space image encoding. As illustrated in

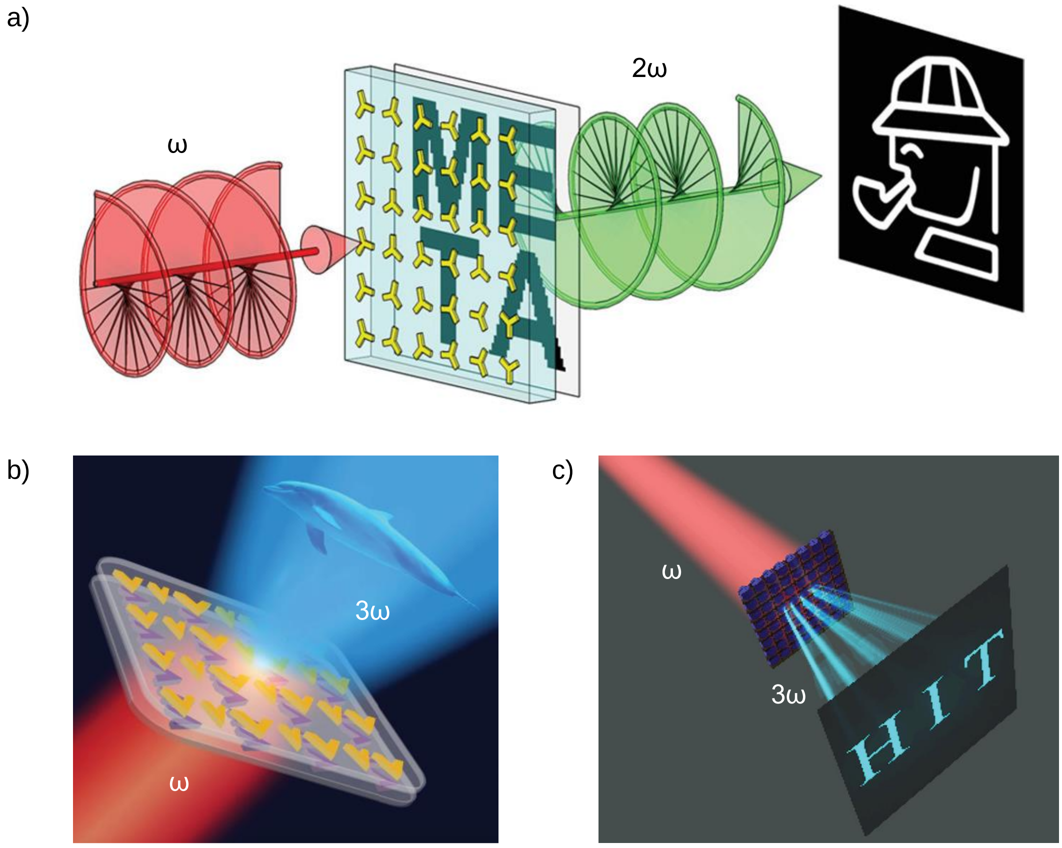

Figure 5.1 a) Nonlinear plasmonic metasurface for Fourier and Real space image encryption, simultaneously. The image is reconstructed at the doubled frequency compared to the incident light [115]. b) Nonlinear plasmonic metasurface based on stacked V-shaped antennas for multiple image encryption. When the metasurface is illuminated with light of the frequency ω, the image is reconstructed at the frequency 3ω [116]. c) A nonlinear dielectric metasurface based on C-shaped Si antennas for THG with 0 to 2π phase control [111].

Figure 5.1a, by pumping a circularly polarized fundamental wave with frequency ω, the second harmonic generation (SHG) waves can form two different holographic images in the Fourier- and real-space with frequency 2ω [115]. Additionally, metasurfaces based on third-harmonic generation (THG) can be realized as illustrated in Figure 5.1b. In this case, the image is reconstructed at frequency 3ω using plasmonic V-shaped antennas [116]. In its dielectric counterpart, the light is mostly confined within the nano resonators and interacts with the material of the resonators. If the material of the resonators exhibits a nonlinear susceptibility larger than zero, nonlinear signals can be generated [117]. Gao et al. designed a THG-based nonlinear hologram using C-shaped silicon nanoantennas: By slightly varying the geometry of the C-shaped antennas, a phase shift can be introduced to the nonlinear signal. Compared to the plasmonic counterparts, Gao et al. already achieved an increased conversion efficiency by two orders of magnitude ($\eta = \frac{P_{3\omega}}{P_{\omega}} = 1.1 \times 10^{-6}$) [111] (Figure 5.1c).

In addition to purely nonlinear holograms, multiplexing technologies or stacking of several layers of nanoantennas can be utilized to increase the functionality and the application range of nonlinear metasurface holograms for holographic displays [27, 116]. However, the creation of colored nonlinear holographic images based on multiple harmonic generations is a challenging task. First, nonlinear processes of different orders scale differently with the intensity of the incident laser beam. Second, the nonlinear response of plasmonic nanoantennas strongly depends on fabrication tolerances and their environment. In this section, a scheme to realize a bi-colored nonlinear metasurface hologram based on the second and third harmonic generation of plasmonic metaatoms is presented. Before moving on to the metasurface concept, the basics of nonlinear generations are shortly summarized and the concept of the nonlinear Pancharatnam-Berry phase, which is exploited to generate the nonlinear bi-color phase-only hologram, is introduced. Parts of the following chapter have already been published in [32].

5.1 Nonlinear harmonic generation processes

The presence of strong optical excitation, the material optical answer can be nonlinear. This means that the material polarization $P(t)$ does no longer scale linearly with the electric field $E(t)$ of the incident light, and the optical answer of the material becomes nonlinear. Thus, higher harmonic polarizations can radiate harmonic signals. Typically, these effects increase in the presence of laser light with high intensity. To describe the nonlinear optical interactions of a material, the material polarization can be expressed as a Taylor-expansion when assuming a monochromatic electric field in form of $E(t) = E_0 e^{-i\omega_1 t} + c.c$:

$$P(t) = \epsilon_0 \left[\chi^{(1)} E(t) + \chi^{(2)} E(t)E(t) + \chi^{(3)} E(t)E(t)E(t) + \cdots\right] \tag{5.1}$$

The tensors $\chi^{(2)}$ and $\chi^{(3)}$, of rank three and four respectively, describe the nonlinear susceptibility. Generally, the susceptibility is dispersive so that each tensor element depends on the electric fields' frequency ω. Each term with a susceptibility tensor of order $n > 1$ can be considered a source of a nonlinear signal. The strength of the generated nonlinear signal depends on the driving electric field strength and the strength of the nonlinear susceptibility $\chi^{(n)}$. Further, the nonlinear signal also depends on the symmetry of the material. For example, a second-order nonlinearity does not exist in a centrosymmetric material. In a centrosymmetric material, the second-order material polarization is $\boldsymbol{P}(t) = \epsilon_0\chi^{(2)}\boldsymbol{E}(t)\boldsymbol{E}(t)$, and for the negative polarization $-\boldsymbol{P}(t) = \epsilon_0\chi^{(2)}\left(-\boldsymbol{E}(t)\right)\left(-\boldsymbol{E}(t)\right) = \epsilon_0\chi^{(2)}\boldsymbol{E}(t)\boldsymbol{E}(t)$, which is only valid for $\chi^{(2)} = 0$. This is also valid for the symmetry of nanoparticles [118].

5.1.1 Second-order nonlinearities

The most prominent nonlinear light-matter interaction is the second harmonic generation (SHG). Shortly after the development of the first laser, Franken et al. (1961) discovered an SHG signal by focusing laser light with a wavelength of 694.3 nm on a crystalline quartz sample and detecting a signal of 347.2 nm [119]. The electric light field of a laser beam with frequency ω can be described as

$$E(t) = E_0 e^{-i\omega_1 t} + c.c. \tag{5.2}$$

If this electric field incident on a material with second-order susceptibility $\chi^{(2)} \neq 0$, a nonlinear material polarization is created and can be expressed as

$$P^{(2)}(t) = 2\epsilon_0\chi^{(2)}EE^* + \left(\epsilon_0\chi^{(2)}E^2e^{-i2\omega_1 t} + c.c.\right). \tag{5.3}$$

The first term of the second-order material polarization is known as optical rectification (OR), creating a static electric field in the material. The second term is known as a second-harmonic generation. In a simple picture, one can assume, that two photons of frequency ω_1 are merged into one photon of frequency $2\omega_1$ by the material, as it is illustrated in the photon energy diagram in Figure 5.2a.

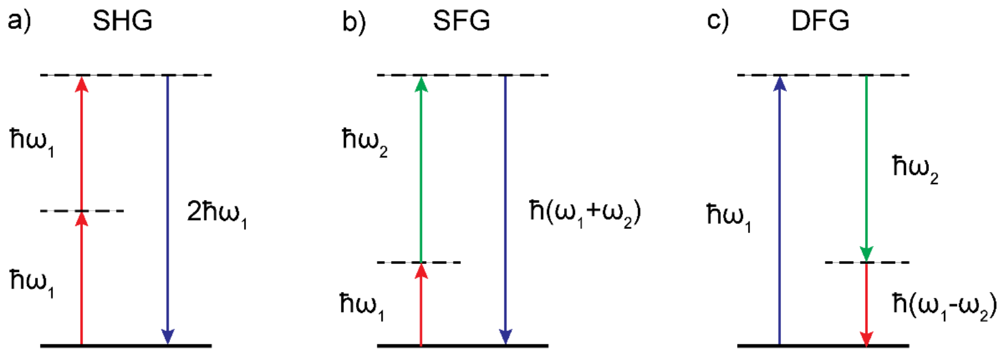

Figure 5.2 Photon Energy diagram of a) second-harmonic generation (SHG), b) sum-frequency generation (SFG) and c) difference-frequency generation (DFG).

SHG is not the only nonlinear process of order two that can appear. To discuss other processes that are supported by $\chi^{(2)}$ nonlinearities, one can assume a light source consisting of two distinct frequencies, so that the electrical field is given by

$$E(t) = E_1e^{-i\omega_1 t} + E_2e^{-i\omega_2 t} + c.c. \tag{5.4}$$

Thus, the nonlinear material polarization equates to

$$P^{(2)}(t) = \epsilon_0\chi^{(2)}\left[E_1^2e^{-i2\omega_1 t} + E_2^2e^{-i2\omega_2 t} + 2E_1E_2e^{-i(\omega_1+\omega_2)t} + 2E_1E_2^*e^{-i(\omega_1-\omega_2)t} + c.c.\right] + 2\epsilon_0\chi^{(2)}[E_1E_1^* + E_2E_2^*]. \tag{5.5}$$

From this expression, one can derive the different nonlinear processes of the second order:

SHG: $$P(2\omega_1) = \epsilon_0 \chi^{(2)} E_1^2 e^{-i2\omega_1 t} \tag{5.6}$$

SHG: $$P(2\omega_2) = \epsilon_0 \chi^{(2)} E_2^2 e^{-i2\omega_2 t} \tag{5.7}$$

SFG: $$P(\omega_1 + \omega_2) = \epsilon_0 \chi^{(2)} E_1 E_2 e^{-i(\omega_1+\omega_2)t} \tag{5.8}$$

DFG: $$P(\omega_1 - \omega_2) = \epsilon_0 \chi^{(2)} E_1 E_2^* e^{-i(\omega_1-\omega_2)t} \tag{5.9}$$

OR: $$P(0) = \epsilon_0 \chi^{(2)} (E_1 E_1^* + E_2 E_2^*) \tag{5.10}$$

Overall, we obtain five terms of nonlinear polarizations of the second-order plus their complex conjugation. Equations (5.6) and (5.7) describe the second-harmonic generation (SHG) of the frequencies ω_1 and ω_2. Here, the material polarization depends quadratically on the electric field amplitudes E_1 and E_2. Equation (5.8) describes the sum-frequency generation (SFG). In this case, the new photon with frequency ω_3 is generated according to $\omega_3 = \omega_1 + \omega_2$ (Figure 5.2b). Equation (5.9) is known as difference-frequency generation (DFG). In this process, the system is excited by a photon of frequency ω_1. The excited state then decays to the ground state by emitting two photons with frequencies ω_2 and $\omega_3 = \omega_2 - \omega_1$ (Figure 5.2c). This process is utilized in optic parametric oscillators, which are widely used as tunable laser sources in the infrared [118].

5.1.2 Third-order nonlinearities

The nonlinear susceptibility tensor $\chi^{(3)}$ describes the third-order nonlinearity of a material. In general, the tensor consists of 81 elements that are nonzero for crystalline solids with low symmetry. However, the number of independent tensor elements decreases if the nonlinear crystals' spatial symmetry increases. For an isotropic material, only three independent elements remain [118].

As discussed for the second-order process, the electric field $E(t)$ contains generally many frequency components $(\omega_1, \omega_2, \ldots)$, which can be used to form a detailed description of the nonlinear polarization of the third order. However, this expression becomes very complex, and the focus here is on the third-harmonic generation to analyze nonlinear metasurface signals. One can express the third-order nonlinear material polarization as

$$\boldsymbol{P}(t) = \epsilon_0 \chi^{(3)} \boldsymbol{E}(t)\boldsymbol{E}(t)\boldsymbol{E}(t) \tag{5.11}$$

By considering a monochromatic electric field $E(t) = E_0 \cos(\omega t)$ as a driving field for the material polarization, we find that the polarization results in

$$\boldsymbol{P}(t) = \epsilon_0 \chi^{(3)} E^3 \cdot \left(\frac{1}{4}\cos(3\omega t) + \frac{3}{4}\cos(\omega t)\right), \tag{5.12}$$

$$\text{with } \cos^3(\omega t) = \frac{1}{4}\cos(3\omega t) + \frac{3}{4}\cos(\omega t).$$

Equation (5.12) consists of two summands, while the first term oscillates with the tripled frequency of the driving field 3ω. This term can be considered as the source of the emitted THG signal. The other term oscillates with the exiting frequency ω. The phenomena are similar to an SHG process, even though in the case of THG, the material polarization depends on the electric field strength to the power of three. As illustrated in the photon energy diagram in Figure 5.3, in the case of THG three photons of frequency ω_1 are transformed to one photon with the frequency $3\omega_1$.

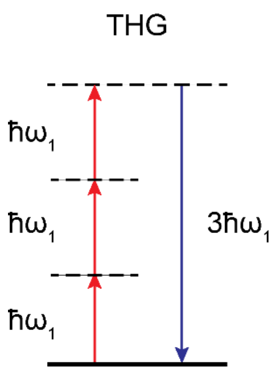

Figure 5.3 Photon energy diagram of third-harmonic generation. Three photons of frequency ω_1 generate one photon of frequency $3\omega_1$.

Analog to the discussed second-harmonic processes, the third-harmonic processes can also be considered in more detail by applying an electric field with several frequency components. Thus, higher-order frequency mixing can be derived with all possible frequency combinations [118].

5.2 Symmetry selection rules for circularly polarized harmonic generations

In artificially structured nanoantennas, the nonlinear processes underlie symmetry-based selection rules for the circular polarization states. These rules determine, depending on the order of the nonlinear process and the symmetry of the nanoantenna, whether the process is allowed or not [107, 120]. The universal concept of spin-rotation coupling for phase modulation in the nonlinear regime, which has been presented by Li et. al [107], can be transferred to plasmonic, as well as dielectric nanostructures.

Let us consider a C2 symmetric nanoantenna, which resembles a dielectric dipole. The nomenclature C*m* (where *m* is an integer larger than zero) means, that one considers the rotation symmetric antenna around the z-axis when the antenna is placed in the x-y-plane as depicted in Figure 5.4. In the case of a C2 antenna, the antenna returns back into its initial state after an in-plane rotation of $\frac{2\pi}{2}$, which corresponds to the C2 class. In the case of the C3 antenna, the rotation would be $\frac{2\pi}{3}$, and so on. Potentially interesting geometries are shown in Table 5.1.

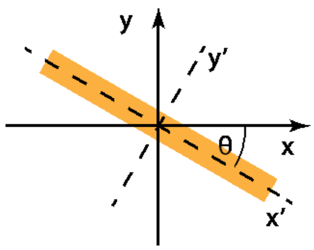

Figure 5.4 Simple depiction of a dipole antenna arranged in the x-y plane rotated by the angle θ with respect to the x-axis. The z- axis is perpendicular to the x-y plane. The x'-y' plane is the local frame of the antenna.

Let us assume a dipole antenna as illustrated in Figure 5.4 is exposed to circularly polarized light of the form $E^{\sigma} = \frac{1}{\sqrt{2}} E_0(e_x + i\sigma e_y)$, with $\sigma = \pm 1$. σ indicates the handedness of the circular light polarization: $\sigma = 1$ stands for left-handed circularly polarized light (LCP) and $\sigma = -1$ stands for right handed polarized light (RCP). If the light interacts with a dipole antenna, an effective nonlinear dipole moment is formed:

$$P_\theta^{n\omega} = \alpha_\theta (E^\sigma)^n \tag{5.13}$$

where ω denotes the frequency of electric field E^σ, $\alpha_\theta$is the *n*th harmonic polarizability tensor of the nanoantenna which is rotated by the angle θ with respect to the lab frame. The local electric field E_{local}^σ (x'-y' frame) of the rotating antenna by the angle of θ can be expressed as

$$E_{local}^\sigma = E^\sigma \, e^{i\sigma\theta}. \tag{5.14}$$

From the antenna's point of view, its polarizability α_θ is unaffected so that $\alpha_0 = \alpha_\theta|_{\theta=0}$. Thus, one ends up with an expression for the *n*th harmonic nonlinear dipole moment in the local frame:

$$P_{\theta,local}^{n\omega} = \alpha_0 (E_{local}^\sigma)^n = \alpha_0 (E^\sigma)^n e^{in\sigma\theta}. \tag{5.15}$$

This nonlinear dipole moment can be decomposed into two in-plane rotating dipoles, which are characterized by the circular polarization states σ and $-\sigma$:

$$P_{\theta,local}^{n\omega} = P_{\theta,local,\sigma}^{n\omega} + P_{\theta,local,-\sigma}^{n\omega}, \text{ with } P_{\theta,local,\sigma}^{n\omega}, P_{\theta,local,-\sigma}^{n\omega} \propto e^{in\sigma\theta} \tag{5.16}$$

The back-transformation into the laboratory frame (x, y) results in two rotating dipole moments:

$$P_{\theta,\sigma}^{n\omega} = P_{\theta,local,\sigma}^{n\omega} e^{-i\sigma\theta} \propto e^{i(n-1)\sigma\theta} \tag{5.17}$$

$$P_{\theta,-\sigma}^{n\omega} = P_{\theta,local,-\sigma}^{n\omega} e^{i\sigma\theta} \propto e^{i(n+1)\sigma\theta}$$

For the nonlinear polarizabilities in the co-polarization channel (σ, σ) and the cross-polarization channel $(\sigma, -\sigma)$ one can show that

$$\alpha_{\theta,\sigma,\sigma}^{n\omega} \propto e^{i(n-1)\sigma\theta} \tag{5.18}$$

$$\alpha_{\theta,-\sigma,\sigma}^{n\omega} \propto e^{i(n+1)\sigma\theta} \tag{5.19}$$

Thus, one can find the geometric phases $(n-1)\sigma\theta$ and $(n+1)\sigma\theta$ of the nth harmonic processes. So far, the symmetry of the nanoantennas has not been taken under consideration. According to Neumann's principle, the physical property of an antenna is invariant under a coordinate transformation if the antenna is invariant under the same coordinate transformation [121]. This applies to both the antenna's material symmetry and the antenna symmetry. In the case of our two-dimensional nanoantennas, an m-fold rotation symmetric antenna is invariant under a rotation $\phi = \frac{2\pi}{m}$ if the antenna consists of an isotropic material like gold. According to the selection rules for harmonic generations for circular polarization states, meta-atoms with an m-fold rotation symmetry generate only higher harmonics of the order n if

$$n = lm \pm 1 \tag{5.20}$$

is satisfied, where l is an integer larger than zero. The signs '$+$' and '$-$'indicate whether the generated harmonic signal is in the same or opposite circular polarization channel [107, 120].

The possible harmonic generation processes of several Cm symmetric meta-atoms are summarized in Table 5.1. C1 symmetric structures support any higher harmonic process. According to equation (5.20), if $m \leq 2$ and m is an even number, only odd higher harmonics are allowed. If $m \leq 3$ and m is an odd number, only even higher harmonics are allowed. The phase dependency is given by the summand lm of equation (5.20). For example: If $l = 3$ and $m = 1$, then $n = 1 \cdot 3 - 1 = 2$. This means that second-harmonic generation is supported by a C3

harmonic order n	C1 	C2	C3 	C4 
1	2θ (-σ)	2θ (-σ)		
2	1θ (σ) 3θ (-σ)		3θ (-σ)	
3	2θ (σ) 4θ (-σ)	2θ (σ) 4θ (-σ)		4θ (-σ)
4	3θ (σ) 5θ (-σ)		3θ (σ)	

Table 5.1 Pancharatnam-Berry phases for different harmonic generations and different rotation symmetries of the meta-atoms. The rotation symmetry (C1, C2, C3, C4) of a nano-particle and the order of the harmonic generation (n = 1, 2, 3, 4, …) determines which phase is accumulated with respect to the rotation angle θ of a nanoantenna in the lab frame.

symmetric structure and the phase is introduced to the second-harmonic by a rotation equal to 3θ. The nonlinear signal is generated with opposite-handedness as the incident circular polarization state because of the '-1'.

5.3 Nonlinear bi-color holography

Nonlinear metasurface phase-holography shows the potential of metasurfaces to not only manipulate the phase of an incident light wave within the nanometer-scale, but also to convert its frequency. By utilizing the concept of the Pancharatnam-Berry phase, I want to show that it is generally possible to generate colored holographic images based on harmonic generation processes of different orders. As illustrated in Figure 5.5, a coherent light beam is used to illuminate a plasmonic metasurface with randomly distributed two-fold (C2) and three-fold (C3) rotation-symmetric gold antennas. The orientation angle of each antenna in the square lattice (with respect to the lab frame) carries the holographic image information. When excited by the coherent light beam with frequency ω, the C2 and C3 antennas generate higher harmonics. The metasurface is designed so that the SHG (2ω) signal emitted by the C3 antennas form the house wall and treetop (red color), while the C2 antennas carry the THG (3ω) phase information, the roof and tree trunk, colored in blue. The hologram is designed in the Fourier space.

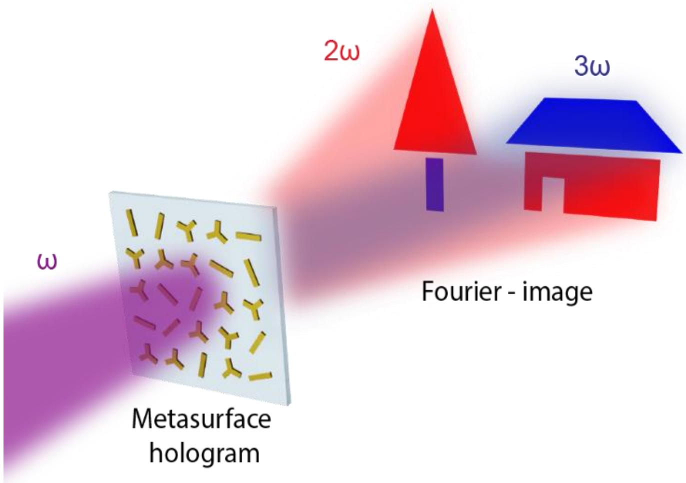

Figure 5.5 Nonlinear bi-colored holographic image encoding based on plasmonic nano-antennas. The plasmonic nano-antennas support different nonlinear processes based on their rotation symmetry. While the C2- and C3-symmetric nano-antennas are randomly distributed in a square lattice, their rotation angle is significant for the image encoding. When the metasurface is illuminated near the resonance frequency ω, a nonlinear Fourier hologram is generated with frequencies 2ω and 3ω [32].

5.3.1 Metasurface design and fabrication

In comparison to linear metasurface phase holograms, a few difficulties appear when designing nonlinear holograms based on multiple nonlinear processes. In the design, it is important to consider not only the encoded objects' shape, but also the image's color brightness. In the case of a bi-color hologram based on an SHG and THG process, it is of high interest to control the emitted SHG and THG intensities I_{SHG} and I_{THG}, so that both colors can be adjusted to have the desired intensity distributions in the images. One way to influence the intensity ratio is the change the electric field strength $E(\omega)$ of the fundamental beam. The nonlinear material polarization, which can be considered as the nonlinear source term, scales quadratically and cubically with $E(\omega)$ in the case of SHG and THG, respectively, as described in sections 5.1.1 and 5.1.2. Consequently, the intensity ratio of the emitted signals depends on the intensity of the fundamental beam. Another possibility is to choose different nanoantenna geometries which can principally have different nonlinear efficiencies. If the meta-atom shape is fixed, another way to control the nonlinear signal strength is the resonance of the selected particles. Far off-resonant excitations of plasmonic nanoparticles generally exhibit weaker nonlinear responses. Furthermore, the number of different nanoantennas placed in the metasurface is equal to the number of nonlinear emitters and therefore directly related to the nonlinear SHG and THG intensities.

To design the nonlinear bi-colored hologram, first, a suitable target wavelength range in the visible spectrum is chosen, which is attractive for display application and detectable with common optical devices and components. As nanoantennas, the simplest design for THG and SHG is the choice of two-fold and three-fold rotation symmetric antennas. Both antenna types enable the phase modulation of the nonlinear signal in the circular cross-polarization channel. This is a great advantage since nonlinear signals are generally very weak. Noise and other unwanted signals which could potentially influence the quality of the holograms can be suppressed by polarization filtering. Note that C1 symmetry also enables SHG and THG phase modulation, but it is not possible to design an independent phase profile for SHG and THG in the same polarization state simultaneously via the rotation of a single antenna type (Table 5.1).

As discussed in section 5.2, the introduced phase of a C3 antenna rotated by the angle θ with respect to the lab frame is $\varphi_{C3}^{SHG} = -\sigma 3\theta$. Exciting the C3 antenna with RCP light, the phase shift can be detected in the LCP output channel and vice versa. In the case of the C2 antenna, which is used to introduce a phase in the generated third-harmonic signal, the relation holds $\varphi_{C2}^{THG} =$

$-\sigma 4\theta$. Note that the C2 antenna also influenced the THG signal in the co-polarization channel $\varphi_{C2}^{THG} = \sigma 2\theta$. However, the signal can be simply filtered out by polarization filtering. On the basis of the selected geometry and the phase relations, the phase distribution for the hologram can be calculated with the Gerchberg-Saxton algorithm [29]. The bi-colored image shown in Figure 5.5 is separated into two sub-holograms: The blue and red parts of the images are encoded in the antennas' rotation angles of the C2 and C3 structures, respectively.

When calculating the phase masks of the two sub-images, one has to consider the wavelength of the SHG and THG signals when projecting the target image to the NA space, which is collected by the MO in the experiment. If the metasurface is treated as a diffraction grating with lattice constant d, the first diffraction order radiates under an angle $\alpha = \arcsin\left(\frac{\lambda}{d}\right)$ to the surface normal. Thus, for a fixed lattice constant, the angle α changes when the wavelength λ changes. This is similar to the case of the metasurface hologram. If the metasurface should work at two different wavelengths, the sizes of the sub-images have to be adapted accordingly. In the case of Fourier holograms, the discrete step size $dk = 2\pi/L$ in the k-space is given by the field size L of the metasurface. The corresponding step size needed to compensate the change in the image size in the NA space of the MO is $dk_{NA,SHG} = \frac{dk}{|k_{SHG}|}$ and $dk_{NA,THG} = \frac{dk}{|k_{THG}|}$, where k_{SHG} and k_{THG} are the wave vectors of the nonlinear signals. Finally, the factor by which the images have to be compensated is $\gamma = \frac{dk_{NA,SHG}}{dk_{NA,THG}}$. An illustration of the compensated target images is shown in Figure 5.6, where the cycle indicates the NA=0.42 of the MO. The SHG image size has been shrunk to 2/3 of its original size [122].

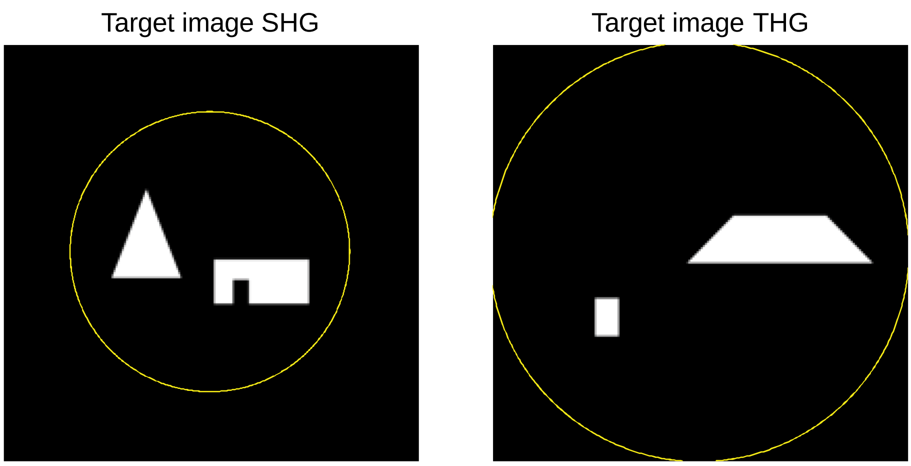

Figure 5.6 Illustration of the image scaling for nonlinear metasurface hologram. The SHG target image has been shrunk to 2/3 of its original size. The circle indicates the NA=0.42 of the used MO in the experiment.

To implement the design idea in a real metasurface, parameter sweeps over the C2 and C3 antenna arm length are performed in an FDTD simulation to calculate the linear transmittance of the antennas. The unit-cell size is 500 nm with periodic boundary conditions. The antenna width and height are 80 nm and 30 nm, respectively. In the simulation, the antenna is placed on a glass substrate with a refractive index of n = 1.44. The upper half-space is set as a vacuum. For the dielectric function of gold, the experimentally measured values by Johnsen and Christy are used [67]. The transmittance of the simulated C2 antenna with an arm length of 310 nm and the C3 antenna with an arm length of 170 nm is plotted in Figure 5.7 (red and blue dashed lines). The transmittance of both structures is below 0.2 in the local minima, indicating a large resonant excitation of the antennas. The location of both resonances is close to 1300 nm.

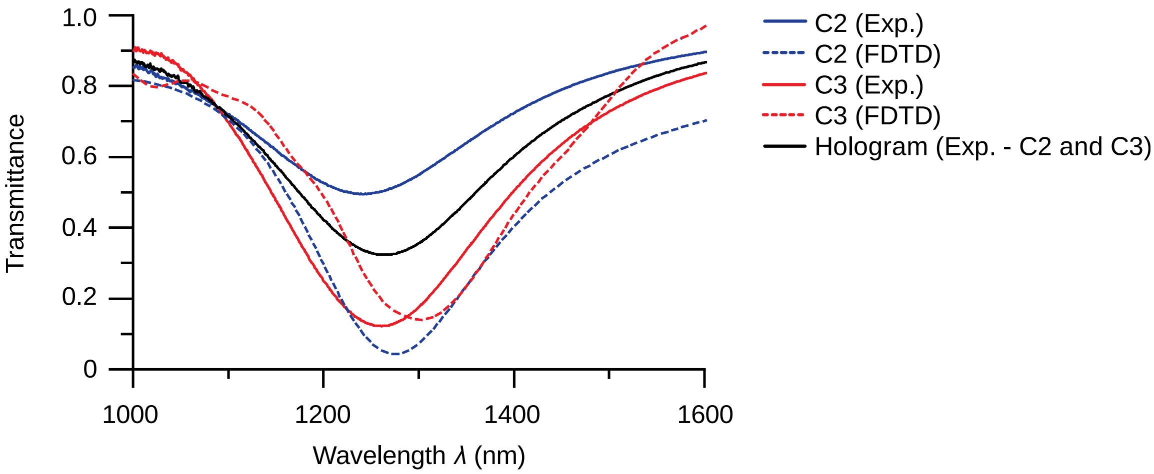

Figure 5.7 Transmittance of the calculated and measured metasurfaces. Dashed blue and red lines: Calculated transmittance based on FDTD-method of C2 and C3 antennas. Solid blue and red lines: Experimentally measured transmittance of a metasurface consisting of only C2 and only C3 antennas using Fourier-transform-infrared spectroscopy. Solid black line: Measured transmittance of the fabricated metasurface hologram consisting of equal amounts of C2 and C3 antennas.

The chosen antenna geometry and SEM images of the fabricated structures are shown in Figure 5.8. To compare the calculated transmittance with the experiment, metasurfaces consisting of only C2 antennas and C3 antennas are fabricated with a phase gradient, as well as the metasurface hologram consisting of equal amounts of C2 and C3 antennas. The metasurface hologram is designed with a random arrangement of the C2 and C3 antennas and carries the phase information of the hologram stored in the orientation of the antennas. The measured transmittance of the fabricated metasurfaces is in good agreement with the calculated values of the single antennas (Figure 5.7). The minima of the metasurface resonances are all located between 1250 nm and 1300 nm. It is striking that the experimentally measured transmittance of the C2 antenna is higher than the transmittance of the C3 antenna, contrary to the simulation results. However, the measured transmittances of the fabricated metasurfaces show that the transmittance of the hologram is roughly equal to the arithmetic mean of the transmittance of the single structure fields.The final hologram consists of 400 × 400 pixels with a unit-cell size of 500 nm × 500 nm, resulting in a hologram pattern of 200 µm × 200 µm.

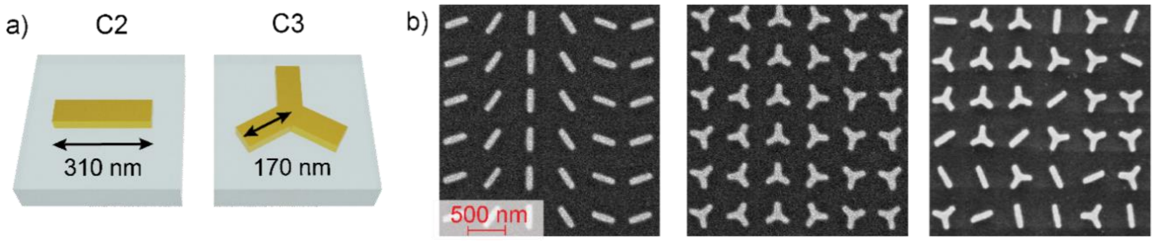

Figure 5.8 Selected antenna designs and SEM images of the fabricated samples. a) C2 and C3 antenna design. The height and width of both antennas is 30 nm and 80 nm. The period is 500 nm. b) SEM images of the C2 only, C3 only, and the metasurface hologram. The metasurface hologram consists of equal amounts of C2 and C3 antennas [32].

5.3.2 Nonlinear holographic image reconstruction

In the following experiment, two different optical setups are used. For the holographic image reconstruction, an imaging system based on a 4f-setup and a CMOS camera to detect the weak nonlinear signals are used. To investigate the spectral characteristics of the nonlinear signals, the camera is replaced by a spectrograph. Both camera and spectrograph are built of different optical components and have different optical responses and losses. Therefore, a quantitative comparison between both measurements is very difficult.

A titanium-sapphire pumped optical parametric oscillator (pulse length 220 fs, repetition rate 80 MHz) is used as a tunable infrared light source for the excitation of the metasurface hologram (Figure 5.9a). The laser light is converted into the right-handed circularly polarized state (RCP) using a linear polarizer (LP) followed by a quarter-wave plate ($\lambda/4$). The light is focused on the metasurface hologram using a lens (L_1) with a focal length of 200 mm. The transmitted light is collected by a microscope objective (MO) with 50× magnification and numerical aperture NA=0.42. A heat absorption filter F_1 blocks the fundamental beam behind the MO to avoid damage to the optical system. The laser power reaches up to 13.3 kW peak power. Two lenses (L_2 and L_3) with a focal length of 100 mm are arranged in a 4f-setup to image the back focal plane of the MO on the camera. The second unit of a quarter-wave plate and a linear polarizer are used to image the cross-polarization channel (RCP to LCP). Spectral filters F_2 in front of the camera can be used to image the SHG and THG signal separately. As a camera, a monochrome CMOS camera is used due to its low readout noise of only 0.9 electrons per second. If no filter is used on position F_2, the SHG and THG signal is imaged simultaneously in grayscale. Figure 5.9b shows the calculated Fourier hologram composed of both wavelengths. For better visualization, red and blue color is used to show the SHG and THG elements of the image.

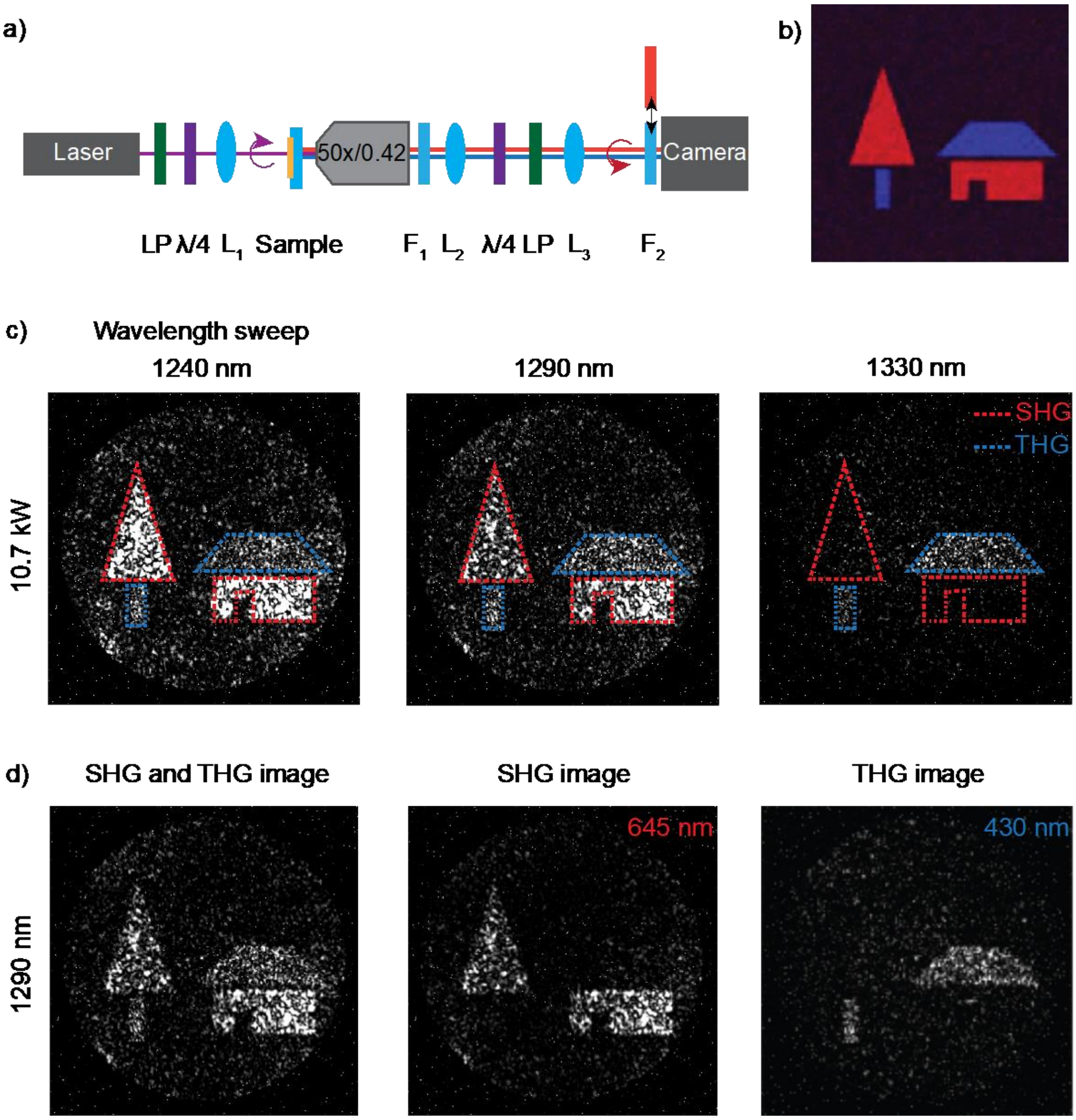

Figure 5.9 Bi-colored nonlinear hologram. a) A tunable near-infrared laser beam is brought into a circular polarization state (RCP) using a linear polarizer (LP) followed by a quarter-wave plate ($\lambda/4$). The light is focused on the metasurface hologram by lens L_1 and captured with a microscope objective (MO) with 50x magnification and numerical aperture NA=0.42. The fundamental beam is blocked behind the MO by the filter F_1 and the nonlinear image is projected on the camera using L_2 and L_3 (4f-setup). The cross-polarization channel can be imaged using a second polarizer unit consisting of a quarter-wave plate and linear polarizer. Different spectral ranges can be imaged by using particular filters F_2 in front of the camera. b) Calculated hologram reconstruction. The SHG and THG signals are colored in red and blue. c) Spectral behavior of the Fourier image. A change in the wavelength of the incident laser influences the intensities of the SHG and THG signals. The red and blue dashed lines indicate areas of weak SHG and THG signals, respectively. d) Fourier image of the metasurface hologram at a wavelength of 1290 nm and peak-power excitation of 10.7 kW. The SHG and THG image can be separated by choosing different optical filters in front of the camera [32].

First, the dependency of the nonlinear signals with respect to the fundamental wavelength is investigated. The fundamental wavelength is swept through the resonance dip of the metasurface hologram while the SHG and THG signals are detected with the CMOS camera. In Figure 5.9c, the reconstructed holograms are shown with red and blue dashed lines to mark the areas of the SHG and THG signals. The images are measured with an exposure time of 270 s for the center wavelength of 1240 nm, 1290 nm, and 1330 nm. The full width of half maximum of the fundamental beam is 17 nm. The set peak power is 10.7 kW. The expected THG signal ranges from 413.3 nm to 443.3 nm, while the SHG ranges from 620 nm to 665 nm. Since no optical filters are used, both signals are imaged in grayscale. For a fundamental wavelength of 1240 nm, the signal within the red dashed lines is stronger than in the blue dashed lines, indicating a dominant SHG process. Changing the wavelength to 1290 nm, while keeping all other parameters in the measurement constant, results in a balancing between the SHG and the THG signal. Further tuning the fundamental beam to 1330 nm results in the absence of the phase-modulated THG signal. Comparing all three images shows the strongest signal intensities at 1240 nm, while they decay for longer wavelengths. This also holds for the background signal. Since the metallic nanostructures underlie fabrication tolerances and exhibit surface roughness, nonlinear signals with random phases can cause background noise. The circular background shape is a result of the k-space limit of the microscope objective in the imaging system.

In Figure 5.9d, the color composition of the nonlinear hologram is investigated. The reconstructed hologram without optical bandpass filters is shown for a wavelength of 1290 nm and peak power of 10.7 kW. By placing a long-pass filter with a band edge of 550 nm in front of the camera, the THG signal with a corresponding wavelength of 430 nm is blocked while the SHG signal with a wavelength of 645 nm passes to the camera. Exchanging the filter with a short-pass filter with a band edge of 500 nm, the THG signal passes to the camera while the SHG is blocked. The measurement shows a clear separation of both filtered images. Thus, cross-talk between the structures can be excluded.

To characterize the spectral behavior of the nonlinear metasurface hologram, the signals are measured in the same configuration as in Figure 5.9a, except that the camera is replaced by a spectrograph. The incident laser peak power for the operation wavelength of 1290 nm is tuned from 2.7 kW to 13.3 kW. Figure 5.10a shows the spectra of the nonlinear signals for the different incident laser powers for an exposure time of 15 s. The first peak, representing the THG signal, is centered at 430 nm with a peak width (FWHM) of 5 nm. The second peak, representing the SHG signal, is centered at 645 nm with an FWHM of 7 nm. As expected from the nonlinear material polarizations, the THG process scales stronger than the SHG process with the source power. Furthermore, from 550 nm to longer wavelengths, one finds a broad background signal, which can be explained by the photoluminescence of gold [123]. To investigate the scaling of both the SHG and THG signals, the spectral intensities are integrated and plotted over the fundamental pump peak powers *P* in a double logarithmic plot in Figure 5.10b. The nonlinear signal intensities I_{SHG}^{fit} and I_{THG}^{fit} follow the quadratic and cubic functions:

$$I_{SHG}^{fit} \sim 2.7 \cdot 10^{-9} \frac{1}{W^2} P^2 \tag{5.21}$$

$$I_{THG}^{fit} \sim 4.4 \cdot 10^{-13} \frac{1}{W^3} P^3. \tag{5.22}$$

The red and blue dashed lines in the graph represent the SHG fit and THG fit, respectively. From the graph, the SHG and THG signals should have the same intensities for an incident power of *P* = 6.1 kW. This value is lower than the estimated power in the case of the imaging system based on the CMOS camera, where an incident power of *P* = 10.7 kW is used for the image reconstruction. The deviations can originate from the different optical systems. In the case of the imaging system, the signal is distributed over a relatively large detector area, lowering the signal-to-noise ratio and increasing the error compared to the spectrograph.

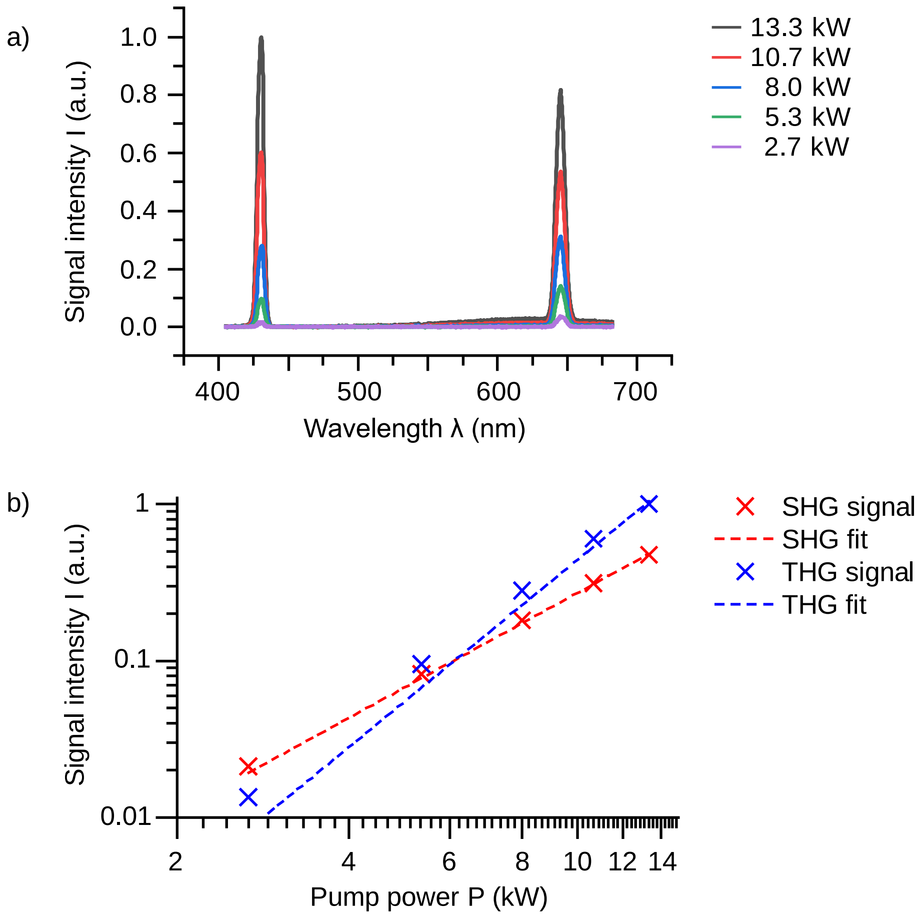

Figure 5.10 Nonlinear spectral response of the nonlinear hologram. a) Nonlinear response of the holographic metasurface for a pump wavelength of 1290 nm and peak powers between 2.7 kW and 13.3 kW. The THG and SHG signal is located at 430 nm and 645 nm, respectively. b) Integrated spectral powers of the SHG and THG signals. The red and blue dashed lines indicate the quadratic and cubic fit function, respectively. The crossing point between the SHG and THG signals is located at approximately 6.1 kW [32].

5.3.3 Short conclusion of nonlinear bi-color holography

In conclusion, a bi-colored metasurface phase-only hologram is designed and fabricated. The metasurface consists of C2 and C3 symmetric plasmonic gold nanoantennas. Based on the Pancharatnam-Berry phase, a bi-colored Fourier hologram is encoded in the arrangement of the antennas. The holographic image is reconstructed by imaging the SHG and THG signals of the nanoantennas in the circular cross-polarization channel from RCP to LCP. The hologram is reconstructed with relatively equal intensity distributions by using an input peak power of 10,7 kW and an exposure time of 270 s. By changing either the input peak power or the input wavelength, the intensity ratio between the SHG and THG signal changes, indicating the sensitivity of the hologram to the laser properties.

Nonlinear metasurfaces like this have very low efficiencies as one can see from the high peak power and long exposure time used for the reconstruction. The conversion efficiency of nonlinear plasmonic metasurfaces is in the range of 10^{-11} to 10^{-12} for SHG and THG from gold split-ring resonators excited by a similar laser system used in this experiment [124, 125]. The low conversion efficiency could be improved by transferring the concept to another material system, a dielectric design, for instance, which has already shown SHG conversion efficiencies in the order of 10^{-6} [126]. However, it is shown that multiple sub-images can be encoded by utilizing different nonlinear processes, which allow a new level of freedom in metasurface hologram design.

6 Conclusion and Outlook

In this thesis, complex optical metasurfaces are investigated as holographic information carriers. The metasurface holograms consist of plasmonic and dielectric nanoantennas, which are tailored to develop applications in advanced holographic devices. In the presented three metasurfaces, the image information is encoded in different polarization and wavelength channels, as well as in different propagation directions.

For directional image encoding, a straightforward approach based on a double-layer system is presented. The functionality of the metasurface can be explained by the design of each layer. One layer is designed to carry the hologram's phase information in an L-shaped structure, while the other layer is utilized to introduce the directionality to the metasurface by a dimer set. It is illustrated that both the amplitude and the phase of transmitted light can be modulated in a linear cross-polarization channel depending on the L-shaped antenna's arm-lengths. The phase hologram covers the full 0 to 2π range and also allows for the amplitude modulation of the transmitted light. The directional metasurface is compared with a single layer L-shaped metasurface. It is demonstrated that the directionality fails to appear in absence of the dimer layer. Furthermore, the overall conversion efficiency of the information channel t_{HV}^{f} in forward propagation direction and the cross-polarization channel V to H drops from 6.7 % to 2 % in the case of the single layer. This is an indicator for a coupling between the two layers which are only separated by 50 nm.

The fabrication of the directional metasurface is done by EBL patterning, electron-beam evaporation, and lift-off processes. By using overlay lithography, the layers can be aligned on top of each other with high lateral precision. A similar directional image encoding can be achieved with chiral structures, fabricated based on focused ion beam milling [91], which is a single-step process. However, the stacking process of two-dimensional structures is a well-established standard process and can be expanded. By adding more layers to a metasurface, one can introduce multiple phase masks which can be combined in different polarization channels to enhance the space-bandwidth product of the holographic metasurface. An ongoing challenge in plasmonic devices is the high optical loss in the visible regime, which makes a phase accumulation of several metasurface layers very difficult, so one should also consider the stacking of metasurfaces consisting of other materials [127].

Apart from directional features of holographic metasurfaces, colored holographic display applications are also current topic in the automotive sector and the sector of virtual reality consumers. To make the metasurface holograms colorful, two approaches are investigated in this work. First, a classical photon sieve is combined with spectral filters. Second, nonlinear nanoantenna responses are utilized to create a pure nonlinear hologram that stores a dual-colored image.

To introduce wavelength multiplexing to a photon sieve hologram, the apertures of a classical photon sieve are replaced by silicon nano filters designed to enable correlated amplitude image encoding, plus the additional encoding of a phase-only hologram. The two different nano filters have a lateral square and rectangular cross-section and are designed so that both structures transmit light at a wavelength of 575 nm, but only the square structure transmits light at 670 nm wavelength. One amplitude hologram is encoded in the arrangement of both nano filter shapes at 575 nm. The second amplitude hologram can be reconstructed when the sample is illuminated with 670 nm and the square-shaped nano filters transmit the light. The choice of the rectangular shape further enables the encoding of a phase-only hologram based on the Pancharatnam-Berry phase. The combination of the amplitude hologram correlation and the phase-only hologram makes the metasurface optically switchable. Depending on the source, an observer can see three different images in two colors. The device shows that different phase modulation concepts can be combined in one metasurface, which can be utilized as information channels. Due to the image correlations for the amplitude holograms, cross-talk cannot be avoided. This concept can generally be expanded to even more information channels. Moreover, the fabrication technique used to place the gold film around the silicon nano filters may be interesting for other metasurface concepts.

Another possibility of colored holographic image encoding is shown by utilizing nonlinear optical effects of plasmonic metaatoms. It is demonstrated that a dual-colored image can be separated into two different kinds of metasurface atoms which support second and third harmonic generation. The selected two- and three-fold rotation symmetric planar structures store the image information in the antenna arrangement. Since both processes, SHG and THG, scale differently with the excitation beam power, the resonances of the nanoantennas and the laser beam properties can be utilized to modulate the nonlinear image response of the hologram. It is demonstrated that the responses of both nonlinear generations behave differently, depending on the excitation beam power and wavelength. Near the holograms resonance at 1290 nm, where the resonances of the individual structures overlap, the nonlinear hologram can be reconstructed with relatively balanced SHG and THG amplitudes by using an excitation peak power of 10.7 kW. Despite the high-power excitation, the nonlinear response of the metasurface is very low and requires exposure times of several minutes. However, noise and unwanted signals can be suppressed by polarization filtering. More interestingly, the basis of multi-harmonic metasurfaces which can be polarization multiplexed is established, because it is demonstrated here that it is generally possible to match different nonlinear signals to the same signal strength. To make this kind of nonlinear metasurface attractive for applications, the efficiency has to be improved tremendously. Several dielectric metasurfaces are used for SHG and conversion efficiencies in the order of 10^{-5} are achieved [126, 128]. However, when talking about efficiencies, one always has to consider that the efficiencies depend on the laser power, wavelength, pulse width, etc. This makes a comparison between different systems very complicated.

In conclusion, this thesis presents examples of three tailored holographic metasurfaces made of different material combinations with different multiplexing schemes. The research area of optical metasurfaces is expanding rapidly and interesting applications are published every day. An ongoing challenge is to improve the efficiencies and enlarge the information channels of metasurface devices, so that bulky optical components and devices like lenses or SLMs can be replaced by nanometer-sized metasurfaces. The high flexibility and the small footprint of metasurfaces make them very attractive for on-chip applications, particularly because of the similar fabrication technologies compared to the semiconductor industry.

References

1. Gabor, D. and W.L. Bragg, *Microscopy by reconstructed wave-fronts.* Proceedings of the Royal Society of London. Series A. Mathematical and Physical Sciences, 1949. **197**(1051): p. 454-487.
2. Maiman, T.H., *Stimulated Optical Radiation in Ruby.* Nature, 1960. **187**(4736): p. 493-494.
3. Leith, E.N. and J. Upatnieks, *Reconstructed Wavefronts and Communication Theory*.* Journal of the Optical Society of America, 1962. **52**(10): p. 1123-1130.
4. Brown, B.R. and A.W. Lohmann, *Complex Spatial Filtering with Binary Masks.* Applied Optics, 1966. **5**(6): p. 967-969.
5. Ackermann, G. and J. Eichler, *Holography: a practical approach.* WILEY-VCH, 2007.
6. Dong, J., C. Jiang, and S. Jia, *Digital holographic metrology based on multi-angle interferometry.* Optics Letters, 2016. **41**(18): p. 4301-4304.
7. Kreis, T., *Application of Digital Holography for Nondestructive Testing and Metrology: A Review.* IEEE Transactions on Industrial Informatics, 2016. **12**(1): p. 240-247.
8. Zhao, R.Z., et al., *Multichannel vectorial holographic display and encryption.* Light-Science & Applications, 2018. **7**: p. 95.
9. Wang, W., et al. *Digital Holographic System for Automotive Augmented Reality Head-Up-Display*. in *2018 IEEE 27th International Symposium on Industrial Electronics (ISIE)*. 2018.
10. Ortuño, M., et al., *Improving the performance of PVA/AA photopolymers for holographic recording.* Optical Materials, 2013. **35**(3): p. 668-673.
11. Stanley, M., et al., *3D electronic holography display system using a 100 Mega-pixel spatial light modulator.* Optical Design and Engineering, 2004. **5249**: p. 297-308.
12. Reichelt, S., et al., *Full-range, complex spatial light modulator for real-time holography.* Optics Letters, 2012. **37**(11): p. 1955-1957.
13. Takaki, Y. and N. Okada, *Hologram generation by horizontal scanning of a high-speed spatial light modulator.* Applied Optics, 2009. **48**(17): p. 3255-3260.
14. Arrizón, V., E. Carreón, and M. Testorf, *Implementation of Fourier array illuminators using pixelated SLM: efficiency limitations.* Optics Communications, 1999. **160**(4): p. 207-213.
15. Hu, J., et al., *A Review on Metasurface: From Principle to Smart Metadevices.* Frontiers in Physics, 2021. **8**(502).
16. Chen, W.T., et al., *A broadband achromatic metalens for focusing and imaging in the visible.* Nature Nanotechnology, 2018. **13**(3): p. 220-+.
17. Yu, N.F., et al., *A Broadband, Background-Free Quarter-Wave Plate Based on Plasmonic Metasurfaces.* Nano Letters, 2012. **12**(12): p. 6328-6333.
18. Ren, H., et al., *Metasurface orbital angular momentum holography.* Nature Communications, 2019. **10**(1): p. 2986.
19. Huang, L.L., S. Zhang, and T. Zentgraf, *Metasurface holography: from fundamentals to applications.* Nanophotonics, 2018. **7**(6): p. 1169-1190.
20. Li, H., et al., *Wideband Transparent Beam-Forming Metadevice with Amplitude- and Phase-Controlled Metasurface.* Physical Review Applied, 2019. **11**(1): p. 014043.

21. Chen, S., et al., *Metasurface-Empowered Optical Multiplexing and Multifunction.* Advanced Materials, 2020. **32**(3): p. 1805912.

22. Du, K., et al., *Optical metasurfaces towards multifunctionality and tunability.* Nanophotonics, 2022.

23. Wang, B., et al., *Visible-Frequency Dielectric Metasurfaces for Multiwavelength Achromatic and Highly Dispersive Holograms.* Nano Letters, 2016. **16**(8): p. 5235–5240.

24. Huang, Y.-W., et al., *Aluminum Plasmonic Multicolor Meta-Hologram.* Nano Letters, 2015. **15**(5): p. 3122-3127.

25. Hu, Y., et al., *Trichromatic and Tripolarization-Channel Holography with Noninterleaved Dielectric Metasurface.* Nano Letters, 2020. **20**(2): p. 994-1002.

26. Jin, L., et al., *Noninterleaved Metasurface for (26-1) Spin- and Wavelength-Encoded Holograms.* Nano Letters, 2018. **18**(12): p. 8016-8024.

27. Ye, W.M., et al., *Spin and wavelength multiplexed nonlinear metasurface holography.* Nature Communications, 2016. **7**: p. 11930.

28. Li, T.Y., et al., *Reconfigurable metasurface hologram by utilizing addressable dynamic pixels.* Optics Express, 2019. **27**(15): p. 21153-21162.

29. R. W. Gerchberg, W.O.S., *A Practical Algorithm for the Determination of the Phase from Image and Diffraction Plane Pictures.* OPTIK, 1972. **2**(35): p. 237-246.

30. Frese, D., et al., *Nonreciprocal Asymmetric Polarization Encryption by Layered Plasmonic Metasurfaces.* Nano Letters, 2019. **19**(6): p. 3976-3980.

31. Frese, D., et al., *A wavelength and polarization selective photon sieve for holographic applications.* Nanophotonics, 2021. **10**(18): p. 4543-.

32. Frese, D., et al., *Nonlinear Bicolor Holography Using Plasmonic Metasurfaces.* ACS Photonics, 2021. **8**(4): p. 1013-1019.

33. Akcay, C., P. Parrein, and J.P. Rolland, *Estimation of longitudinal resolution in optical coherence imaging.* Applied Optics, 2002. **41**(25): p. 5256-5262.

34. Deng, Y. and D. Chu, *Coherence properties of different light sources and their effect on the image sharpness and speckle of holographic displays.* Scientific Reports, 2017. **7**(1): p. 5893.

35. Liu, W., et al., *Dielectric Resonance-Based Optical Metasurfaces: From Fundamentals to Applications.* iScience, 2020. **23**(12): p. 101868.

36. Genevet, P., et al., *Recent advances in planar optics: from plasmonic to dielectric metasurfaces.* Optica, 2017. **4**(1): p. 139-152.

37. Deng, Z.L. and G.X. Li, *Metasurface optical holography.* Materials Today Physics, 2017. **3**: p. 16-32.

38. Wei, Q., et al., *Optical wavefront shaping based on functional metasurfaces.* Nanophotonics, 2020. **9**(5): p. 987-1002.

39. Neshev, D. and I. Aharonovich, *Optical metasurfaces: new generation building blocks for multi-functional optics.* Light: Science & Applications, 2018. **7**(1): p. 58.

40. Genevet, P. and F. Capasso, *Holographic optical metasurfaces: a review of current progress.* Reports on Progress in Physics, 2015. **78**(2): p. 024401.

41. Zheng, G.X., et al., *Metasurface holograms reaching 80% efficiency.* Nature Nanotechnology, 2015. **10**(4): p. 308-312.

42. Zhang, X., et al., *Metasurface-based broadband hologram with high tolerance to fabrication errors.* Scientific Reports, 2016. **6**(1): p. 19856.

43. Huang, L.L., et al., *Three-dimensional optical holography using a plasmonic metasurface.* Nature Communications, 2013. **4**: p. 2808.

44. Zhao, W., et al., *Dielectric Huygens' Metasurface for High-Efficiency Hologram Operating in Transmission Mode.* Scientific Reports, 2016. **6**(1): p. 30613.

45. Butt, H., et al., *Carbon Nanotube Based High Resolution Holograms.* Advanced Materials, 2012. **24**(44): p. OP331-OP336.

46. Huang, K., et al., *Ultrahigh-capacity non-periodic photon sieves operating in visible light.* Nature Communications, 2015. **6**(1): p. 7059.

47. Ni, X.J., A.V. Kildishev, and V.M. Shalaev, *Metasurface holograms for visible light.* Nature Communications, 2013. **4**: p. 2807.

48. Chong, K.E., et al., *Efficient Polarization-Insensitive Complex Wavefront Control Using Huygens' Metasurfaces Based on Dielectric Resonant Meta-atoms.* ACS Photonics, 2016. **3**(4): p. 514-519.

49. Decker, M., et al., *High-Efficiency Dielectric Huygens' Surfaces.* Advanced Optical Materials, 2015. **3**(6): p. 813-820.

50. Yu, N. and F. Capasso, *Flat optics with designer metasurfaces.* Nat Mater, 2014. **13**(2): p. 139-150.

51. Yu, N., et al., *Light propagation with phase discontinuities: generalized laws of reflection and refraction.* Science, 2011. **334**(6054): p. 333-337.

52. Cooley, J.W. and J.W. Tukey, *An algorithm for the machine calculation of complex Fourier series.* Mathematics of Computation, 1965. **19**: p. 297-301.

53. Sun, S., et al., *Electromagnetic metasurfaces: physics and applications.* Advances in Optics and Photonics, 2019. **11**(2): p. 380-479.

54. Yu, N., et al., *Flat Optics: Controlling Wavefronts With Optical Antenna Metasurfaces.* IEEE J SEL TOP QUANT, 2013. **19**(3): p. 4700423-4700423.

55. Daboul, J., *On generalising Abraham-Lorentz equation.* International Journal of Theoretical Physics, 1974. **11**(3): p. 145-147.

56. Zhou, F., Y. Liu, and W. Cai, *Plasmonic holographic imaging with V-shaped nanoantenna array.* Optics Express, 2013. **21**(4): p. 4348-4354.

57. Blanchard, R., et al., *Modeling nanoscale V-shaped antennas for the design of optical phased arrays.* Physical Review B, 2012. **85**(15): p. 155457.

58. Ding, F., A. Pors, and S.I. Bozhevolnyi, *Gradient metasurfaces: a review of fundamentals and applications.* Reports on Progress in Physics, 2017. **81**(2): p. 026401.

59. Wan, W.W., J. Gao, and X.D. Yang, *Full-Color Plasmonic Metasurface Holograms.* ACS Nano, 2016. **10**(12): p. 10671-10680.

60. Zhao, W.Y., et al., *Full-color hologram using spatial multiplexing of dielectric metasurface.* Optics Letters, 2016. **41**(1): p. 147-150.

61. Schlickriede, C., et al., *Imaging through Nonlinear Metalens Using Second Harmonic Generation.* Advanced Materials, 2018. **30**(8).

62. Spreyer, F., et al., *Second harmonic imaging of plasmonic Pancharatnam-Berry phase metasurfaces coupled to monolayers of WS2.* Nanophotonics, 2020. **9**(2): p. 351-360.

63. Ding, X.M., et al., *Ultrathin Pancharatnam-Berry Metasurface with Maximal Cross-Polarization Efficiency.* Advanced Materials, 2015. **27**(7): p. 1195-1200.

64. Walter, F., et al., *Ultrathin Nonlinear Metasurface for Optical Image Encoding.* Nano Letters, 2017. **17**(5): p. 3171-3175.

65. Yee, K.S., *Numerical Solution of Initial Boundary Value Problems Involving Maxwell's Equations in Isotropic Media.* IEEE Transactions on Antennas and Propagation, 1966. **14**: p. 302-307.

66. Callens, M.K., et al., *RCWA and FDTD modeling of light emission from internally structured OLEDs.* Optics Express, 2014. **22**(S3): p. A589-A600.

67. Johnson, P.B. and R.W. Christy, *Optical Constants of the Noble Metals.* Physical Review B, 1972. **6**(12): p. 4370-4379.

68. Khurgin, J.B., *How to deal with the loss in plasmonics and metamaterials.* Nature Nanotechnology, 2015. **10**(1): p. 2-6.

69. Kuznetsov, A.I., et al., *Magnetic light.* Scientific Reports, 2012. **2**(1): p. 492.

70. Cardin, A., K. Fan, and W. Padilla, *Role of loss in all-dielectric metasurfaces.* Optics Express, 2018. **26**(13): p. 17669-17679.

71. Evlyukhin, A.B., et al., *Demonstration of Magnetic Dipole Resonances of Dielectric Nanospheres in the Visible Region.* Nano Letters, 2012. **12**(7): p. 3749-3755.

72. Kivshar Yuri and M. Andrey, *Meta-Optics with Mie Resonances.* Optics Photonics News, 2017. **24**(8): p. 1047-6938.

73. Kruk, S., et al., *Invited Article: Broadband highly efficient dielectric metadevices for polarization control.* APL Photonics, 2016. **1**(3): p. 030801.

74. Zhao, R., et al., *Polarization and Holography Recording in Real- and k-Space Based on Dielectric Metasurface.* Advanced Functional Materials, 2021. **31**(27): p. 2100406.

75. Zheng, G., et al., *Full-space metasurface holograms in the visible range.* Optics Express, 2021. **29**(2): p. 2920-2930.

76. Ma, Z., et al., *All-dielectric reflective half-wave plate metasurface based on the anisotropic excitation of electric and magnetic dipole resonances.* Optics Letters, 2018. **43**(4): p. 911-914.

77. Cheng, J., S. Jafar-Zanjani, and H. Mosallaei, *All-dielectric ultrathin conformal metasurfaces: lensing and cloaking applications at 532 nm wavelength.* Scientific Reports, 2016. **6**: p. 38440.

78. Wang, S.M., et al., *A broadband achromatic metalens in the visible.* Nature Nanotechnology, 2018. **13**(3): p. 227-232.

79. Devlin, R.C., et al., *Broadband high-efficiency dielectric metasurfaces for the visible spectrum.* Proc. Natl. Acad. Sci., 2016. **113**(38): p. 10473-8.

80. Moers, J., et al., *Optimized marker definition for high overlay accuracy e-beam lithography.* Microelectronic Engineering, 2012. **97**: p. 68-71.

81. Vasista, A.B., D.K. Sharma, and G.V.P. Kumar, *Fourier Plane Optical Microscopy and Spectroscopy*, in *digital Encyclopedia of Applied Physics*. 2019, American Cancer Society. p. 1-14.

82. Curto, A.G., et al., *Multipolar radiation of quantum emitters with nanowire optical antennas.* Nature Communications, 2013. **4**(1): p. 1750.

83. Curto, A.G., et al., *Unidirectional Emission of a Quantum Dot Coupled to a Nanoantenna.* Science, 2010. **329**(5994): p. 930-933.

84. Grzela, G., et al., *Nanowire Antenna Emission.* Nano Letters, 2012. **12**(11): p. 5481-5486.

85. Menzel, C., et al., *Asymmetric Transmission of Linearly Polarized Light at Optical Metamaterials.* Physical Review Letters, 2010. **104**(25): p. 253902.

86. Shang, X.-J., et al., *Asymmetric transmission and polarization conversion of linearly polarized waves with bilayer L-shaped metasurfaces.* Applied Physics Express, 2017. **10**(5): p. 052602.

87. Sounas, D.L. and A. Alù, *Non-reciprocal photonics based on time modulation.* Nature Photonics, 2017. **11**(12): p. 774-783.

88. Jalas, D., et al., *What is — and what is not — an optical isolator.* Nature Photonics, 2013. **7**(8): p. 579-582.

89. Fratello, V.J., S.J. Licht, and C.D. Brandle, *Compositional Design of Faraday Rotator Materials.* MRS Proceedings, 2011. **574**: p. 225.

90. Chen, W., B. Javidi, and X.D. Chen, *Advances in optical security systems.* Advances in Optics and Photonics, 2014. **6**(2): p. 120-155.

91. Chen, Y., X. Yang, and J. Gao, *3D Janus plasmonic helical nanoapertures for polarization-encrypted data storage.* Light: Science & Applications, 2019. **8**(1): p. 45.

92. Chen, Y., J. Gao, and X. Yang, *Direction-Controlled Bifunctional Metasurface Polarizers.* Laser & Photonics Reviews, 2018. **12**(12): p. 1800198.

93. Pfeiffer, C. and A. Grbic, *Controlling Vector Bessel Beams with Metasurfaces.* Physical Review Applied, 2014. **2**(4): p. 044012.

94. Zhao, Y., M.A. Belkin, and A. Alu, *Twisted optical metamaterials for planarized ultrathin broadband circular polarizers.* Nature Communications, 2012. **3**: p. 870.

95. Menzel, C., C. Rockstuhl, and F. Lederer, *Advanced Jones calculus for the classification of periodic metamaterials.* Physical Review A, 2010. **82**(5): p. 053811.

96. Wen, D., et al., *Light field on a chip: metasurface-based multicolor holograms.* Advanced Photonics, 2021. **3**(2): p. 024001.

97. Li, X., et al., *Multicolor 3D meta-holography by broadband plasmonic modulation.* Science Advances, 2016. **2**(11): p. e1601102.

98. Li, X.P., et al., *Athermally photoreduced graphene oxides for three-dimensional holographic images.* Nature Communications, 2015. **6**: p. 6984.

99. Jin, L., et al., *Dielectric multi-momentum meta-transformer in the visible.* Nature Communications, 2019. **10**(1): p. 4789.

100. Wang, B., et al., *Polarization-controlled color-tunable holograms with dielectric metasurfaces.* Optica, 2017. **4**(11): p. 1368-1371.

101. Walther, B., et al., *Spatial and Spectral Light Shaping with Metamaterials.* Advanced Materials, 2012. **24**(47): p. 6300-6304.

102. Kipp, L., et al., *Sharper images by focusing soft X-rays with photon sieves.* Nature, 2001. **414**(6860): p. 184-188.

103. Cao, Q. and J. Jahns, *Focusing analysis of the pinhole photon sieve: individual far-field model.* Journal of the Optical Society of America A, 2002. **19**(12): p. 2387-2393.

104. van Nielen, N., et al., *Electrons Generate Self-Complementary Broadband Vortex Light Beams Using Chiral Photon Sieves.* Nano Letters, 2020. **20**(8): p. 5975-5981.

105. Xu, Z., et al., *Quantitatively Correlated Amplitude Holography Based on Photon Sieves.* Advanced Optical Materials, 2020. **8**(2): p. 1901169.

106. Ren, L. and B. Chen, *Proximity effect in electron beam lithography.* Proceedings. 7th International Conference on Solid-State and Integrated Circuits Technology, 2004., 2004. **1**: p. 579-582 vol.1.

107. Li, G.X., et al., *Continuous control of the nonlinearity phase for harmonic generations.* Nature Materials, 2015. **14**(6): p. 607-612.

108. Keren-Zur, S., et al., *Nonlinear Beam Shaping with Plasmonic Metasurfaces.* ACS Photonics, 2016. **3**(1): p. 117-123.

109. Sain, B., C. Meier, and T. Zentgraf, *Nonlinear optics in all-dielectric nanoantennas and metasurfaces: a review.* Advanced Photonics, 2019. **1**(2): p. 024002.

110. Li, G., S. Zhang, and T. Zentgraf, *Nonlinear photonic metasurfaces.* Nature Reviews Materials, 2017. **2**(5): p. 17010.

111. Gao, Y., et al., *Nonlinear Holographic All-Dielectric Metasurfaces.* Nano Letters, 2018. **18**(12): p. 8054-8061.

112. Fejer, M.M., et al., *Quasi-phase-matched second harmonic generation: tuning and tolerances.* IEEE Journal of Quantum Electronics, 1992. **28**(11): p. 2631-2654.

113. Xu, P. and S.N. Zhu, *Review Article: Quasi-phase-matching engineering of entangled photons.* AIP Advances, 2012. **2**(4): p. 041401.

114. Zhang, X., et al., *Quasi-phase-matching and quantum-path control of high-harmonic generation using counterpropagating light.* Nature Physics, 2007. **3**(4): p. 270-275.

115. Mao, N., et al., *Nonlinear Diatomic Metasurface for Real and Fourier Space Image Encoding.* Nano Letters, 2020. **20**(10): p. 7463-7468.

116. Almeida, E., O. Bitton, and Y. Prior, *Nonlinear metamaterials for holography.* Nature Communications, 2016. **7**(1): p. 12533.

117. Reineke, B., et al., *Silicon Metasurfaces for Third Harmonic Geometric Phase Manipulation and Multiplexed Holography.* Nano Letters, 2019. **19**(9): p. 6585-6591.

118. Boyd, R., *Nonlinear Optics.* Academic Press, 2008. **3**: p. 640.

119. Franken, P.A., et al., *Generation of Optical Harmonics.* Physical Review Letters, 1961. **7**(4): p. 118-119.

120. S. Bhagavantam, P.C., *Harmonic generation and selection rules in nonlinear optics.* Indian Academy of Sciences, 1972. **76**(1): p. 13-20.

121. Konishi, K., et al., *Polarization-Controlled Circular Second-Harmonic Generation from Metal Hole Arrays with Threefold Rotational Symmetry.* Physical Review Letters, 2014. **112**(13): p. 135502.

122. Hu, Y.Q., et al., *3D-Integrated metasurfaces for full-colour holography.* Light-Science & Applications, 2019. **8**: p. 86.

123. Imura, K., T. Nagahara, and H. Okamoto, *Near-Field Two-Photon-Induced Photoluminescence from Single Gold Nanorods and Imaging of Plasmon Modes.* The Journal of Physical Chemistry B, 2005. **109**(27): p. 13214-13220.

124. Klein, M.W., et al., *Experiments on second- and third-harmonic generation from magnetic metamaterials.* Optics Express, 2007. **15**(8): p. 5238-5247.

125. Klein, M.W., et al., *Experiments on second- and third-harmonic generation from magnetic metamaterials: erratum.* Optics Express, 2008. **16**(11): p. 8055-8055.

126. Makarov, S.V., et al., *Efficient Second-Harmonic Generation in Nanocrystalline Silicon Nanoparticles.* Nano Letters, 2017. **17**(5): p. 3047-3053.

127. Zhou, Y., et al., *Multilayer Noninteracting Dielectric Metasurfaces for Multiwavelength Metaoptics.* Nano Letters, 2018. **18**(12): p. 7529-7537.

128. Liu, S., et al., *Resonantly Enhanced Second-Harmonic Generation Using III–V Semiconductor All-Dielectric Metasurfaces.* Nano Letters, 2016. **16**(9): p. 5426-5432.

Appendix

Scientific contributions

Publications

2021	A wavelength and polarization selective photon sieve for holographic applications D. Frese, B. Sain, H. Zhou, Y. Wang, L. Huang, T. Zentgraf Nanophotonics (2021), 10 (18), 4543-4550
2021	Nonlinear Bicolor Holography Using Plasmonic Metasurfaces D. Frese, Q. Wei, Y. Wang, M. Cinchetti, L. Huang, T. Zentgraf ACS Photonics (2021), 8 (4), 1013–1019
2019	Nonreciprocal Asymmetric Polarization Encryption by Layered Plasmonic Metasurfaces D. Frese, Q. Wei, Y. Wang, L. Huang, T. Zentgraf Nano Letters (2019), 19 (6), 3976-3980

Conference contributions

2020	D. Frese, Q. Wei, Y. Wang, M. Cinchetti, L. Huang, T. Zentgraf Nonlinear color holography using plasmonic metasurfaces Online PhD Workshop, TRR142 der Deutschen Forschungsgesellschaft, Talk
2020	D. Frese, Q. Wei, Y. Wang, L. Huang, T. Zentgraf Bilayered plasmonic metasurface for non-reciprocal holographic image encryption Photonics West, San Francisco, USA, Talk
2019	D. Frese, Q. Wei, L. Huang, T. Zentgraf Wavelength multiplexed nonlinear plasmonic metasurface holography 6th CRC/TRR 142 workshop 2019, Talk
2019	D. Frese, L. Meng, H. Zhong, T. Zentgraf Characterization of the optical Kerr-Effect in CsPbBr3-perovskite films DPG-Frühjahrstagung, Regensburg, Talk
2018	D. Frese, M. Cinchetti, T. Zentgraf Characterization of the optical Kerr-Effect in CsPbBr3-perovskite films 5th CRC/TRR 142 workshop 2018, Poster

Acknowledgment

I would now like to express my sincere thanks to the people who have accompanied and supported me during the preparation of this dissertation. My special thanks go to

- Prof. Dr. Thomas Zentgraf for giving me the opportunity to carry out my projects at Paderborn University. Furthermore, I would like to especially thank him for the support and advice during my time in his research group. He helped me at any time to solve any problem that occurred. Many thanks for a great time in his group, in which I could develop myself scientifically and personally.
- Prof. Dr. Donat Josef As for reviewing this work.
- all the group members I had the privilege of working with during my time at Paderborn University. I would especially like to thank my office colleagues Felicitas Walter, Bernhard Reineke, René Geromel, Christian Schlickriede, and Philip Georgi. We were divided into two offices, but it felt like one. We had an open exchange about our research topics at any time and always motivated each other when things got difficult. Further, I would like to thank Basudeb Sain who openly shared his experience in sample fabrication, as well as Wenlong Gao for a great time in Birmingham and later in Paderborn. Even outside the university it was, and always is, a pleasure to do something with you. I have made really good friends here.
- the scientists who worked with me on my projects. Many thanks to Lingling Huang, Hongqiang Zhou, Yongtian Wang, and Qunshuo Wei from the Beijing Institute of Technology for the great and friendly cooperation.
- Prof. Dr. Mirko Cinchetti, my co-supervisor, and his group for the support when we tried to reconstruct the nonlinear holograms in Dortmund. I was impressed with how well we were taken care of here, even if it went long into the night.
- Philip Georgi and Bernhard Reineke for proofreading this work and to Maike Doll for spelling correction.
- Florian Spreyer, who became one of my best friends during this time. I always enjoyed the time with him during coffee breaks, in the lab, at conferences (where it all began), at lunch, and also at the after-work beers.
- my little family! My wife Anna supports me every day in all my plans and watches my back. Thank you for your support in all circumstances and for keeping everything in perspective. Also many thanks to my little daughter Ella who gives me so many hugs when

I come home that I can forget about problems and get back to work motivated. I thank you both for the love and support you give me every day!

- my parents Andrea and Markus, and my brother Marc, who have been with me since day one and have always given me advice and support.